

VO₂ Nanostructures for Batteries and Supercapacitors: A Review

Ziyauddin Khan,* Prem Singh, Sajid Ali Ansari, Sai Rashmi Manippady, Amit Jaiswal,* and Manav Saxena*

Vanadium dioxide (VO₂) received tremendous interest lately due to its unique structural, electronic, and optoelectronic properties. VO₂ has been extensively used in electrochromic displays and memristors and its VO₂ (B) polymorph is extensively utilized as electrode material in energy storage applications. More studies are focused on VO₂ (B) nanostructures which displayed different energy storage behavior than the bulk VO₂. The present review provides a systematic overview of the progress in VO₂ nanostructures syntheses and its application in energy storage devices. Herein, a general introduction, discussion about crystal structure, and syntheses of a variety of nanostructures such as nanowires, nanorods, nanobelts, nanotubes, carambola shaped, etc. are summarized. The energy storage application of VO₂ nanostructure and its composites are also described in detail and categorically, e.g. Li-ion battery, Na-ion battery, and supercapacitors. The current status and challenges associated with VO₂ nanostructures are reported. Finally, light has been shed for the overall performance improvement of VO₂ nanostructure as potential electrode material for future application.

1. Introduction

Batteries and supercapacitors are electrochemical energy storage (EES) devices that conduct reversible conversion of chemical energy into electrical energy, have been regarded as

Dr. Z. Khan
Laboratory of Organic Electronics
Department of Science and Technology
Linköping University
Norrköping SE-60174, Sweden
E-mail: ziyauddin.khan@liu.se

P. Singh, Dr. A. Jaiswal
School of Basic Sciences
Indian Institute of Technology Mandi
Kamand, Mandi, Himachal Pradesh 175005, India
E-mail: j.amit@iitmandi.ac.in

Dr. S. A. Ansari
Department of Physics
College of Science
King Faisal University
P.O. Box 400, Hofuf, Al-Ahsa 31982, Kingdom of Saudi Arabia

S. R. Manippady, Dr. M. Saxena
Centre for Nano and Material Sciences
Jain University
Ramanagaram, Bangalore, Karnataka 562112, India
E-mail: s.manav@jainuniversity.ac.in

 The ORCID identification number(s) for the author(s) of this article can be found under <https://doi.org/10.1002/smll.202006651>.

DOI: 10.1002/smll.202006651

sustainable energy generation sources, and already show a wide variety of applications ranging from household electronics to electrical vehicles.^[1] Batteries are classified as energy devices whereas, supercapacitors are regarded as power devices. These devices have captured the market for small electric appliances such laptops, mobiles, etc. as clean energy sources since they can be prepared from environmentally friendly materials, have sufficient specific energy and decent cyclic life, and are comparatively cheaper. However, the major obstacle to realize the high performance of EES devices for their application in hybrid electric vehicles and electric vehicles are mainly related to the issues from both the active electrode materials related to low specific energy and poor cyclic stability, and electrolyte related to flammability and leakage. Therefore, it would be worth to say that the realization

for high performing EES devices is mainly hampered by the poor functioning electrodes and electrolyte. Though both the areas need improvement, however, research is focused on the advancement of electrode materials for EES devices to improve the performance related to ion storage, rate capability, and rechargeability by their innovative synthetic approaches. With the concentrated research attended with noteworthy development, the cathode side still shows a limiting concern to enhanced battery performance due to its lower specific capacity and significant degradation after a long-time span. Moreover, the cathode is also one of the expensive and most challenging materials components against the anode of the full cell. Nanostructured materials having different morphology, size, and shape were explored and investigated as electrode material for EES devices to improve the performance.^[1c,2] These nanostructured materials showed unique electrochemical behavior than their bulk counterparts.

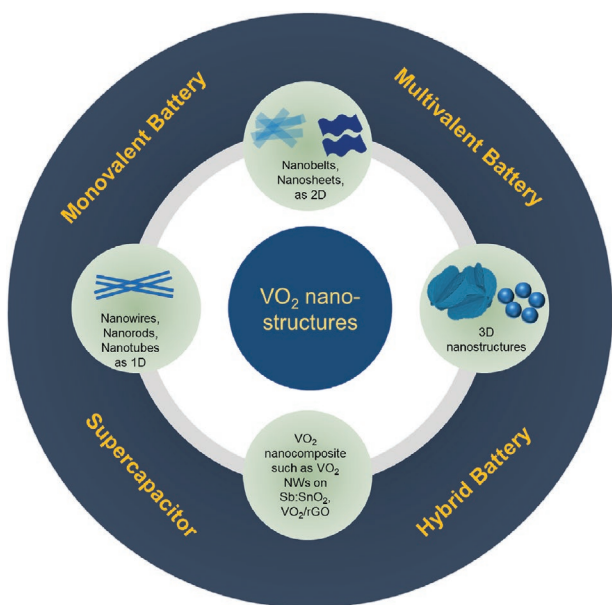
Number of electrode materials such as carbon-based materials, metal oxides, phosphates, etc. were used in EES and their performances were studied comprehensively.^[2m,3] Oxides of vanadium such as V₂O₅, VO₂, V₃O₇, and V₂O₃ have been utilized in batteries and supercapacitors, thanks to their high specific capacities, high specific energy, moderate work-potential, unique lamellar or layered structure, and low cost.^[4] Vanadium is a naturally abundant element with about 0.019% in the earth's crust (average concentration of 150 mg kg⁻¹ in mineral ores and 3–300 mg kg⁻¹ in soil) and it reacts easily with oxygen to form

oxides of different phases and morphologies.^[5] Vanadium possesses multivalent stable oxidation states (+5 to +2) allowing the formation of several compositions with exciting properties combining structural transformation and optical, magnetic, or electronic modification. It has a wide range of utilization scenarios in various technological applications such as EES, sensors, solar cells, photocatalysis, electrochromic displays, and thermochromic smart windows owing to its unique switchable activity, optoelectronic and magnetic features.^[1c,4i,j] V_2O_5 , one of vanadium oxide, has been studied primarily in Li-ion batteries (LIBs) thanks to its high specific capacity of 294 mAh g⁻¹ for two Li⁺ ions or 437 mAh g⁻¹ for three Li⁺ ion intercalation/deintercalation,^[6] which is greater than the traditional LiCoO₂ (140 mAh g⁻¹)^[7] and LiFePO₄ (170 mAh g⁻¹)^[8] cathode materials. Despite the high capacity, crystalline V_2O_5 suffers from low electronic conductivity (10^{-2} to 10^{-3} S cm⁻¹), poor Li⁺ ion diffusion coefficient (10^{-12} to 10^{-13} cm² s⁻¹), irreversible phase change, and vanadium dissolution in the electrolyte.^[9] Also, the layered V_2O_5 showed fast capacity degradation and sluggish rate capability possibly due to the self-aggregation and increased charge transfer resistance on cycling which hampers its commercial use. Vanadium dioxide (VO_2) shows rapid metal ion diffusion, higher capacity (323 mAh g⁻¹ for one Li per VO_2),^[10] and superior rate capability to other vanadium oxides which makes it an appropriate electrode material for energy storage for LIBs and also for post Li-ion EES devices. VO_2 nanostructures^[11] such as nanoparticles, nanowires (NWs), nanobelts, nanoscrolls, etc. and different composites^[4a,12] were utilized as electrode materials and found that these nanostructures have unique electrochemical properties than bulk material. Nanostructured materials can have different morphologies such as 1D (NWs, nanotubes), 2D (nanosheets, nanobelts, nanoribbons), and 3D (flower shaped, carambola shaped, NWs grown on hollow microspheres, etc.).^[13] Also, they provide a high surface to volume ratio, short diffusion path length for ions, facilitate electrolyte diffusion owing to their open and porous structure, and can sustain huge volume changes during the insertion/ extraction of ions.

There are separate reviews on vanadium oxide^[14] in general with application in energy storage but to date there is no review, specifically focusing on VO_2 nanostructures which discuss its importance and implication on energy storage application. Thus, we believe there exists plenty of room for a review article on VO_2 nanostructures for energy storage applications. The present review illustrates the details of crystal structure, charge storage mechanism, numerous synthetic approaches, and its application for batteries and supercapacitors (Scheme 1) to provide a better understanding and enormous capability of VO_2 nanostructures as electrode material.

2. Crystal Structure of VO_2 : Phases with Their Advantages and Disadvantages

VO_2 exhibits numerous polymorphs such as VO_2 (M), VO_2 (R), VO_2 (T) and few metastable phases such as VO_2 (A), VO_2 (B), and VO_2 (C), etc.^[14a,15] The polymorphs VO_2 (M) and VO_2 (R) show rapid metal insulator transition (MIT) at critical temperature which changes its electronic and optical properties



Scheme 1. VO_2 nanostructures and their energy storage application.

making it applicable for optoelectronic switching, memristors, and intelligent window coatings.^[16] The low temperature phase belongs to monoclinic crystal structure with space group $P2_1/c$ (No. 14) and lattice parameters $a = 0.575$ nm, $b = 0.452$ nm, $c = 0.538$ nm, and $\beta = 122.6^\circ$.^[15a,17] As stated elsewhere “The structure involves V⁴⁺–V⁴⁺ pairing with alternate shorter (0.265 nm) and longer (0.312 nm) V⁴⁺–V⁴⁺ distances along the monoclinic a -axis, and tilting with respect to the rutile c -axis.”^[17] In rutile structure, body center positions and vertex of the tetragonal structure were occupied by V⁴⁺ ions and each V atom is surrounded by an edge-sharing octahedron of oxygen atoms (VO₆).^[15a] In VO_2 (R) the lattice parameters are $a = b = 0.455$ nm, $c = 0.286$ nm and belongs to $P4_2/mnm$ (No. 136) space group. In 1971, Goodenough proposed the band structure diagram to explain the conducting and insulating nature of the both rutile and monoclinic phase.^[18] In monoclinic band structure, the $d_{||}$ band, originates by splitting of t_{2g} state, splits into two energy bands filled bonding ($d_{||}$) and empty antibonding ($d_{||^*}$) states (Figure 1a). Also, the π^* bands move to higher energy due to the antiferroelectric zigzag type displacement of vanadium atoms.^[19] A forbidden band is formed between $d_{||}$ band and π^* band and the Fermi level falls well within the forbidden band thereby making VO_2 (M) insulative.^[15a,18] However, in the case of VO_2 (R), the Fermi level lies between the $d_{||}$ and π^* bands and thus displays electrical conductivity.

The metastable phase VO_2 (B) was also considered and studied as a promising electrode material due to its layered structure which can accommodate ions between the layer (Figure 1b) and showed electrode potential plateau at 2.5–2.6 V.^[20] Also, it has a shear-type structure which allows fast ion diffusion through the formed tunnel and also resists lattice shearing during the galvanostatic charge-discharge processes in batteries.^[14a,21] The VO_2 (B) phase crystallizes into triclinic crystal structure with $a = 1.23$ nm, $b = 0.369$ nm, $c = 0.64$ nm, and $\beta = 106.1^\circ$ and space group C 2/m (No. 12).^[22] Another VO_2 phase studied in energy storage application is

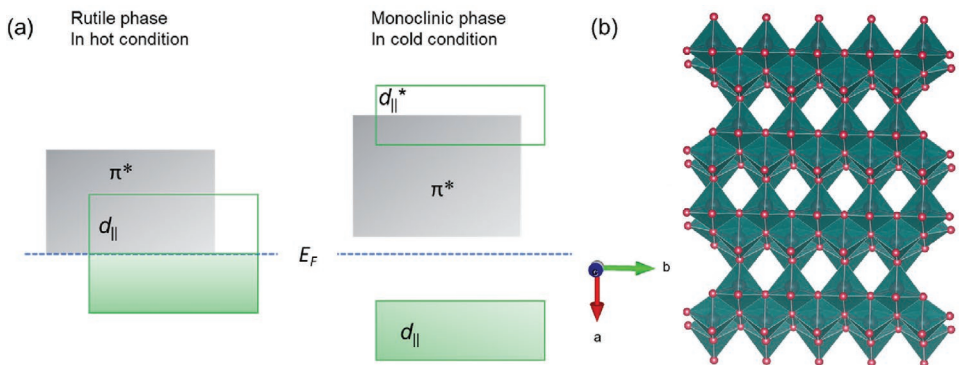


Figure 1. a) Schematic illustration of VO_2 band structure showing the metallic rutile phase and insulating monoclinic phase. Adapted with permission.^[19] Copyright 2002, Wiley VCH. b) Crystal structure of VO_2 (B) phase. Adapted with permission.^[66] Copyright 2015, The Royal Society of Chemistry.

"paramontroseite" which also formed a tunnel structure.^[23] In this structure, VO₆ octahedra linked together to form double chains and the two chains are connected through one axial and another equatorial oxygen atom with each other thus forming a tunnel structure.^[23a]

3. Synthetic Method of VO_2 Nanostructures

In 1980s, vanadium oxides were prepared by the thermal decomposition of ammonium vanadate (NH_4VO_3) in an inert or reducing atmosphere at 450 °C.^[24] However, since the discovery of VO_x nanotubes in 1998 by R. Nesper and his team,^[25] a variety of techniques have been developed to synthesize vanadium oxide nanomaterials having different sizes and shapes. These techniques can be categorized as hydrothermal/solvothermal, thermal pyrolysis, chemical vapor deposition (CVD), electrospinning, liquid exfoliation, pulsed laser deposition (PLD), electron/ion beam lithography, and freeze-drying treatment.^[14a,26] In most of the energy storage applications, VO_2 (B) has been used as an electrode but VO_2 (B) is a metastable phase that can transform irreversibly above 537 °C to a thermodynamically stable rutile phase.^[11a] Therefore, there has been different approaches utilized to synthesize different nanostructures and stable phase of vanadium oxide at a lower temperature. Herein, we have divided the synthesis methodology into two sections, the first section is focused on the general methods used and the second section provides a brief description of the synthesis of VO_2 nanostructures such as 1D, 2D, and 3D nanostructures.

3.1. Common Synthetic Approaches for VO_2

3.1.1. Hydrothermal/Solvothermal Method

Hydrothermal treatment of vanadium (V) species in aqueous solutions is the most popular method for the synthesis of a wide range of vanadium oxides from 0D to 2D nanostructures.^[1c] In a typical hydrothermal process, a Teflon-lined stainless steel autoclave with a temperature beyond 300 °C containing an aqueous solution of vanadium precursor and a reducing agent is used for the synthesis of vanadium oxide nanoparticles.^[27]

Usually, hydrazine hydrate is used as a strong reductant which also played a key role in the formation of VO_2 (M) nanoparticles.^[28] A one-step hydrothermal/solvothermal method is facile and cost-efficient. Gao et al. were the first who reported the synthesis of W-doped snowflake-shaped VO_2 (R) via one-pot hydrothermal method at 240 °C for 7 days.^[29] Authors concluded that a proper amount of W is crucial for the formation of VO_2 (R). Later, a similar kind of morphology of VO_2 (M) was reported by other groups by manipulating the number of precursors and reaction conditions. Chen et al. reported the synthesis of monoclinic VO_2 nanoparticles by following the one-step rapid hydrothermal process by using ammonium metavanadate and hydrazine as a precursor and reductant, respectively.^[28] By this one-step rapid hydrothermal method, they concluded that the amount of precursor and high temperature, that is, above 340 °C helped in the formation of pure for VO_2 (M) nanoparticles. In another work, Jin et al. used a hydrothermal-assisted homogeneous precipitation approach for the synthesis of VO_2 nanoparticles.^[4b] They observed that the lower concentration of vanadium precursors yields large rod-like crystals, while a higher concentration of precursors leads to the formation of small spherical nanostructures. In the same manner, Xia et al. studied the influence of the concentration of vanadium precursor, influence of pH, temperature, and dependence on reactants on the synthesis of VO_2 nanostructures.^[30] By manipulating these parameters, the authors controlled the phase and morphology of VO_2 nanocrystals from asterisk-shaped microcrystals to hexagon-shaped nanocrystals. Nevertheless, their study also suggested that the low-temperature hydrothermal synthesis of VO_2 (M) could be further improved and modified to produce pure VO_2 (M) NWs. There have been numerous works published for the synthesis of VO_2 (M) nanostructures using a direct hydrothermal approach.^[31] But still, this direct synthesis method and multiple valence states of vanadium ions and their ease of oxidation/reduction from V^{4+} to V^{5+} / V^{3+} species are the most critical and challenging.^[32] Also, this direct synthesis method requires several post-synthesis steps to remove any additional impurities and substances from the final product. The major problems associated with the direct hydrothermal method are: low reproducibility, time-consuming process, additional processing step to the final product risks oxidation/reduction of vanadium, low yield, and safety issues with autoclaves.^[32a] To address these issues, in the year 2018,

Palgrave et al. reported the synthesis of pure $\text{VO}_2(\text{M})$ nanoparticles using the direct continuous hydrothermal flow synthesis (CHFS) method. In a typical CHFS method, rapid hydrolysis, and subsequent dehydration/degradation of metal salts are the two main steps involved in the synthesis of metal oxide nanoparticles, where a stream of metal precursors is mixed with a stream of supercritical water inside an engineered mixer which further lead to the synthesis of metal oxide nanoparticles with a good yield (usually above 85%). In the past, the preparation of a pure form of $\text{VO}_2(\text{M})$ was challenging due to balanced flow rate conditions in the conventional form of CHFS which usually requires post-synthesis annealing at a very high temperature to obtain pure $\text{VO}_2(\text{M})$ which was overcome by Palgrave et al. They modified the CHFS apparatus and used unbalanced flow rate conditions in their reaction setup to obtain $\text{VO}_2(\text{M})$ nanoparticles. The advantage of this system is that it can immediately convert vanadium (IV) precursor into a $\text{VO}_2(\text{M})$ nanostructures without doing any post-synthesis heat treatment (**Figure 2a**).^[32a] The modified form of the CHFS method is direct, continuous, reproducible, and scalable which has the capability to produce a kg of material per hour.

3.1.2. Thermal Pyrolysis Method

The term pyrolysis is Greek-derived elements pyro “fire” and lysis “separating”. Thermal pyrolysis is a thermal

decomposition process to decompose materials or precursors at an elevated temperature in an anaerobic condition. The synthesis of vanadium oxide nanostructures through this technique could be realized by decomposing hydrated V(IV) compounds in a vacuum condition under moderate or elevated temperature conditions.^[14a] Liu and his co-workers prepared a W-doped VO_2 nanopowder by the thermal decomposition of $(\text{NH}_4)_5[\text{VO}_6 \cdot (\text{CO}_3)_4(\text{OH})_9] \cdot 10\text{H}_2\text{O}$ at low thermal conditions. The obtained nanopowders of monoclinic VO_2 were found to have narrow size distribution.^[33]

Later, Guan et al. reported the two-step synthesis of pure $\text{VO}_2(\text{M})$ particles with tunable crystallinity and morphology.^[34] In the first step, the authors thermally decomposed the precursor vanadyl ethylene glycolate (VEG) followed by a post-annealing process under an oxygen-free atmosphere. In the 2nd step, a pure $\text{VO}_2(\text{M})$ compound with different crystallite sizes was synthesized under an anaerobic condition (500 or 700 °C). Figure 2b,c represents the two-step synthesis of pure $\text{VO}_2(\text{M})$ by the thermal pyrolysis method. The solvent-thermal pyrolysis method for the preparation of $\text{VO}_2(\text{M})$ nanopowder of mean size 22 nm was also reported in the literature.^[35] Very recently, Zeng et al. proposed a solid-state de-wetting combined with the thermal pyrolysis method for the preparation of VO_2 thin films.^[36] Figure 2d,e represents the schematic diagram of the solid-state de-wetting and pyrolysis process for the synthesis of VO_2 nanoparticles. The thermal pyrolysis method is rarely used for the synthesis of a variety of vanadium oxide nanoparticles

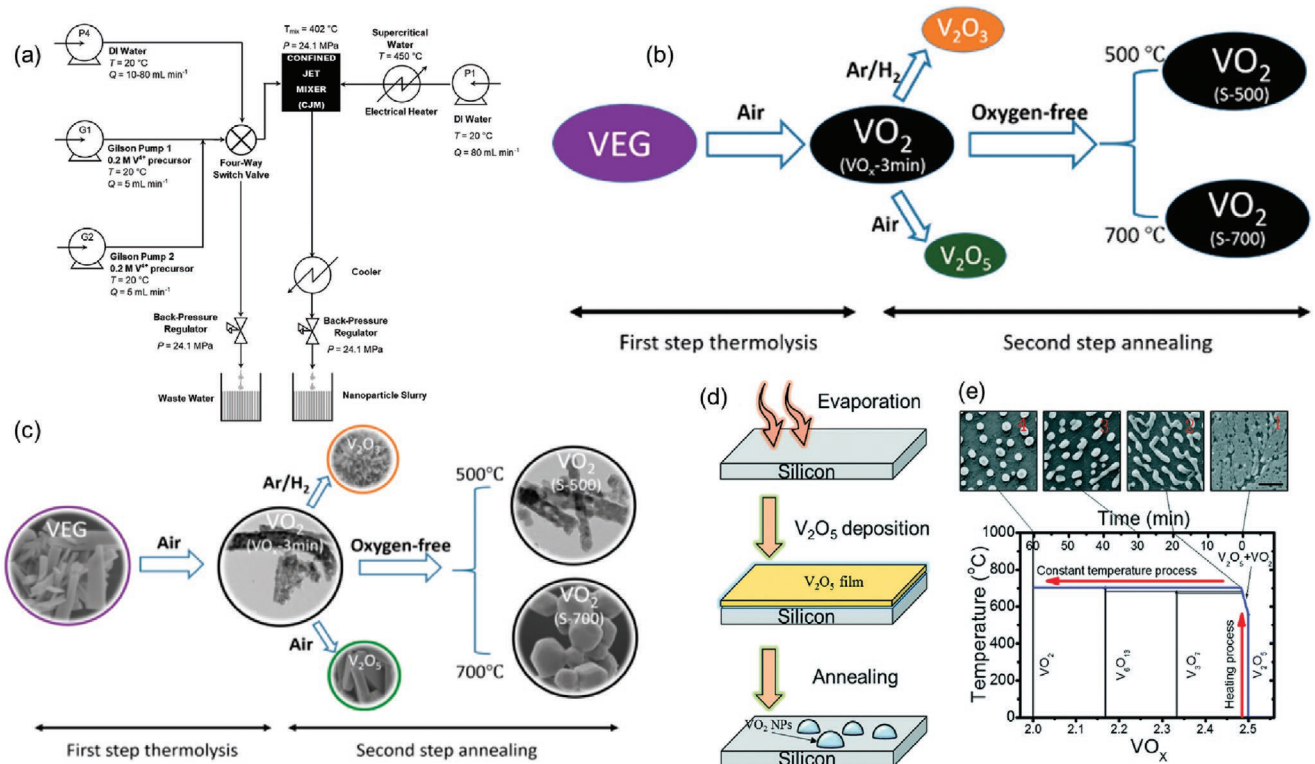


Figure 2. a) Schematic illustration of the CHFS process used to synthesize $\text{VO}_2(\text{M})$ nanoparticles. Reproduced with permission.^[32a] Copyright 2018, Royal Society of Chemistry. b,c) Synthesis of pure $\text{VO}_2(\text{M})$ nanostructure by the thermal pyrolysis method. Reproduced with permission.^[34] Copyright 2018, American Chemical Society. d) The graphic illustration for the synthesis of VO_2 nanoparticles by solid-state de-wetting and pyrolysis process. e) V–O composition and temperature phase diagram which illustrates the change of phase and morphology of VO_2 particles during synthesis. Reproduced with permission.^[36] Copyright 2019, Royal Society of Chemistry.

due to issues related to scalable fabrication for practical applications.

3.1.3. Sputtering Method

The reactive ion beam sputtering technique for the preparation of VO_2 thin films was first reported by Fuls et al. in 1967.^[37] Till now, a number of sputtering techniques were developed so far such as radio frequency (RF), direct current (DC), and magnetron sputtering. Nowadays sputtering technique is most preferred for the preparation of thin films because of its advantage of uniform coating, high control on film thickness by controlling the sputtering time, high deposition efficiency, and strong interaction between substrate and thin films. Chen et al. reported the two-step synthesis method for the preparation of VO_2 thin films.^[38] In the first step, the thin films of V_2O_3 and VO_2 were prepared by using reactive ion beam sputtering deposition. Subsequently, the thermal annealing method was applied to form thin films of VO_2 . After annealing, thin films were exposed at 405 °C for 100 min under Ar atmosphere. In 2014 Zhang et al. reported the fabrication of grain size VO_2 films on a glass substrate via DC magnetron sputtering method. They modulated the size of VO_2 nanoparticles from 49.4 to 77 nm on thin films by varying the annealing time from 15–90 min.^[39] Later in 2014, preparation of VO_2 thin films on soda-lime glass substrate was reported.^[40] Authors used the RF magnetron sputtering method followed by annealing to produce thin VO_2 films. With the same technique, that is, RF magnetron sputtering, Nishikawa et al. manipulated the VO_2 NPs size by manipulating and controlling the sputtering time. The authors also noticed the role of oxygen partial pressure on the morphology and structure of VO_2 thin films (Figure 3).^[41] Fang et al. reported the fabrication of VO_2 nanoparticles hole array on anodic aluminium oxide (AAO) template via the DC magnetron sputtering method.^[42] By following the electrochemical

etching technique, the authors prepared an AAO template having different spacing and pore size. Later, vanadium metal film was deposited on AAO templates under an Ar atmosphere. In the final step, the VO_2 nanoparticle hole arrays were formed by annealing under O_2 partial pressure.

3.1.4. PLD Method

PLD method is an alternative technique to the physical vapor deposition method. This technique was reported in 1993 for the preparation of vanadium oxide thin films.^[43] This process needs an ultra-high vacuum pressure in the presence of some background gases (oxidation-reduction and protective gas etc.), where the evaporated material is deposited on the desired substrate as a thin film with the help of a high-power pulsed laser beam. In 2009, Villani and her group reported the vanadium oxide thin films using ultrafast PLD technology.^[44] Figure 4 represents the PLD experimental setup used by Villani. Later using the PLD method, a different polymorphic phase of VO_2 was obtained by depositing V_2O_3 thin films on a silicon substrate.^[45] Few other groups too reported the fabrication of vanadium oxide thin films using the PLD method.^[2b,46]

3.1.5. Flame Spray Pyrolysis (FSP), and Combustion-Assist Fabrication

In the FSP technique, the precursor solution is carried by gases and sprayed to the bottom of the ignited flame. Mostly methane and oxygen gases are used to generate the flame. When this mixture of aqueous precursors comes in contact with flame, it gets vaporized, then condensed and crystallized into smaller nanostructures within a fraction of a second.^[47] Figure 5a represents the schematic diagram of the spraying pyrolysis process.^[48] This technique is rapid and facile and gives high quality

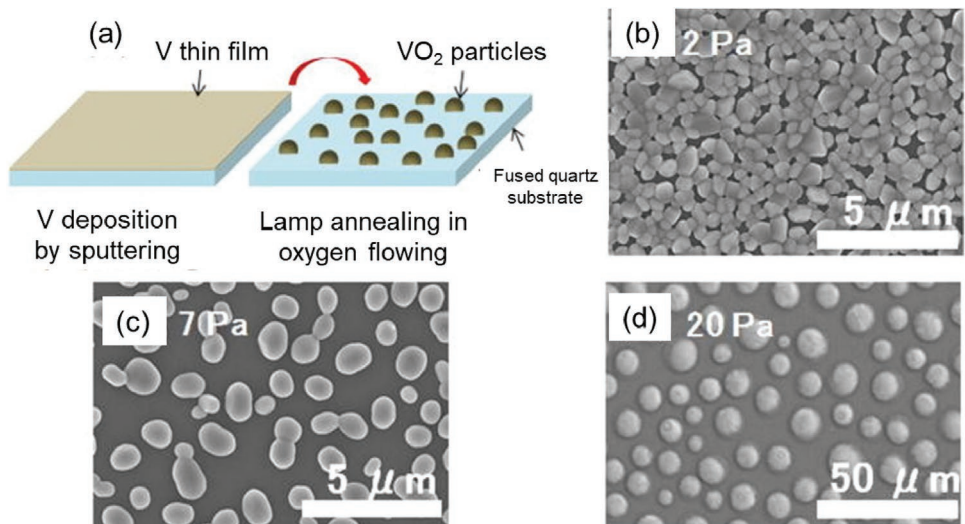


Figure 3. a) Schematic illustration for the synthesis of VO_2 nanoparticles by sputtering and post-lamp annealing process on fused quartz substrates. b-d) SEM images of the VO_2 particles at different oxygen gas pressure during the annealing process. Reproduced with permission.^[41] Copyright 2017, American Institute of Physics.

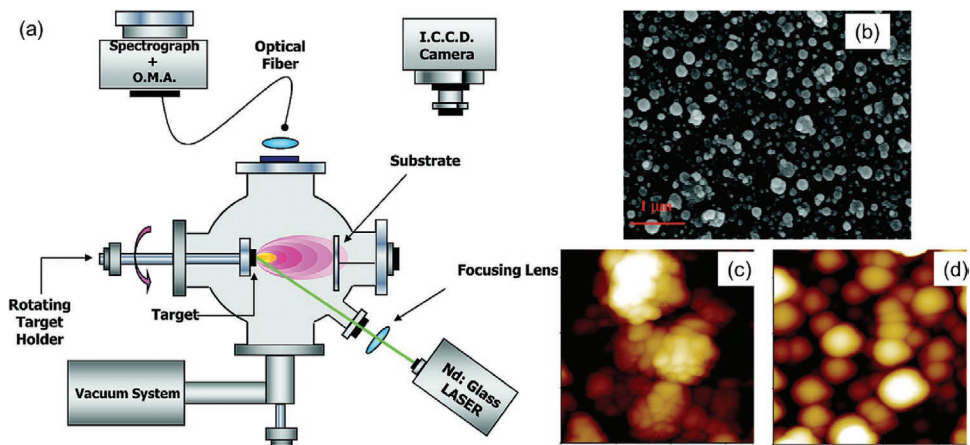


Figure 4. a) PLD experimental setup by Villani et al. b) SEM image of a film acquired by the excision of a V_2O_5 target for the 1.5 h deposition time and the laser fluence 3.0 J cm^{-2} . AFM image of the c) center and d) border of the film. Image dimensions are $700 \text{ nm} \times 700 \text{ nm}$. Reproduced with permission.^[44] Copyright 2009, American Chemical Society.

of vanadium oxide nanoparticles in one step. Umarji and his co-workers prepared low-cost VO_2 (M) thin films by using the ultrasonic nebulized spray pyrolysis (UNSP) method.^[49] They followed a two-step synthesis process, in the first step, the authors deposited V_2O_5 thin films on a quartz substrate at 400°C and next they used a nebulized spray having an aqueous combustion mixture of oxidizer (vanadyl nitrate) and a fuel (urea) to reduce V_2O_5 thin films to obtain pure VO_2 thin films. The same group also reported the preparation of VO_2 films over the LaAlO_3 substrate.^[50] However, other reaction parameters and ingredients were constant.

In the combustion-assist technique, flammable precursors are ignited which further undergoes endothermic pyrolysis to produce smaller nanostructures. This whole process is carried out in the ambient condition and suitable for the synthesis of VO_2 (M) nanoparticles. Synthesis of VO_2 (M) nanoparticles using vanadyl acetylacetone ($\text{VO}(\text{acac})_2$) and ethanol precursors are already reported using the combustion-assist Figure 5b.^[51] Parameters like the amount of precursor and its

composition, container size, and diameter are critical to avoid impure polymorph or other oxidation states of vanadium. Broad size distribution (50 nm to 10 μm) and uneven heat distribution during combustion reactions are major drawbacks of this technique.^[51]

3.1.6. Other Methods

In Addition to these methods, there are some other techniques reported for the synthesis of different VO_2 nanostructures. The electrospinning method is a facile and commonly used technique for the synthesis of metal oxides nanofiber. However, this technique is hardly used in the preparation of VO_2 nanofibers. Using this technique, the thickness of the electrospun fiber can be controlled mostly in the range of 200–300 nm.^[52] This generally involves a two-step method, wherein the first step, spinable precursor solution (a mixture of metal oxide precursor and a polymer solution) is used to draw charged threads. In

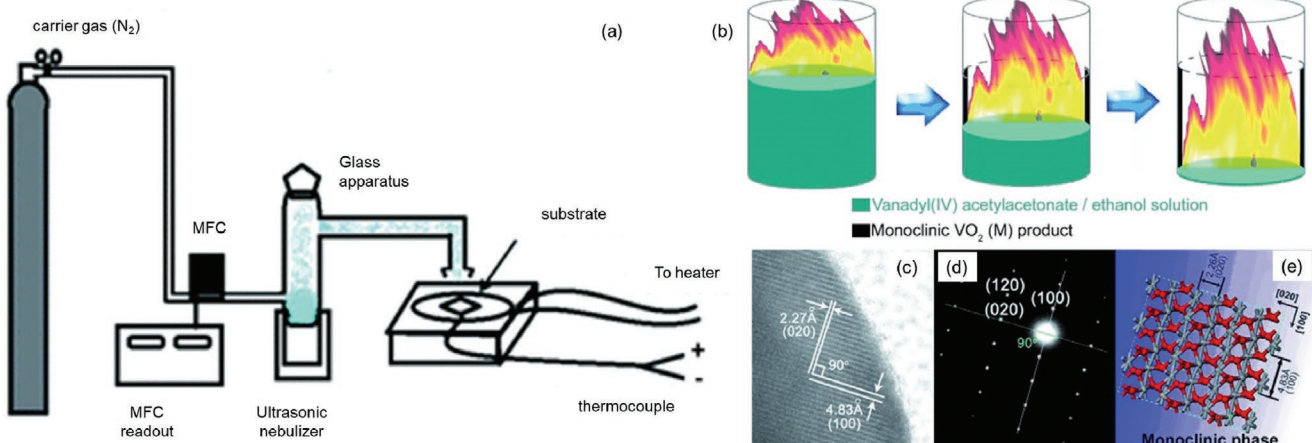


Figure 5. a) Illustration of the UNSP set up. Reproduced with permission.^[48] Copyright 2013, Royal Society of Chemistry. b) Synthesis of VO_2 (M) by direct confined-space combustion technique, c) HR-TEM image and d) SAED pattern and e) atomic model of VO_2 (M) particle. Reproduced with permission.^[51] Copyright 2010, Wiley-VCH.

the next step, the obtained electrospun fibers are calcined in a furnace for the degradation of polymers and the formation of metal oxides.^[52b] Berezina et al. prepared the VO₂ nanofibers by sol-gel electrospinning technique followed by the thermal treatment in air and Ar.^[53] To investigate the special properties of uniformly distributed VO₂ nanoparticles, Lopez et al.^[54] (in 2004) and Appavoo et al.^[55] (in 2012) reported the fabrication of vanadium oxide nanoarrays via electron/ion beam lithography. Ding et al. proposed a novel sol-gel method for the preparation of self-assembled porous thin films of VO₂ nanoparticles.^[56] For their experiment, they used a self-prepared precursor of vanadium metal, that is, cetyltrimethylammonium vanadium (CTAV). The same technique was also exploited by Lan et al. for the preparation of VO₂ thin films.^[57] The authors deposited V₂O₅ sol-gel on a plasma-treated glass slide, further they annealed the thin film at 500 °C for 2 h to obtain VO₂ nanoparticles below 10 nm. In **Table 1** we have summarized some published vanadium oxide nanostructures prepared by using different synthesis methods and respective synthetic parameters.

3.2. VO₂ Nanostructures Synthesis

3.2.1. 1D VO₂ Nanostructure

1D nanostructured materials can provide a high surface to volume ratio, high structural flexibility, and provide short path length for the movement of ions which improves the performance of EES devices. Armstrong et al. synthesized ultra-thin VO₂ NWs via reduction of V₂O₅ using ethylene glycol by solvothermal method at 180 °C for 48 h.^[58] The prepared VO₂ crystallized in its metastable tunneled structure VO₂ (B) phase and the size of ultra-thin NWs arranged in bundles was from 6–10 nm. Nethravathi et al., for the first time, synthesized a VO₂ nanotube/graphene composite using a hydrothermal method and used the composite as cathode material for LIBs.^[59] Typical synthesis involved the mixing of ammonium vanadate and graphene oxide (GO) in water followed by the addition of formic acid. The reaction mixture was heated in Teflon lined stainless steel autoclave at 180 °C for 48 h. Scanning electron microscopy (SEM) and transmission electron microscopy (TEM) images of composite confirmed the growth of 1D VO₂ nanotubes in graphene matrix. The formed VO₂ (B) nanotubes were few microns in length and ~100 nm in diameter. Usually, tubular morphology for VO_x species can be achieved with alkyl amines which act as a template or directing agents. However, in this case, the authors stated that GO layers acted as templates by providing a curved surface for crystallization of VO₂ (B) to tubular morphology. He et al. also synthesized 1D VO₂/reduced graphene oxide (rGO) (g-VO₂) nanorods by the one-pot method using the microwave-assisted solvothermal method.^[60] The prepared nanorods crystallized in VO₂ (B) phase with an average diameter of 200–300 nm and length 1–2 μm. Also, the nanorods were encapsulated with a thin layer of rGO which improved the conductivity and structural stability. These methods provide a facile synthetic approach for VO₂ nanorods which can be easily scalable for large scale

energy application, though the hydrothermal method reported for VO₂ nanorods is a time-consuming process except microwave assisted hydrothermal method.

3.2.2. 2D VO₂ Nanostructures

Synthesis of strongly anisotropic materials such as nanosheets is considered excellent approach to improve the performance of EES related to specific capacity and cyclic stability. The synthesis of VO₂ (B) nanobelts has also been reported as these nanostructures offer several advantages such as high interfacial intimacy between electrode and electrolyte and shorter diffusion path length for ions.^[61] VO₂(B)@C nanobelts (C refers to Carbon) nanostructures were synthesized using V₂O₅ and sucrose solution and treating this solution hydrothermally at 180 °C for 24 h.^[61] Under the hydrothermal condition, sucrose acts as a reducing agent due to the presence of hydroxyl groups and carbon source. Authors also varied sucrose amount to obtain different thickness of carbon on VO₂ (B) nanobelts. The size of prepared VO₂(B)@C nanobelts are 1–2 mm long, 120–160 nm wide, and ~25 nm thick, when the V₂O₅ and sucrose weight ratio was 5 (**Figure 6a–c**). However, decreasing the weight ratio from 5 to 2.5 and 1.67, no significant change in shape was observed except a slight decrease in length (**Figure 6d–i**). Further lowering the weight ratio to 1.25, reduces the length to 200–500 nm of formed VO₂ (B)@C nanobelts (**Figure 6j–l**). Interestingly, it was also observed that the thickness of carbon shell increased from 3 to 6.9 nm with reducing the weight ratio of V₂O₅ and sucrose from 5 to 1.25.

Huang et al. synthesized flexible free-standing binder-free VO₂ (B) film to avoid the usage of non-conductive binders. For synthesis, the authors first prepared VO₂ (B) nanobelts by hydrothermal method using NH₄VO₃ and formic acid as reaction precursors. The stainless steel autoclave was cooled down to room temperature and obtained dispersant was filtered through a filter paper using Buchner funnel to get thin VO₂ (B) free-standing film.^[62] The advantage of free-standing film is that it can be directly employed as electrode material without a binder. Li et al. synthesized 2D VO₂ (B) nanofibers by 3D V₂O₅.xH₂O aerogel as a precursor.^[63] The aerogel structure displays expanded interlayer spacing, high surface area, and small particle size which can help in efficient diffusion of ions and volumetric sustainability during ions intercalation. Authors' objective was to maintain the morphology and key structural advantage of aerogel in the final product. The synthesis involves hydrolysis of vanadyl triisopropoxide which formed gel within 1 min. The wet gel was kept at ambient condition and aged for 4 days in a sealed tube. After washing with anhydrous acetone and cyclohexane, the gel was freeze-dried to get 3D V₂O₅.xH₂O aerogel as presented in **Figure 7a**.^[63] The obtained aerogel was heated at 400 °C under high vacuum in Ar atmosphere to get pure phase and fibrous VO₂ (B) (**Figure 7b–c**) without any change in morphology with the precursor. Along with nanobelts and nanofibers, nanosheets of VO₂ were also synthesized. Wang et al. used a hydrothermal method to synthesize VO₂ nanosheets which involved treatment of V₂O₅ with

Table 1. Summary of published VO₂ nanostructures prepared by using different synthesis methods and their parameters.

| Morphology | Dimension | Size | Synthesis Method | Precursors/solvent used | Conditions | Year of synthesis | Ref |
|--|------------|---|-------------------------------|---|---|-------------------|-------|
| VO ₂ Nanoparticles of varied morphologies | 0D | 0–100 nm | Hydrothermal | NH ₄ VO ₃ & N ₂ H ₄ ·H ₂ O / H ₂ O | 340 °C for 6 h, final product dried at 50 °C for 10 h | 2019 | [28] |
| Sb ³⁺ -doped VO ₂ nanoparticles | 0D | 8–30 nm | Hydrothermal | V ₂ O ₅ , hydrazine, HCl, Sb ₂ O ₃ | 200–260 °C at different time points, final product dried at 90 °C for 60 min | 2012 | [79] |
| VO ₂ nanoparticles | 0D | — | Hydrothermal | VOSO ₄ , hydrazine / H ₂ O, and Ammonia | 240 °C for 36 h, final product annealed at 600 °C for 20 min | 2016 | [32b] |
| VO ₂ nanoparticles | 0D | Below 50 nm | Continuous hydrothermal flow | V ₂ O ₅ & Oxalic acid / H ₂ O | Temp: 402 °C & pressure 24.1 MPa | 2018 | [32a] |
| VO ₂ micro & nanocrystals/ asterisk or rod-shaped and hexagon-shaped microcrystals | 0D, 1D, 2D | 20–50 nm (crystal at pH 10), 50–200 nm (crystals at pH 8) | Hydrothermal | V ₂ O ₅ , H ₂ SO ₄ , hydrazine hydrate and NaOH. | 220 °C for 48 h, final product washed and dried | 2010 | [30] |
| VO ₂ Nanoparticles of varied morphologies | 0D | 20–50 nm | Hydrothermal | VOSO ₄ & CO(NH ₂) ₂ / H ₂ O | 260 °C for 24 h, final product dried at 60 °C for 10 h | 2014 | [80] |
| VO ₂ plates | 1D | — | Hydrothermal | V ₂ O ₅ & Citric acid / H ₂ O | 180 °C for 2 h and 220 °C for 1 h annealing under vacuum for 1 h, final product dried at 80 °C for 6 h | 2013 | [81] |
| VO ₂ Nanorods | 1D | l: 200 nm | Hydrothermal | V ₂ O ₅ & Oxalic acid / H ₂ SO ₄ | 260 °C for 4–48 h, final product dried at 60 °C for 10 h | 2010 | [31c] |
| VO ₂ nanobelt | 1D | — | Hydrothermal | V ₂ O ₅ & H ₂ O ₂ / H ₂ SO ₄ | 200–300 °C for 3–48 h, final product dried at 75 °C | 2011 | [82] |
| W-doped VO ₂ nanorod | 2D | l: 2.5 μm w: 600 nm | Hydrothermal | V ₂ O ₅ , Oxalic acid / H ₂ O | 280 °C for 6–72 h, final product dried at 60 °C for 6 h | 2015 | [31d] |
| VO ₂ Rods, stars, and sheets | 1D and 2D | — | Hydrothermal | V ₂ O ₅ , Oxalic acid / H ₂ O | At varied temp. for 24 h, final product dried at 60 °C under vacuum | 2014 | [31b] |
| Snowflake-shaped VO ₂ nanostructures | 2 D | t: 200–800 nm w: 200–300 nm | Hydrothermal | V ₂ O ₅ , Tungstenic powder & Oxalic acid / H ₂ O | 240 °C for 7 days, final product dried at 60 °C for 10 h | 2008 | [29] |
| VO ₂ nanobelt | 2D | w: 0.5–2.5 μm t: 200–450 nm | Hydrothermal | V ₂ O ₅ /PEG | 220 °C & 260 °C at different time, final product dried at 70 °C in air | 2013 | [31a] |
| VO ₂ polymorphs nanosheets, walnut, nanoaggregates, cucumber, and carambola like structures | 2D | l: 1μ d: 450 nm | Hydrothermal | ammonium metavanadate and oxalic acid | 160–180 °C for VO ₂ (B) & 180–220 °C for VO ₂ (D) | 2016 | [83] |
| VO ₂ Nanoflakes arrays | 3D | Nanoflakes size: 200 nm | Hydrothermal | V ₂ O ₅ and H ₂ C ₂ O ₄ powders/H ₂ O, H ₂ O ₂ & ethanol | 180 °C for 3 h; annealed at 400 °C in Ar + H ₂ | 2015 | [12] |
| Graphene quantum dots coated VO ₂ arrays | 3D | t: 15 nm | Hydrothermal | V ₂ O ₅ and H ₂ C ₂ O ₄ powders/H ₂ O, H ₂ O ₂ & ethanol | 180 °C for 3 h; dried at 120 °C in vacuum | 2015 | [4a] |
| Tungsten-doped VO ₂ nanopowders | 0D | — | Thermal pyrolysis | Tungstic acid, (NH ₄) ₅ [(VO) ₆ (CO ₃) ₄ (OH) ₉]·10H ₂ O, hydrazine hydrate | 450–500 °C for 0.5–1 h, final product cooled to room temp under N ₂ gas | 2007 | [33] |
| VO ₂ micropowder of varied morphologies | — | d: 2μm | Thermal pyrolysis | (NH ₄) ₅ [(VO) ₆ (CO ₃) ₄ (OH) ₉]·10H ₂ O, Ammonium hydrocarbonate | 350–410 °C for 0.5 h, later heated in silica tube at a rate of 5 °C min ⁻¹ in a flow of N ₂ gas | 2000 | [84] |
| VO ₂ (M) nanocrystals | 0D and 1D | 745 nm | Thermal pyrolysis | Vanadyl ethylene glycolate (VEG) | 1st step thermal decomposition at 300 °C, post-annealing 500 or 700 °C under anaerobic condition | 2018 | [34] |
| VO ₂ (M) nanopowder | 0D | 22 nm | solvent–thermal and pyrolysis | NH ₄ VO ₃ & C ₂ H ₆ O ₂ | 160–180 °C | 2015 | [35] |

Table 1. Continued.

| Morphology | Dimension | Size | Synthesis Method | Precursors/solvent used | Conditions | Year of synthesis | Ref |
|---|-----------|-------------------------------------|-------------------------------------|--|---|-------------------|-------|
| VO ₂ thin films on SiO ₂ substrate | — | t: 52–192 nm | Solid-state dewetting and pyrolysis | V ₂ O ₅ | Annealing 700 °C for 200 min at 5Pa | 2019 | [36] |
| VO ₂ thin films | — | h:20 nm d: 20 & 100 nm | Ion beam sputtering | V ₂ O ₃ and VO ₂ | Annealing 40–120 min in temp range of 280–480 °C under Ar atmosphere | 2007 | [38] |
| VO ₂ thin films | — | 49.4–77 nm | DC magnetron sputtering | Vanadium precursor | Annealing time 40–90 min | 2014 | [39] |
| VO ₂ thin films on soda-lime glass substrate | — | t: 400 nm | RF magnetron sputtering | V ₂ O ₅ | Magnetron power: 120W; substrate temp: 450 °C and annealed at 450 °C in N ₂ | 2014 | [40] |
| VO ₂ NPs on fused quartz substrate | — | t: 150 nm | RF magnetron sputtering | Vanadium metal target | RF power: 100W; 600 °C for 1 h at 2–20 Pa, lamp annealing under O ₂ | 2017 | [41] |
| VO ₂ NPs on glass substrate with porous AAO mask | — | — | DC magnetron sputtering | Vanadium metal target | DC power: 400V; annealing 380 °C for 4 h under O ₂ | 2015 | [42] |
| VO ₂ thin films on a quartz substrate | — | rms:207 nm | spray pyrolysis | V ₂ O ₅ , Combustion mixture: vanadyl nitrate and urea | 400 °C ultrasonic nebulized spray | 2019 | [49] |
| VO ₂ thin films on LaAlO ₃ substrate | — | Film thickness: 400 nm | spray pyrolysis | V ₂ O ₅ , Combustion mixture: vanadyl nitrate and urea | 400 °C ultrasonic nebulized spray | 2015 | [50] |
| VO ₂ (M) film | — | — | Combustion-assist fabrication | Vanadyl (IV) acetylacetone/ethanol | Ignited and allowed to combust completely | 2010 | [51] |
| VO ₂ thin film | — | Less than 0.5 μm | Pulsed laser deposition | Vanadium metal target | Wavelength: 248nm, pulsed time: τ= 15ns; substrate temp: 500–525 °C, annealing for 1 h | 1993 | [43] |
| VO ₂ thin film | — | d: 45 nm in center, 75 nm at border | Pulsed laser deposition | Vanadium metal target | Wavelength: 248nm, τ= 250 fs; substrate temp: 25 & 500 °C | 2009 | [44] |
| VO ₂ phase on Si substrate | — | — | Pulsed laser deposition | V ₂ O ₅ | Wavelength: 248nm, laser: 210 mJ; fluence: 3 J/; substrate temp: 650 °C, annealing 650 °C under O ₂ | 2016 | [45] |
| VO ₂ thin film on Si substrate | — | Surface roughness:3–5 nm | Pulsed laser deposition | Vanadium metal | 2.6 J cm ⁻² KrF excimer laser; 10 Hz for 15 min; substrate temp: 600 °C; base pressure: 10 ⁻³ mTorr; pO ₂ : 50 mTorr | 2018 | [2b] |
| VO ₂ thin film | — | t: 80–100 nm | Pulsed laser deposition | V ₂ O ₅ | Sintering at 690 °C in air for 12 h; 1.5 J cm ⁻² KrF excimer laser; Ts: 350–600 °C; pO ₂ : 5–200 mTorr | 2015 | [46b] |
| VO ₂ nanofiber | 1D | t: 300–400nm | Sol-gel electrospinning | V ₂ O ₅ & PVP / H ₂ O ₂ | Pump flow: 0.5 mL h ⁻¹ ; potential diff: 15–18kv; heating at 60–80 °C and annealing in air and Ar atmosphere | 2020 | [53] |
| VO ₂ nanoparticles porous thin film | — | 100–300 nm | Sol-gel | cetyltrimethylammonium vanadate (CTAV), 1-butanol | Dip coating using CTAV at 5–300 mm min ⁻¹ rate; drying at 60 °C for 30 min; annealing at 50 °C in the air; reduction of V ₂ O ₅ film by H ₂ /Ar gas at 430–450 °C for 10–40 min | 2013 | [56] |
| Thin films of VO ₂ nanoparticles | — | VO ₂ NPs below 10 nm | Sol-gel | V ₂ O ₅ , WO ₃ | Spin coating followed by annealing and reduction at 500 °C for 2 h | 2015 | [57] |

l = length; *w* = width; *t* = thickness; *d* = diameter.

ethylene glycol water mixture at 160 °C for 3h.^[64] Authors carried out TEM to confirm the formation of nanosheets, which suggested that VO₂ is composed of parallel ultrathin 2D nanosheets with diameter 50–60 nm and hundreds of nanometer length (Figure 7d–e).

Rahman et al. synthesized VO₂(B)-multiwall carbon nanotube (MWCNT) microsheets composite by in situ hydrothermal method.^[65] Briefly, first, the surface of MWCNTs was

functionalized by treating them with a mixture of H₂O₂ and sulfuric–nitric acid using reflux method at 120 °C for 2 h. Thereafter, the obtained mixture was washed with water and dried. For the synthesis of composite, a mixture of treated MWCNTs, V₂O₅, n-butanol, and water was filled in the autoclave and then kept in an oven at 180 °C for 48 h. The product is washed and dried, then heated at 250 °C for 10 h in an argon atmosphere.

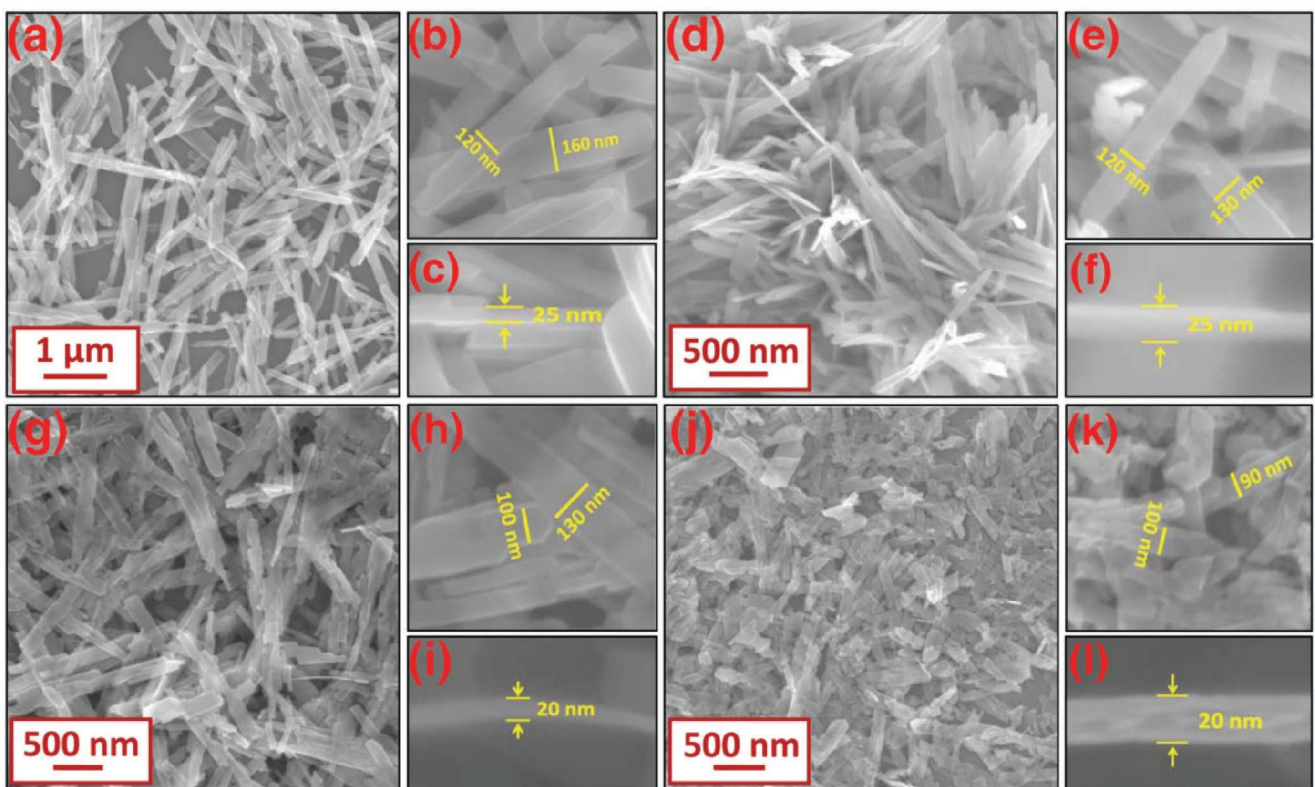


Figure 6. FE-SEM images of $\text{VO}_2(\text{B})@\text{C}$ nanobelts a–c) weight ratio 5, d–f) weight ratio 2.5, g–i) weight ratio 1.67, and j–l) weight ratio 1.25. (b, e, h, and k) and (c, f, i, and l) are the high-resolution images of $\text{VO}_2(\text{B})@\text{C}$ nanobelts presenting the estimated dimensions of the prepared nanobelts, respectively. Reproduced with permission.^[61] Copyright 2012, The Royal Society of Chemistry.

In general, the morphological analysis suggested that composite has a sheet-like structure, and these nanosheets were grown together to form bundles. On closer inspection, these MWCNTs were distributed randomly and located underneath

of $\text{VO}_2(\text{B})$ nanosheets/bundle.^[65] Vertically aligned $\text{VO}_2(\text{B})$ nanobelts forests were also synthesized by the hydrothermal method on vertically oriented graphene (VOG).^[66] Graphene was first grown on a flat substrate such as graphite, Ni foil

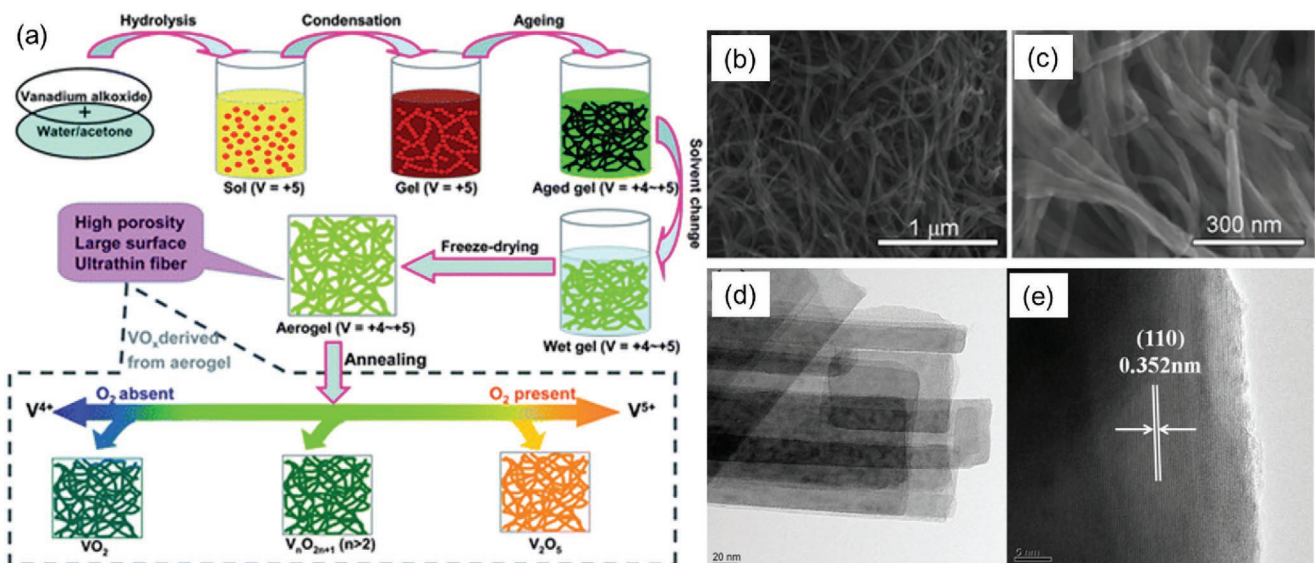


Figure 7. a) Schematic illustration for the synthesis of $\text{V}_2\text{O}_5 \times \text{H}_2\text{O}$ aerogels and other vanadium oxides using aerogels. b) low and c) high-resolution SEM images of $\text{VO}_2(\text{B})$ fibers. Reproduced with permission.^[63] Copyright 2011, The Royal Society of Chemistry. d,e) The TEM and HR-TEM images of prepared VO_2 nanosheets by hydrothermal method. Reproduced with permission.^[64] Copyright 2014, Elsevier.

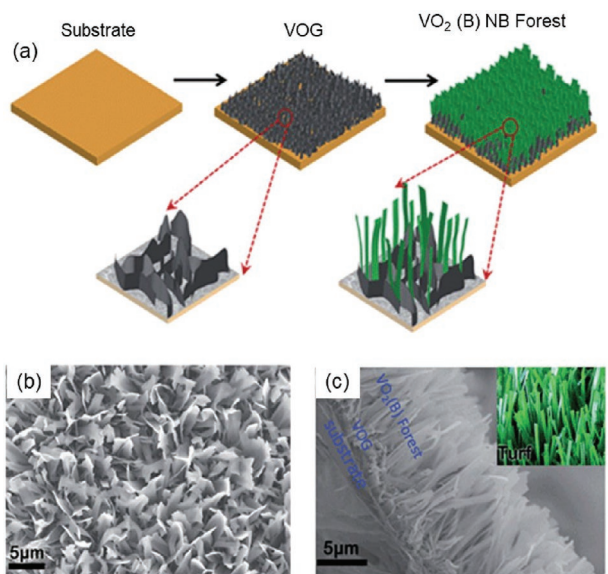


Figure 8. a) Graphitic illustration for the growth of VO_2 (B) nanobelts-based forest structure on VOG coated on a flat substrate. b) Vertical and c) cross-sectional SEM images of VO_2 (B) nanobelts forest showing the width of individual nanobelts. The inset of (c) shows a photo of artificial turf to compare. Reproduced with permission.^[66] Copyright 2015, The Royal Society of Chemistry.

or Ni foam, etc. by microwave plasma-enhanced chemical vapor deposition (PECVD) method.^[67] The prepared VOG sample was kept in an autoclave with V_2O_5 , isopropanol, and water solution at 160–180 °C for 48 h. The synthesis scheme is shown in **Figure 8a**. The vertical thickness of VOG grown from PECVD was estimated \approx 1 μm from SEM. After

hydrothermal treatment, vertically aligned densely packed VO_2 (B) nanobelts assembled and formed a forest-like structure confirmed from cross-sectional view (Figure 8b–c). The detailed growth mechanism was provided in the article by studying morphology with the time of hydrothermal treatment. To show the universality, the authors had also grown the forest of VO_2 (B) nanobelts on Ni foam.

3.2.3. 3D VO_2 Nanostructure

Liu et al. synthesized 3D VO_2 (B) hollow microspheres by hydrothermal method.^[68] Briefly, the authors mixed V_2O_5 , glucose, and aniline by stirring up to 5 h, then transferred the reaction mixture in an autoclave and heated it up to 180 °C for 48 h. Authors carried out a controlled experiment to understand the formation of nanothorn VO_2 (B) hollow microspheres (as presented in **Figure 9a–c**). In absence of either aniline or glucose, the formation of nanobelts was observed; however, these microspheres were observed when both are present in the reaction mixture. In presence of both, aniline act as a reductant whereas, glucose first self-organized to form carbon spheres and then functioned as a structure-directing template.^[68] TEM confirmed the formation of hollow microspheres having porous and rough surfaces and the thickness of the shell was about 100–200 nm (shown in Figure 9d–f). The selected area diffraction pattern showed that formed VO_2 (B) spheres are polycrystalline in nature (inset of Figure 9d).

In 2009, Zhang et al. reported a low-temperature method to prepare flowerlike metastable VO_2 (B).^[21c] In the earlier adopted method, VO_2 was mainly synthesized by the thermal evaporation method which requires high temperature and vacuum.

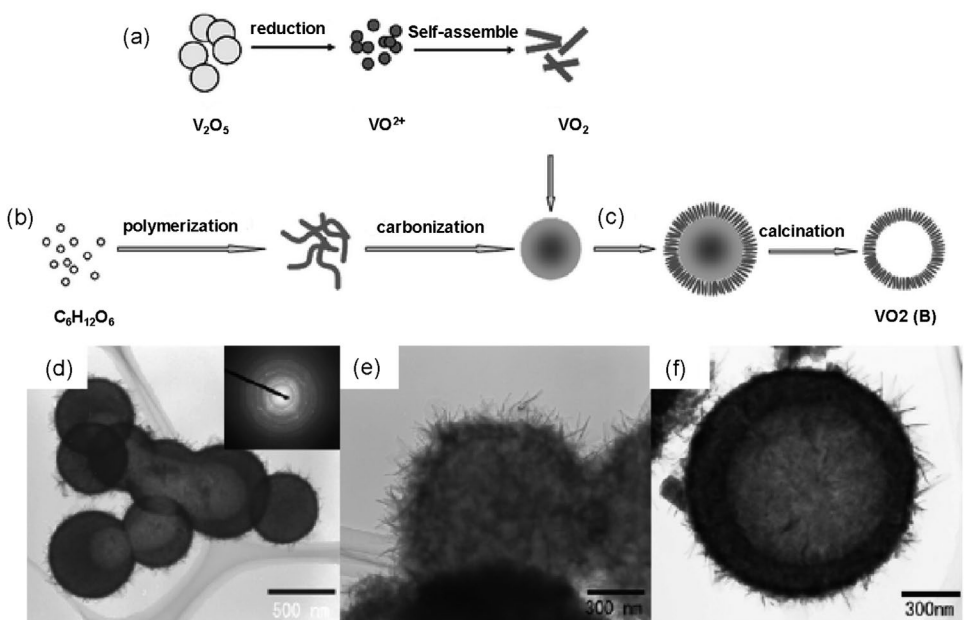


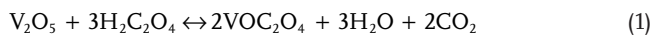
Figure 9. a) Schematic of V_2O_5 reduction to VO_2 nanoparticles and nanothorns. b) Glucose polymerization and carbonization to carbon spheres. c) Formation of VO_2 (B) hollow spheres. d) Low-resolution and e,f) show high-resolution TEM images of nanothorn VO_2 (B) hollow microspheres. Reproduced with permission.^[68] Copyright 2009, The Royal Society of Chemistry.

In further advancement, the hydrothermal method and surfactant assisted routes were used. However, in these solution-based methods, the formation of low valent vanadium oxide depends on reactants which may lead to the presence of impurity in the final product. To avoid this, Zhang et al. developed a reductant-free method which involved mixing of $\text{VO}(\text{acac})_2$ in polyvinyl pyrrolidone (PVP) solution and heating this solution in an autoclave at 200 °C for 24 h.^[21c] This method produced uniform architecture built with interconnected 20–30 nm thick nanopetals arranged in a way to yield flowerlike morphology, having a diameter in the range of 1–1.5 μm. Additionally, the authors also found different morphology such as belt, flower, and carambola shaped VO_2 (B) using different concentrations of PVP. These reported methods involved either higher temperature or prolonged heating to achieve a highly crystalline and pure phase of VO_2 . Xu et al. used montroseite VOOH having hollow nanourchin shape to synthesize paramontroseite VO_2 by simply heating at 120 °C for 6 h in air.^[23b] Interestingly, the authors observed no change in phase post-heat treatment. The size of formed hollow nanourchins was found to be in the 700–800 nm range as confirmed by SEM. Wang et al. synthesized 3D C/ VO_2 (B) composite microspheres by a facile one-step synthesis in order to improve the cyclic stability of VO_2 (B).^[69] Authors claimed that coating of material with carbon improved its electronic conductivity. In a typical synthesis, in the mixture of NH_4VO_3 and sucrose, sodium peroxocarbonate (Na_2CO_4) was added and the obtained solution was treated under hydrothermal condition at 200 °C for 24 h. The prepared sample was washed with pure water and absolute ethanol before drying at room temperature. Ni et al. varied the concentration of oxalic acid and hydrothermal reaction time to investigated their effect on the morphology of VO_2 (B).^[70] VO_2 (B) nanorods were produced at 0.08 mol L⁻¹ oxalic acid concentration and at 180 °C temperature, for VO_2 (B) nanoflakes synthesis temperature was kept constant while the concentration of oxalic acid was slightly increased (from 0.08 mol L⁻¹ to 0.1 mol L⁻¹). Authors observed VO_2 (B) nanoflowers at a higher oxalic acid concentration (0.12 mol L⁻¹) and higher temperature (200 °C). These nanoflowers were comprised of 800 nm wide and 100 nm thick nanobelts.

In addition to VO_2 (B), Won et al. synthesized VO_2 (R)-carbon microspheres by heat treatment in air atmosphere.^[71] Herein, PVP was utilized as a carbon source whose presence affected the morphology, crystal structure, and also electrochemical properties. For the synthesis of VO_2 (R)-carbon composite, first V_2O_3 -carbon composite was prepared by spray pyrolysis which was then heated at 300 °C for 1 h in the air to get VO_2 (R)-carbon microspheres. Authors observed that the presence of PVP played a key role in deciding the morphology. When there is no PVP in the reaction precursor, rod- and sphere-like mixed morphology was observed, however, the presence of PVP lead to the formation of microspheres. Rutile phase has not been studied as much as the metastable phase for LIBs, nonetheless, rutile electrodes suffer from stable reversible capacity due to the formation of an irreversible structure during deep Li⁺ ion insertion.^[72] Park et al. carried out a conceptual study using heteroepitaxial engineering to improve the performance of VO_2 (R) which involves surface reconstruction of an epilayer induced by a number of strain relief processes which resulted in the

growth of nanostructured surface with specific facets.^[72,73] Using this engineering method, exposure of highly reactive facets was achieved which significantly improved the kinetics of lithium diffusion and also Li⁺ ion activity. In this method, the most critical point was finding an appropriate substrate that can accommodate anisotropic volume change during the expansion/shrinkage in *ab* plane thru Li⁺ ions intercalation/deintercalation. For VO_2 (R), SnO_2 can be a good choice as it has larger *a*- and *b*-axes (0.474 nm) than VO_2 (0.455 nm) which can easily accommodate 4.2% growth of VO_2 . Park et al. strategically grown rutile VO_2 (M/R) nanobranches on rutile Sb: SnO_2 (ATO) as presented in Figure 10a.^[72] This novel heterostructure can provide i) high electrode/electrolyte interfacial area ii) fast transport of charge carriers, and iii) improved Li⁺ ion diffusion through (002) facets and higher Li⁺ ion accommodation.

For further advancement, Chao et al. synthesized graphene quantum dots (GQDs) coated VO_2 arrays on graphene foam by solvothermal method.^[4a] The prepared electrode was a binder-free electrode that was grown on graphene foam by an ultralight, highly porous, and conductive substrate. Also, the prepared electrode is binder-free which prevents usage of binder, conductive additive, and current collectors (such as Al/Cu foil) that helps to reduce total the weight of electrode. Typical synthesis involved the mixing of V_2O_5 and oxalic acid in water, ethanol, and hydrogen peroxide mixture. Finally, graphene foam prepared by the CVD method was dipped in the solution, and autoclave was heated at 180 °C for 3h. For coating GQDs, authors first prepared GQDs by solvothermal method and then coated it on VO_2 nanoarrays on graphene foam by electrophoresis process. The growth mechanism was explained by self-assembly and oriented crystallization processes. During the solvothermal condition, V_2O_5 was reduced to VOC_2O_4 which nucleated onto graphene foam. Due to strong crystal anisotropy, the particle grows and forms a belt-like structure of monoclinic VO_2 . Later, Li et al. fabricated flexible electrodes by growing VO_2 nanobelts on top of carbon cloth by the hydrothermal method by modifying the previous method (Figure 10b).^[74] The homogenous growth of VO_2 (B) nanobelts on carbon cloth can be seen in SEM images (Figure 10c–e). The prepared electrode displayed well distributed VO_2 nanobelts arrays with an average length ranging 359–900 nm and 50–100 nm thicker. The formation of nanobelts was confirmed by HRTEM (Figure 10f).



Chen et al. also synthesized VO_2 nanoarrays decorated with N-doped carbon on carbon cloth by solvothermal method.^[75] The preparation method is almost the same as described above; however, to synthesize pure VO_2 nanoarrays, authors annealed the as-prepared sample at 450 °C for 3 h in Ar and H₂ mixture. Furthermore, to coat N-doped carbon, the authors dipped the above sample in dopamine hydrochloride and water solution and left it for self-polymerization at 80 °C for 3 h. Later, the sample was annealed again at 500 °C under Ar atmosphere to obtained N-doped carbon on VO_2 nanoarrays

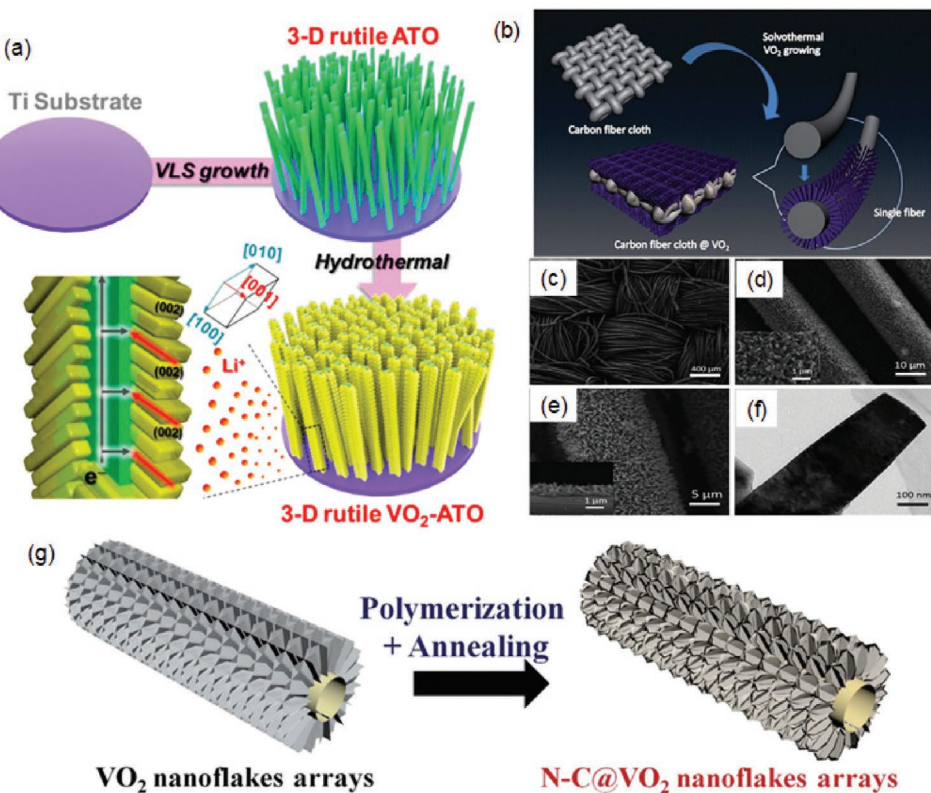


Figure 10. a) Graphitic presentation for the fabrication of 3D hierarchical VO₂–ATO nanobelt arrays. Reproduced with permission.^[72] Copyright 2016, The American Chemical Society. b) Schematic presentation of the growth of the VO₂ nanobelt array nanostructure on carbon cloth. c) Low and d,e) high-resolution SEM images and f) TEM of VO₂ nanobelts. Reproduced with permission.^[74] Copyright 2016, The Royal Society of Chemistry. g) Graphitic illustration of the fabrication of N-doped carbon coated VO₂ core-shell arrays. Reproduced with permission.^[75] Copyright 2019, The Royal Society of Chemistry.

(Figure 10g). Yan et al. synthesized crumpled reduced rGO coated VO₂ microspheres by solvothermal method.^[76] Here, the authors first synthesized GO by modified Hummers method and obtained sample was ground into a fine powder then dispersed in ethylene glycol by sonication. Later, a dark blue VOC₂O₄ precursor solution was prepared by mixing V₂O₅ and oxalic acid. These two solutions were mixed in an appropriate amount and hydrothermally treated at 200 °C for 8 h to get rGO coated VO₂ spheres. SEM images confirmed that VO₂ crystallized as microspheres with an average diameter of ≈500 nm and were encapsulated properly by crumpled graphene. This method can be a handful method to prepare uniformly encapsulated electrode material with rGO which is a challenging task. Authors also proposed the formation mechanism as shown in Figure 11a. First, the formation of VO₂ nuclei took place at higher temperature due to the hydrolysis of VOC₂O₄ (Equation 2). These formed nuclei aggregated and transformed into nano-microspheres in order to reduce the surface energy. At stage II, GO was reduced to scrap nanosheets on the surface of VO₂ nano-microspheres due to electrostatic attraction and surface energies. At stage III, stacking and crimping process occurred which lead to the formation of rGO encapsulated VO₂ microspheres.

To prepare a binder-free and conductive electrode, Khan et al. grew carambola-shaped VO₂ nanostructures on porous

rGO coated carbon paper (Figure 11b), and the prepared electrode was utilized as an air electrode for hybrid Na-air battery.^[77] Prior to VO₂ growth, the authors first coated porous rGO on carbon paper by hydrothermal method. GO was prepared by modified Hummers method and then it was dispersed in water, followed by addition of polystyrene beads and sonicated thoroughly. The solution was transferred in Teflon-lined stainless-steel autoclave and carbon paper of desired size was immersed in a solution which was then treated hydrothermally. After hydrothermal treatment, the carbon paper was first washed with water and then with toluene to remove polystyrene and to obtain porous rGO coated carbon paper. Later, this carbon paper was kept in a solution of NaVO₃, sodium dodecyl sulfate, and oxalic acid for further hydrothermal treatment (180 °C for 24 h) which leads to the formation of carambola shaped VO₂ nanostructures on porous rGO coated carbon paper. It would be worth to mention here that without porous rGO, growth of spherical shaped VO₂ on carbon paper was observed.^[77] SEM confirmed the formation and uniform growth of six armed nanostructures with an average height of 3 μm and a width of 2 μm (Figure 11c–f). The formation of carambola shape takes place by self-assembly of 20–50 nm thick VO₂ layers. Later, a 3D flower-like VO₂/MXene hybrid nanoarchitecture was synthesized to improve the conductivity and structural stability of VO₂.^[78] Ti₃C₂T_x (MX) was first

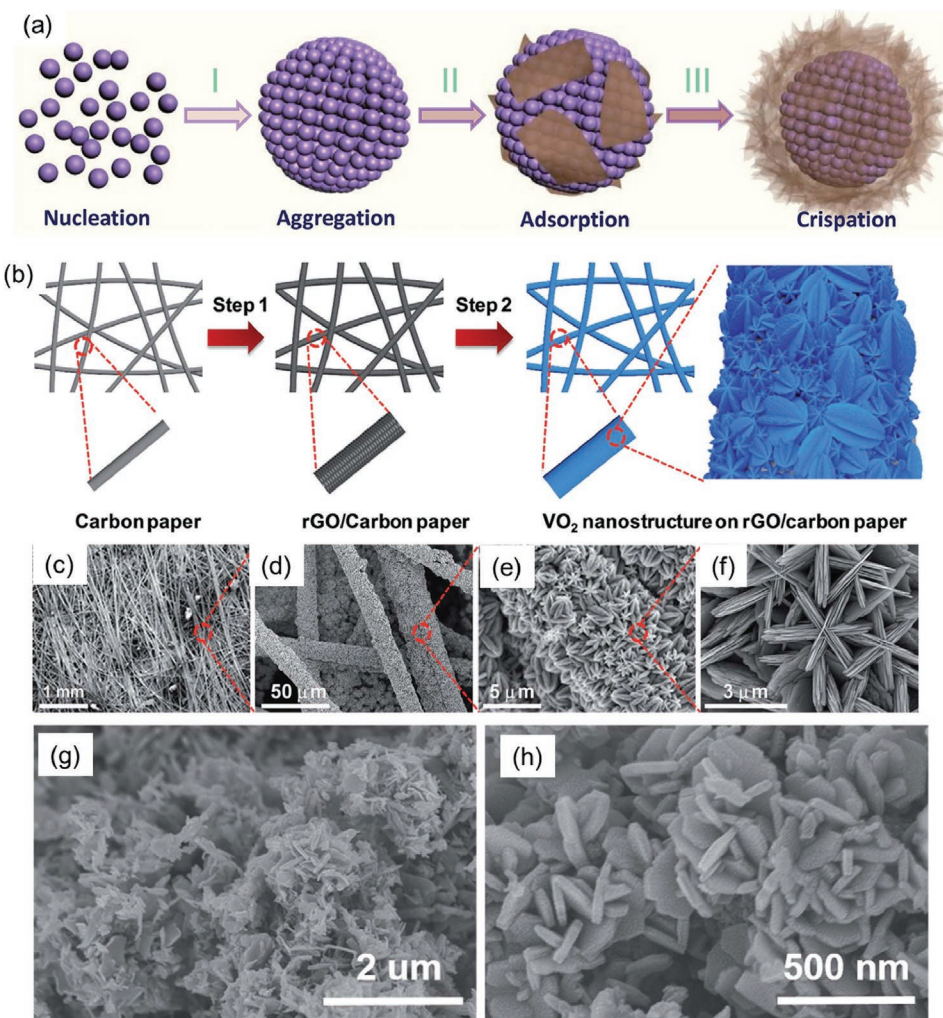


Figure 11. a) A time-dependent schematic illustration for the synthesis of rGO coated VO₂ spheres. Reproduced with permission.^[76] Copyright 2017, The Royal Society of Chemistry. b) Graphical presentation for the growth of carambola shaped VO₂ nanostructures on reduced GO coated carbon paper; c,d) low and e,f) high-resolution SEM images confirmed the uniform formation of carambola shape VO₂. Reproduced with permission.^[77] Copyright 2017, The Royal Society of Chemistry. g,h) Presents different magnification SEM images of VO₂/MXene composite. Reproduced with permission.^[78] Copyright 2019, The Royal Society of Chemistry.

synthesized by treating Ti₃AlC₂ powder in hydrofluoric acid and the obtained powder was collected by centrifugation and dried to get MX powder. The obtained MX was then dispersed in water followed by the addition of vanadyl acetylacetone and hydrochloric acid. The reaction mixture was finally treated hydrothermally at 180 °C for 24 to get novel nanocomposite (VO₂/MX). The prepared composite showed 3D flower-like morphology resulted from self-assembly of hybrid nanosheets of VO₂ and MX (Figure 11g–h).

4. Energy Storage Application of VO₂ Nanostructure

Density functional theory (DFT) calculation of monolayer VO₂ suggested that it can be utilized in Li, Na, K, Mg, and Ca ion batteries due to their excellent mobility with lower

diffusion barrier such as 0.119 eV for Li, 0.098 eV for Na, 0.043 eV for K, 0.517 eV for Mg, and 0.306 eV for Ca. Authors also calculated the high open-circuit potentials which were 1.56 V for Li, 0.98 V for Na, 2.36 V for K, 1.21 V for Mg, and 2.82 V for Ca. Also, the estimated specific capacities can be reached up to 968, 613, and 815 mAh g⁻¹ for Li, Na, and Mg respectively that made VO₂ an attractive choice electrode material for batteries.^[85] In the following subsections, we are presenting systematically the applications of VO₂ in Li⁺ ion, Na⁺ ion, Mg²⁺ ion, and Zn²⁺ ion batteries and in supercapacitors.

4.1. Li-Ion Battery Application

During 1980s, LIBs technology was developing quickly because LIBs showed higher specific energy than the best competing

batteries. Most cells were built up using Li as negative electrode and metal oxide such as MnO_2 was chosen as positive electrode.^[86] The charge storage mechanism was explained based on the reversible Li^+ ion intercalation ability of positive electrode. For intercalation of Li^+ ion, the host should have a layered or tunneled structure in which intercalated Li reside. The feasibility of Li intercalation into host lies due to the reason that the chemical potential of Li can be lowered by Li insertion which leads to chemical bond formation.^[86] Since Whittingham showed the usage of layered material as cathode in Li^+ ion battery in 1976,^[87] research to find other layered materials speeded up. After four years in the 1980s, Christian et al. showed the Li^+ ion storage property of VO_2 (B).^[24] A Li-ion cell was built up using $\text{VO}_{2.122}$ as cathode material which showed 35% capacity degradation within 15 cycles.^[24] Ten years later, Dahn et al. revisited VO_2 (B) and adopted a different synthesis approach in order to improve the capacity decay.^[88] Authors showed that cells built by lithium anode and VO_2 (B) cathode did not show any capacity fading up to 20 cycles. Since then, numerous studies were carried out using VO_2 as efficient electrode material for LIBs. In 1994, Li et al. fabricated an aqueous electrolyte-based LIB to avoid price issues related to non-aqueous cells, using LiMn_2O_4 and VO_2 (B) as electrode materials with 1 mM LiOH electrolyte.^[86] The 1.5 V cell displayed excellent repeatability and a maximum of 75 Wh kg^{-1} specific energy higher than Pb-acid ($\approx 30 \text{ Wh kg}^{-1}$) and Ni-Cd (50 Wh kg^{-1}) well-established technologies.

Since, VO_2 (B) is a metastable polymorph, its synthesis in pure form isn't easy due to its irreversible phase transformation to the rutile phase above 537°C . Tsang et al. used potassium borohydride reduction method to synthesize pure VO_2 (B) phase which exhibited a maximum of 320 mAh g^{-1} specific capacity and good cyclability for LIBs. Later, Kannan et al. synthesized metastable VO_2 (B) phase at an ambient condition which displayed high reversible capacity $> 300 \text{ mAh g}^{-1}$ in 3.5 V to 1 V at 0.5 mA cm^{-2} current density with decent cyclability in temperature range -30 to 60°C .^[89] Here authors have explored the possibility of using VO_2 (B) in different temperature ranges. Wen et al. prepared VO_2 (B) nanorods with 1–2 mm length and 40–60 nm diameter by hydrothermal method.^[90] VO_2 (B) nanorods displayed an initial 306 mAh g^{-1} specific capacity which reduced to 20% (245 mAh g^{-1}) in 15th cycle. Though VO_2 (B) displayed good capacity, yet degradation in the capacity required improvement. In mid-2006, VO_2 (B) nanotextured aerogels were produced at low temperature and used it for LIBs.^[91] Authors observed that temperature has an impact on the electrochemical behavior of the material. The aerogel's galvanostatic charge-discharge curve was featureless when heated at 280°C , however, upon heat treatment at 400°C two well-defined redox peaks appeared in CV curves (Figure 12). The nondimensional VO_2 (B) phase formed by heating 280°C delivered a maximum of 500 mAh g^{-1} specific capacity (relatively higher than the sample prepared by heating at 400°C) and decent cyclic stability in 4–1.5 V versus Li voltage range. The capacity decay was fast in the potential range 4–1.5 V than 4–2.4 V (vs Li) which was attributed to the dissolution of vanadium at low potential range.

Ultra-thin ($< 10 \text{ nm}$ diameter) VO_2 (B) NWs prepared by solvothermal method showed 265 mAh g^{-1} of specific capacity

which was found to be higher than standard NWs ($50\text{--}100 \text{ nm}$ diameter).^[58] Also, the cyclic stability was observed better than standard NWs. However, the capacity obtained here is lower than the capacity of VO_2 (B) aerogel explained above. In early 2008, Wu et al. synthesized paramontroseite VO_2 different polymorphs having walnut like nanoarchitectures and showed its application in aqueous LIBs.^[23a] Authors built a full cell with LiMn_2O_4 and tested the cell in 5 M LiNO_3 and 0.001 M LiOH aqueous electrolyte. The 1.2 V cell showed 61.9 mAh g^{-1} of specific capacity at 60 mA g^{-1} which reduces to $\approx 46 \text{ mAh g}^{-1}$ in 50 cycles. Liu et al. synthesized 3D nanothorn VO_2 (B) microspheres and used them as cathodes for LIBs.^[68] The prepared nanostructure showed reduction and oxidation peak at 3 and 3.7 V versus Li, respectively related to the insertion and extraction of Li^+ ions in the tunnel of VO_2 (B). Also, the electrode displayed 450 mAh g^{-1} of specific capacity at 10 mA g^{-1} of current density and no decay in capacity up to 50 cycles at higher current density (50 mA g^{-1}). This performance was credited to the formation of a rigid 3D structure with nanothorns arranged vertically on the surface, avoiding the aggregation of active materials during cell operation. Another possible reason would be the highly porous nature of the material which allowed the diffusion of electrolytes and ions.^[68] Zhang et al. studied LIB performance using different morphology of VO_2 (B) in aqueous electrolytes.^[21c] $\text{VO}_2/\text{LiMn}_2\text{O}_4$ based aqueous cell displayed 74.9, 62.1, and 58.3 mAh g^{-1} of specific capacity for flowers, nanobelts, and carambola shaped VO_2 (B), respectively. The specific capacity retentions up to 50 cycles were observed 41.5, 46, and 38% for flower, nanobelts and carambola shaped material. Not only, the flowerlike VO_2 (B) based cell showed the highest discharge capacity but also displayed decent cyclic stability up to 50 cycles. Further, the authors also heated the prepared flowerlike VO_2 (B) sample at 350°C to synthesize highly crystalline VO_2 and investigate its effect on LIB performance. The post treated sample did not show any significant change in morphology, however, it showed the highest specific capacity of 81.3 mAh g^{-1} at 60 mA g^{-1} , and also, it retained almost 67% of

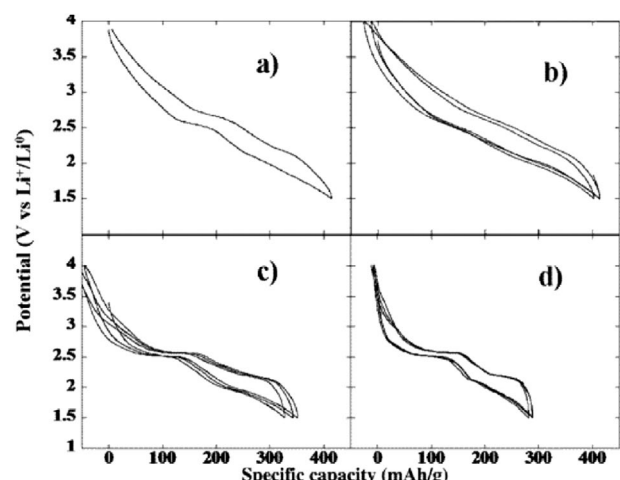


Figure 12. Potential versus specific capacity plots of a) vanadium oxide aerogel with VO_2 (B) prepared by heating at b) 280°C , c) 320°C , and d) 400°C ; all data recorded at C/20 rate. Reproduced with permission.^[91] Copyright 2006, The American Chemical Society.

initial capacity up to 50 cycles. The high performance was attributed to the highly crystalline structure, high aspect ratio, and high specific surface area which reduced the path length for Li^+ ion diffusion thereby, making the intercalation and de-intercalation processes much smooth. Xu et al. synthesized hollow nanourchin shaped paramontroseite VO_2 and investigated its performance in aqueous LIBs.^[23b] An aqueous cell was built using LiMn_2O_4 as cathode and hollow nanourchin paramontroseite VO_2 as anode electrode materials with 5 m LiNO_3 and 1 m LiOH mixture as the aqueous electrolyte. The paramontroseite VO_2 can be a potential anode material for LIBs due to not only its proper working electrode potential, but also its unique tunneled structure. The ionic size of Li^+ ions (1.36 Å) is smaller than the tunnel size in paramontroseite VO_2 (2.446 Å × 4.946 Å) in the supercell crystal structure which allows efficient intercalation/deintercalation of Li^+ ions in paramontroseite VO_2 . The device displayed a maximum of 72.1 mAh g⁻¹ of specific discharge capacity at 60 mA g⁻¹ of current density and also retained 39.1% of its initial capacity up to 50 cycles. The increased electrochemical performance was credited to the synergistic effect of microscopic tunneled crystal structure and macroscopic hollow morphology which not only provided a shorter path for Li^+ ion diffusion but also the proper size for Li^+ ion accommodation. Different morphologies of VO_2 such as aerogel, flower like, ultra-thin NWs, 3D nanothorn, and hollow nanourchin, etc. were explored to improve specific capacity and cyclic stability. The performance in terms of specific capacity was found improved but capacity degradation with cycle is still poor which might be due to the conductivity of electrode and volume changes in crystal structure during the charge-discharge process.

In order to improve the conductivity of the electrode and thus its performance, Rahman et al. synthesized MWCNT/ VO_2 (B) composite and investigated it as a cathode for LIBs.^[65] Authors analyzed electrochemical performance in voltage range 2–3.25 V versus Li. The composite displayed 177 mAh g⁻¹ discharge capacity, good cyclic stability up to 100 cycles (92% retention in initial capacity) and rate capability compare to VO_2 (B). The better rate capability of VO_2 (B) could be attributed to the improved ionic conductivity of composite as evaluated by the Nyquist plot. Also, the exceptional cyclic stability could be credited to the fact that composite prevented the formation of aggregation of active material and accommodate the huge volume change during charge-discharge cycles. Li et al. synthesized fibrous VO_2 (B) by annealing $\text{V}_2\text{O}_5 \cdot x\text{H}_2\text{O}$ aerogel to use the advantage associated with aerogel structure.^[63] The fibrous structured 3D VO_2 (B) aerogel was tested for LIBs displayed three broad reduction peaks at 2.6, 2.3, and 1.8 V versus Li and two prominent oxidation peaks which were attributed to the reversible insertion/de-insertion of Li^+ into VO_2 (B) interlayer or interlayer sites. Also, the material shows a higher specific capacity of 410 mAh g⁻¹ at C/8 rate than $\text{V}_2\text{O}_5 \cdot 0.5\text{H}_2\text{O}$ xerogel (340 mAh g⁻¹ at C/55) and good cyclic stability up to 20 cycles (80% retention).

Nethravathi et al. used VO_2 nanotubes-graphene hybrid composite as cathode in organic electrolyte.^[59] Indeed, the charge transport susceptibility was found much higher in 1D nanostructures than bulk, however, they displayed rapid

capacity degradation and poor cyclic stability owing to its higher surface energy which results in aggregation and collapse of the 1D structure.^[59] To avoid these drawbacks, the authors synthesized VO_2 nanotubes-graphene hybrid composite. The hybrid composite delivered 450 mAh g⁻¹ of specific capacity at 40 mA g⁻¹ of current which was found to be higher than the theoretical maximum capacity (320 mAh g⁻¹). Authors also observed fast charge and discharge reversible capacities attributed to the presence of graphene matrix which helped to improve the charge transfer properties to and from VO_2 (B) nanotubes. Also, the hybrid composite showed 71% capacity retention in 20 cycles at 40 mA g⁻¹ current. Indeed, the reported VO_2 nanostructures displayed improved specific capacity, but their rate capability and cyclic stability were not reasonable. To improve the performance of VO_2 (B) further, Rui et al. synthesized carbon coated VO_2 (B) nanobelts by hydrothermal method.^[61] Coating of thin carbon layer on VO_2 (B) nanobelts can help to improve the kinetics of charge transfer, sustain the structural or volume changes, and also prevent the aggregation of electrode material during cycling. The optimal thickness of carbon was found to be 4.3 nm which showed high specific capacity (161 mAh g⁻¹), good cyclic stability (~80% retention), and superior rate capability (136 mAh g⁻¹ at 6.2 C whereas, 100 mAh g⁻¹ at 12.4 C rate). In 2012 Nethravathi et al. showed that VO_2 nanotubes-graphene hybrid composite can exhibit 450 mAh g⁻¹ of specific capacity but, this composite displayed poor rate capability.^[59] To improve the rate capability further, Nethravathi et al. synthesized 3D VO_2 (B) flower-like nanostructure uniformly distributed on N-doped graphene.^[92] The hybrid composite displayed 418 mAh g⁻¹ of maximum specific capacity and good cyclic stability (60% retention). The specific capacity decreased from 418 to 102 mAh g⁻¹ when current was increased from 0.05 to 5 A g⁻¹, which is better than the pristine VO_2 (B). Though it was claimed that rate capability has been improved, but it is still beyond the satisfactory limit. The improved performance was attributed to improved electronic conductivity, short diffusion path for Li^+ ions, and enhanced charge transfer. Yang et al. used a bottom-up approach to prepare VO_2 -graphene ribbons as cathode material for ultrafast Li^+ ion storage (**Figure 13a**).^[4c] The single crystalline VO_2 ribbon with thin graphene layer provided high specific capacity 415 mAh g⁻¹ at 1C rate (**Figure 13b**) and displayed ultrafast charging and discharging capabilities as fairly reversible capacities as high as 222 and 204 mAh g⁻¹ were observed at exceptionally high rates 84 and 190 C, respectively (**Figure 13c**). At 190 C ultrahigh rate, the cell capacity decreased to 190 mAh g⁻¹ in 1000 cycles which is almost 90% retention in specific capacity (**Figure 13d**). Also, the specific power was estimated as 110 kW kg⁻¹. He et al. synthesized a 1D g- VO_2 composite electrode and tested its performance and stability for LIBs beyond 1 V.^[60] First authors carried out electrochemical performance investigation in 3.3–1.5 V versus Li at 100 mA g⁻¹ which showed 175 mAh g⁻¹ of initial specific capacity and 162 mAh g⁻¹ reversible capacity from the 2nd cycle. Further, the cell was tested in 3–0.05 V versus Li window where cell showed 692 mAh g⁻¹ of initial discharge capacity and stabilizes around 450 mAh g⁻¹ for the second consecutive cycle.

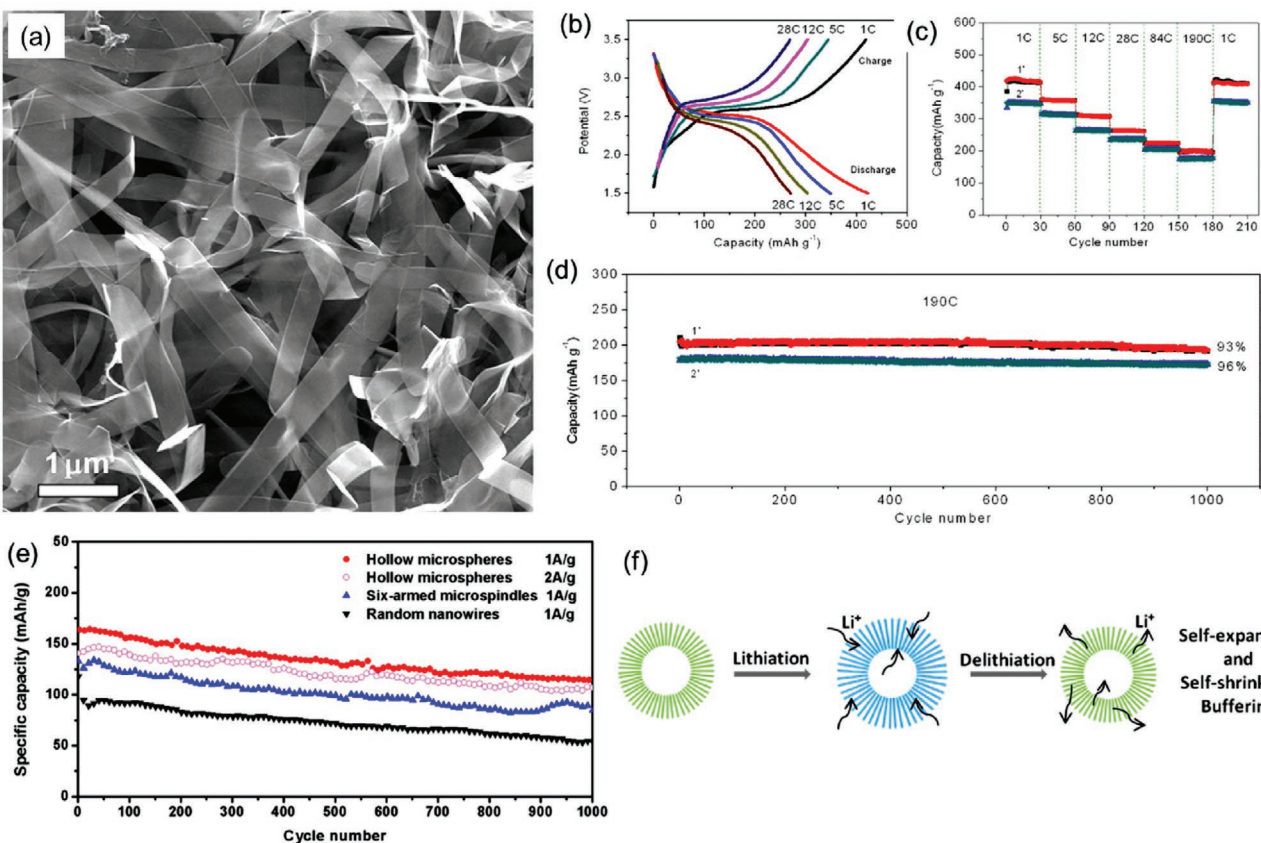


Figure 13. a) SEM images of VO_2 -graphene nanoribbons prepared by 12 h hydrothermal treatment; b) charge-discharge curve, c) rate capability at different rates ranging from 1C to 190 C, and d) cyclic stability of VO_2 -graphene nanostructure for 1000 cycles. 1' and 2' presents composite with different VO_2 contents 78% and 68%, respectively. Reproduced with permission.^[4c] Copyright 2013, The American Chemical Society. e) Comparative cyclic stability analyses of hollow microspheres, six-armed microspindles, and random NWs in 2–3 V range; f) Schematics of the structural stability of hollow microspheres during lithiation and delithiation. Reproduced with permission.^[94] Copyright 2014, The American Chemical Society.

Also, cell displayed 400 mAh g^{-1} of specific capacity up to 400 cycles showing stable performance. Ex situ XRD analysis of electrode suggests a reduction in crystallinity with cycles. However, the appearance of low-intensity diffraction peaks suggested that the structure is stable during intercalation/deintercalation of Li^+ ions. Also, no additional phase peak was found in XRD, indicating that Li^+ ion intercalation in VO_2 (B) is the dominant reaction for energy storage even at low potential 0.05 V. Ren et al. synthesized vertically grown forest of VO_2 (B) nanobelts on VOG substrate and used it as electrode material for LIBs.^[66] Since, in graphene or graphite, Li^+ ion storage occurred below 1 V, therefore, the authors investigated the Li^+ ion storage behavior in 1.5–3.5 V versus Li. The charge-discharge profile of VO_2 (B) nanobelt based forest displayed a plateau around 2.5 V which corresponds to the $\text{Li}_{0.5}\text{VO}_2$ phase.^[93] The discharge capacity was estimated at 475 mAh g^{-1} at 0.1 A g^{-1} current density. However, the cell retained 79% of specific capacity up to 2000 cycles when charge-discharged continuously at 2 A g^{-1} .

Niu et al. synthesized VO_2 with different morphology hollow microspheres, six-armed microspindles, and random NWs by ion-modulating approach and systematically studied their performance for LIBs.^[94] The hollow microspheres exhibited 163 mAh g^{-1} of initial specific capacity at 1 A g^{-1} which

was higher than both six-armed microspindles (142 mAh g^{-1}) and random NWs (118 mAh g^{-1}). The 3D hollow microspheres retained 73% of its initial capacity whereas, six-armed microspindles and random NWs retained only 60 and 45% of initial capacity after 1000 cycles (Figure 13e). Additionally, hollow microspheres retained 80% of initial capacity when charged-discharged at 2 A g^{-1} indicate superior rate capacity and cyclability. The performance of 3D VO_2 hollow microspheres was attributed to high specific surface area and its sustainability the expansion and shrinkage during lithiation/delithiation thereby preventing the self-aggregation of NWs (Figure 13f).

In most of the reports, VO_2 (B) nanostructures were explored as electrode material for LIBs. However, there also exist few reports on other polymorphs of VO_2 . For example, in early 2015, Won et al. reported the rutile phase of VO_2 -carbon microspheres and used this composite as anode in LIBs.^[71] VO_2 (R)-carbon (12.5 wt%) displayed a maximum of 1091 mAh g^{-1} discharge capacity, which is one of the best reported to date. The retention in discharge capacity of the composite was 96% after 100 cycles, calculated from 2nd cycle. Authors attributed this high performance to low pulverization originated from the high structural stability of VO_2 (R)-carbon composite microspheres in the charge-discharge process which involves huge volume changes. Later, Park et al. demonstrated heteroepitaxial grown rutile VO_2

with exposed (002) facets displayed improved performance with lower pulverization.^[72] The as prepared electrode (rutile VO₂ nanobranches grown on rutile Sb:SnO₂) displayed high reversible capacity (350 mAh g⁻¹ at 100 mA g⁻¹) and excellent rate capability (196 mAh g⁻¹ at 2000 mA g⁻¹) with great structural sustainability. The exceptional rate capability was ascribed to the efficient electron and Li⁺ ion migration from heterostructure. The growth of VO₂ nanobranches occurred along (001) direction on rutile Sb:SnO₂ backbone which provides fast Li⁺ ion conduction channels due to the faster diffusion ability through *c* channels. Moreover, the highly conductive nature of Sb:SnO₂ nanobelts (resistivity $1.66 \times 10^{-2} \Omega$) also assisted in electron transport. The prepared electrode material also displayed outstanding cyclic stability delivering 86% of specific capacity up to 80 cycles. It would be worth mentioning here that there is continuous progress being made in improving the performance of VO₂ as a cathode by employing different morphology or composite with carbon-based materials. The specific capacity and rate capability were improved greatly, but the question remains the same for capacity degradation with cycle. Also, it was found that the potential window played a crucial role to achieve better cyclic stability as charge-discharge at low potential leads to the dissolution of vanadium. Improvement in cyclic stability required a deep understanding of reaction mechanisms such as side product formation by in situ analytical tools and thus demands further investigations.

A comprehensive theoretical study presented by Li et al. on Li-ion intercalation into VO₂ (B) using first principle analysis provides significant information about the kinetics of Li-ion diffusion and redox mechanism.^[10] Thermodynamically, one Li per formula can be inserted in VO₂ (B) but its charge storage

capacity can be due to the kinetic factors. Li diffusion in the bulk of VO₂ depends on the concentration of Li such as *b*-axis tunnel where diffusion of Li is facile at low Li concentration and gets blocked by Li diffusion at a higher concentration as observed by energy barrier calculations. However, at higher Li content, the diffusion of Li can be facile at *c*-axis which can alleviate a load of excess Li near surface. This suggests that exposure to desirable crystal facets can also play a crucial role in performance improvement. For the capacity decay with cycles, authors proposed that dissolution of vanadium through disproportionation ($2V^{4+} \rightarrow V^{3+} + V^{5+}$) reaction can be a possible reason like spinel LiMnO₄ where disproportionation of Mn ($2Mn^{3+} \rightarrow Mn^{4+} + Mn^{2+}$) causes surface corrosion and its dissolution.^[95]

VO₂ (B) was also employed as flexible electrodes for application in wearable electronics. To fabricate flexible LIB, Li et al. grown VO₂ (B) nanobelts on carbon cloth and used it as a flexible cathode.^[74] The electrode displayed 145 mAh g⁻¹ initial capacity which reduces to 138 mAh g⁻¹ in 100 cycles, suggesting the outstanding cyclic stability of the electrode. Additionally, the electrode also showed excellent rate capability as discharge capacity was estimated at around 91 mAh g⁻¹ at 2000 mA g⁻¹ current. These results suggest faster kinetics for Li⁺ ion insertion/extraction on the binder-free electrode due to lower charge transfer resistance estimated by EIS. Chao et al. grew GQDs coated VO₂ nanoarrays on graphene foam which was examined as cathode for LIBs.^[4a] Authors carried out CV in voltage range 3.5 to 1.5 V versus Li/Li⁺ for VO₂ nanoarrays grown on graphene foam (presented as GV) whereas GQDs coated VO₂ nanoarrays on graphene foam (presented as GVG). The CV of GV electrode displayed two redox peaks around 2.4 and 2.73 V along with several small peaks (Figure 14a)

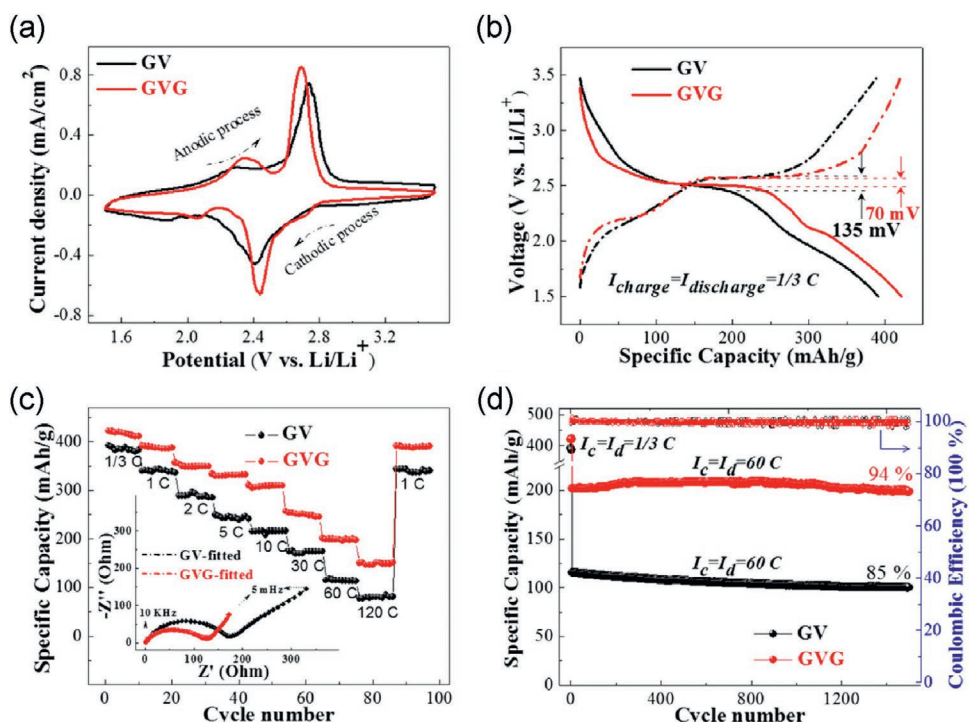


Figure 14. a) CV, b) charge-discharge profile, and c) rate capabilities at 1/3 C for GV and GVG electrodes. Inset of C shows Nyquist plot for both electrodes. d) The cyclic behavior at 60 C for 1500 cycles for both electrodes. Reproduced with permission.^[4a] Copyright 2014, The American Chemical Society.

suggesting multistep Li^+ ion insertion which can be described using Equation 3.



The CV of the GVG electrode showed a positive cathodic peak at 2.44 V versus Li and a negative anodic peak at 2.69 V versus Li. The difference in peak positions for both electrodes was credited to the enhancement in surface electrochemical activity and reduced polarization of the GVG electrode. Authors also calculated the overpotential at half reversible capacity which was found to be 70 mV for GVG electrode while 135 mV for GV supporting the claim (Figure 14b). EIS studied also suggested lower charge transfer resistance for GVG (120Ω) than GV (190Ω). Therefore, GVG electrode showed a higher specific capacity (421 mAh g^{-1}) than GC (391 mAh g^{-1}) at $1/3 \text{ C}$ rate. Also, it delivered 151 mAh g^{-1} of specific capacity at a higher rate of 120 C , suggesting the exceptional rate capability of material (Figure 14c). Moreover, GVG electrode exhibited 94% specific capacity retention to its original value up to 1500 cycles at 60 C rate which can be attributed to the enhanced conductivity and shielding effect of GQDs impeding VO_2 dissolution (Figure 14d). Chen et al. prepared N-doped carbon coated VO_2 nanoarrays on carbon cloth and use it for LIBs as a binder-free cathode material.^[75] The binder-free and N-doped carbon coated electrode displayed 295 mAh g^{-1} of specific capacity at 1C rate for Li^+ ion storage greater than the pure VO_2 arrays (254 mAh g^{-1}). Authors observed lower solution resistance and charge transfer resistance for N-doped carbon coated VO_2 nanoarrays in comparison to VO_2 nanoarrays by EIS method. The reduction in resistance certainly helped to improve the rate capability and cyclic stability. At a 20 C rate, the N-doped carbon coated VO_2 nanoarrays displayed 180 mAh g^{-1} specific capacity higher than pure VO_2 nanoarrays (126 mAh g^{-1}). Also, the composite electrode showed higher retention in specific capacity (95.3%) than VO_2 nanoarrays (91.5%) at 1 C rate for 500 cycles. Authors claimed that improved performance is due to the synergistic effect between array architecture and N-doped carbon shell which improved the reaction kinetics and provide more structural stability. Ex situ SEM analysis was performed to investigate the changes in the morphology of the electrode after 500 cycles. The observed SEM suggested no significant change in morphology of electrode which supports the authors claim about structural stability. Though flexible electrodes have been fabricated and their performance was studied but efforts have not been given to study the performance electrode in bending condition.

4.2. Na-Ion Battery Application

In recent times, the research in Na-ion battery surged mainly due to the exponential increase in the price of Li source and similar chemical properties. Lately, VO_2 has also been explored for Na-ion battery as an electrode material for the development of battery beyond LIBs. Wang et al. synthesized single-crystalline 2D nanosheets and investigated their electrochemical activity as cathode material for SIBs.^[64] Authors carried out a theoretical study to understand the Na^+ ion insertion in VO_2

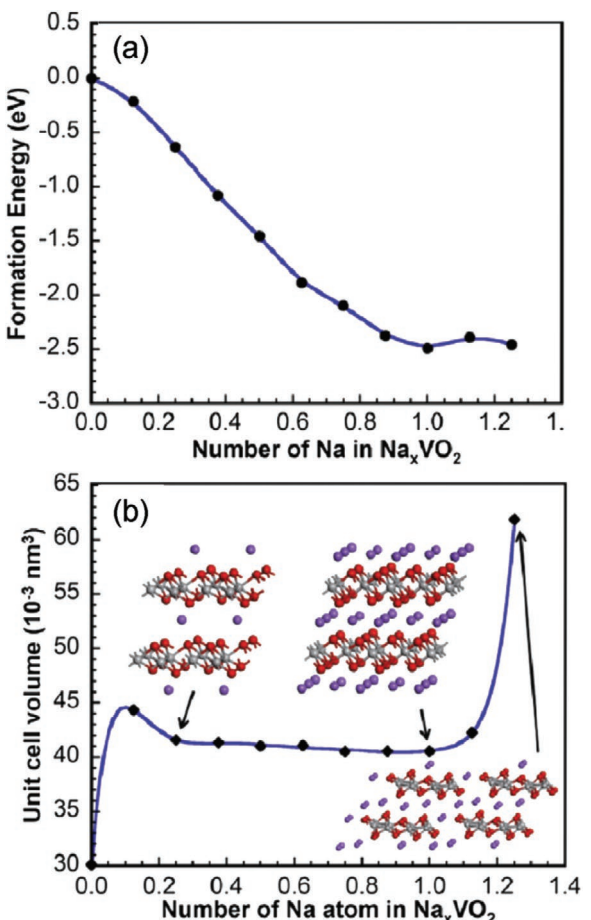


Figure 15. a) The relationship between the formation energy and the number of Na in Na_xVO_2 . The blue curve is the fitting line for the calculated results. b) Unit cell volume with number of Na^+ ions inserted in a VO_2 molecule. The insets explain the relaxed atomic structures with 0.25 Na, 1 Na, and 1.25 Na, respectively, per VO_2 molecule. Na, O, and V atoms are presented by purple, red, and gray spheres, respectively. Reproduced with permission.^[64] Copyright 2014, Elsevier.

nanostructures. The formation energy of discharge product was more negative as the number of Na^+ ion insertion increased from 0 to 1; however, further increase in the number of Na^+ ions, the formation energy became more positive suggested that NaVO_2 as discharge product is more stable than $\text{Na}_{1.125}\text{VO}_2$ (Figure 15a). Also, the authors calculated the change in volume of unit cell with Na^+ ion insertion (Figure 15b). No significant change in volume was observed when inserted Na^+ ions fall in the range of 0.25 to 1, strongly supporting the formation energy calculation data. After calculations, the authors carried out an electrochemical test to evaluate specific capacity. The fabricated cell displayed 214 mAh g^{-1} of specific capacity at 50 mA g^{-1} of current density during first discharge which was not change much for the next two consecutive cycles owing to the large surface area of prepared nanosheets. The cyclic stability of the electrode was examined by charging and discharging at different current densities ranging from 10 to 500 mA g^{-1} up to 50 cycles. A decrease in specific capacity was observed when charged and discharged continuously, however, the capacity loss was much faster when cyclic stability was carried out at

10 mA g⁻¹ of current density. This behavior was explained by the fact that at low current extraction of Na⁺ ion would be difficult for consequent charge process due to complete reduction of the electrode.

He et al. investigated g-VO₂ nanorods for SIBs in 3–0.25 V versus Na potential window at 60 mA g⁻¹ current.^[60] In 1st cycle, the cell displayed 370 mAh g⁻¹ of discharge capacity whereas, in the 2nd cycle it dropped to 220 mAh g⁻¹. Also, the cell showed 70% retention in specific capacity after 100 cycles. Authors carried out ex situ XRD analysis to investigate the discharge mechanism whether it proceeded through intercalation or conversion. XRD analyses suggested that Na⁺ ion intercalation takes place at higher potential (>0.5 V) however, at low potential conversion reaction occurs. Authors also performed TEM analysis of electrodes after discharging up to 0.5 V which showed lattice fringes having d-spacing 0.63 and 0.362 nm that is related to the expansion of (001) and (110) planes after Na⁺ ions intercalation. TEM also suggests that after 10 cycles the crystal structure of VO₂ was damaged but still some lattice fringes can be seen. Also, TEM results suggest the defects in the crystal structure that validated the amorphization of electrodes for discharge below 0.5 V versus Na. Chao et al. prepared 3D nanostructures GQDs coated VO₂ nanoarrays on graphene foam (GVG) and used it as a binder-free electrode for SIBs.^[4a] The electrode displayed 306 mAh g⁻¹ of specific capacity at 1/3 C rate in 3.5–1.5 V versus Na. The discharge curve did not show any plateau, instead a quasi-linear discharge profile was obtained where the slope was divided into two stages for different Na⁺ ion intercalation processes (Equation 4).



The designed GVG electrode also displayed 93 mAh g⁻¹ of specific capacity at 120 C rate which was claimed to be better than other vanadium oxides. The SIB showed 91% retention after 500 cycles at a 5 C charge-discharge rate. This behavior was attributed to the unique design, absence of nonconductive binder, and reduced charge transfer resistance. Yan et al. prepared crumpled rGO coated VO₂ microspheres as electrode material and investigated its activity as anode for SIBs.^[76] The Na⁺ ion storage behavior was tested in a voltage range of 3–0.01 V versus Na. The fabricated cell exhibited 383 mAh g⁻¹ of specific capacity at 0.1 A g⁻¹ current density which reduced to 214 mAh g⁻¹ when the current density was increased 40 times (4 A g⁻¹). The cell also showed stable cyclic stability up to 2000 cycles with only 0.013% loss in specific capacity per cycle. This outstanding behavior was attributed to the improved electronic conductivity, structural stability, and enhanced wettability of the electrode. Wu et al. synthesized a novel composite of VO₂ with MXene and examined its electrochemical activity as anode for SIBs.^[78] At first cycle, the cell exhibited 229.2 mAh g⁻¹ of specific capacity which reduced to 193.8 mAh g⁻¹ at 0.1 A g⁻¹ current density. This decay in specific capacity is because of the solid electrolyte interphase (SEI) formation which leads to irreversible capacity and incomplete deintercalation of Na⁺ ions. The prepared hybrid composite displayed exceptional cyclic stability with a specific capacity of 280.9 mAh g⁻¹ after 200 cycles, which is higher than initial capacities (either compare to 1st cycle or 2nd cycle). Also, it showed higher cyclability than MXene and

VO₂ only. The specific capacity was 323 mAh g⁻¹ at 50 mA g⁻¹ which decreased to only 206 mAh g⁻¹ at 1600 mA g⁻¹ revealed good rate capability as well. This exceptional performance was attributed to low charge resistance, prevention in the aggregation of VO₂ due to MXene, and high surface area due to the flower-like structure. Authors also carried out ex situ XRD and TEM analyses of electrode after the 10th discharge cycle to study the phase changes in electrodes during cycling. VO₂ converted to amorphous phase during Na⁺ ion intercalation up to 0.01 V in VO₂/MXene composite. A similar observation was also noticed by Mahadi et al. when they studied VO₂ (B) and rGO/VO₂ (B) composite for Li⁺ and Na⁺ ion battery.^[96] Authors carried out ex situ XRD and SEM analysis after the 50th charge-discharge cycle to study the changes in phase and structural stability of the electrode. Due to the repetitive intercalation-deintercalation of metal ions, crystalline VO₂ (B) electrode converts to amorphous phase thereby causing capacity degradation during cycling. It was also observed that the original spherical morphology of VO₂ (B) was not found exclusively in cycled electrode. On contrary, when it was combined with rGO, XRD showed the presence of main diffraction peaks of VO₂ in the electrode. Also, no significant change in morphology was observed, thereby suggesting that due to the presence of rGO, VO₂ (B) can sustain volume changes during charge-discharge process.

4.3. Multivalent Ion Battery Application

In recent years, multivalent ions such as Zn²⁺, Mg²⁺, Ca²⁺, and Al³⁺, etc. have gained much attention owing to cost, dendrite-free nature, and safety than LIBs and SIBs.^[97] VO₂ has also been employed as electrode material in multivalent ion based batteries owing to suitable voltage plateau and high capacity. In early 2017, Pei et al. designed an Mg-Li-ion hybrid battery using VO₂ nanoflakes as electrode material.^[98] The hybrid battery was fabricated using dendrite free Mg anode, Mg-Li dual salt electrolyte, and VO₂ nanoflakes as cathode. The cell containing Mg-Li based dual electrolyte (phenyl based) showed distinctive redox peaks in CV whereas, with only Mg based electrolyte, no redox activity was observed which suggested that for proper redox activity Li⁺ ions are required. The hybrid electrolyte-based cell was tested in two potential windows to understand its effect on cyclic stability. In potential range 2–0.01 V, cells showed 291.9 mAh g⁻¹ of specific capacity which reduced to 41.8 mAh g⁻¹ after 100 cycles. This behavior was attributed to the excessive insertion of Li⁺ ion in VO₂ causes structural change. On the other hand, when authors carried out cell investigation in 2–0.5 V, cells showed a lower initial discharge capacity of 206.8 mAh g⁻¹ but it reduced to 154.9 mAh g⁻¹ after 100 cycles, suggesting that this potential window is a perfect working window for the cell. Also, the calculated energy density for this hybrid Mg-Li cell was 427 Wh kg⁻¹ based on the mass of cathode material. This study demonstrates that the selection of a proper potential window is extremely important to achieve maximum performance from VO₂. Later Luo et al. studied Mg ion battery using VO₂ (B) nanorods (1D) and nanosheets (2D) in Mg²⁺ based electrolytes.^[99] VO₂ (B) nanorods exhibited better performance than nanosheets morphology. VO₂ (B) nanorods

showed 341 mAh g⁻¹ of specific capacity which reduced to 142.9 mAh g⁻¹ after 60 cycles. The improved performance of VO₂ (B) nanorods was attributed to the reduction in the diffusion path and improved diffusion rate of Mg ions. Here, the authors used Mg²⁺ based electrolytes without any addition of Li⁺ ions-based salt. Though authors achieved much better specific capacity, but rate capability and cyclic stability are poor which might be due to the low ionic conductivity of Mg²⁺ ions caused by its polarizing character. Future studies should be focused on the investigation of Mg²⁺ based electrolyte with good ionic conductivity for Mg²⁺ ion batteries. Recently, Cen et al. used VO₂ (B) ultrathin nanosheets as cathode for hybrid Mg-Li-ion batteries with phenyl-based electrolyte to improve the kinetics of intercalation/deintercalation process.^[100] The cell configuration and electrolytes were the same as explained above and reported by Pei et al. Here authors achieved 275 mAh g⁻¹ of reversible discharge capacity in 2.4–1.2 V versus Mg potential window, decent rate capability, good cyclic stability up to 500 cycles, and high energy density of 484 Wh kg⁻¹. Hybrid electrolyte improves the performance of battery but demonstrated batteries still lacks with rate capability and cyclic stability. Also, using two metal cations in the electrolyte can make the electrochemical process complex such as type of metal cation intercalated, chemical composition of SEI formed on Mg surface, etc., therefore, research should be focused on understanding the charge storage mechanism.

Applications of VO₂ (B) can also be seen in Zn-ion batteries (ZIBs).^[101] Ding et al. employed VO₂ (B) as cathode material in ZIBs.^[101a] Taking the advantage of tunnel structure which can easily accommodate Zn²⁺ ion and thus improves the capacity and rate capability. The Zn ion cell delivered 357 mAh g⁻¹ of specific capacity at 0.5 C which decreased to only 171 mAh g⁻¹ at 300 C. The device exhibited 297 Wh kg⁻¹ of specific energy at 180 W kg⁻¹ of specific power. Authors confirmed the intercalation of Zn²⁺ and formation of Zn_xVO₂ by XPS analysis of discharge electrode. This kind of intercalation pseudocapacitance behavior of VO₂ (B) can be utilized to achieve ultrafast kinetics and high-performance batteries. Wei et al. fabricated an aqueous ZIB using metastable VO₂ cathode to study the charge storage mechanism.^[102] The cell with Zn foil anode and VO₂ cathode (2 mg mass loading) in aqueous 3M Zn(CF₃SO₃)₂ showed 274 mAh g⁻¹ of specific capacity, 271.8 Wh kg⁻¹ of specific energy, and exceptional cyclic stability up to 10 000 cycles (79% capacity retention). Authors carried out XRD and Raman analyses to understand the structural changes in VO₂ during intercalation and deintercalation. During electrochemical processes, the increase in interlayer spacing was observed, suggesting phase transition and formation of V₂O₅·nH₂O (from XRD). Also, the crystal structure changed from monoclinic to bilayer lamellar structure providing great flexibility in crystal structure which can self-adjust the Zn²⁺ ion diffusion to sustain the volume changes during charge-discharge process. Later Li et al. also studied the electrochemical charge storage mechanism of Zn/VO₂ battery using operando XRD, XPS, and neutron activation analysis.^[101c] In ZnSO₄ aqueous electrolyte the cell delivered 272 mAh g⁻¹ of specific capacity at 3 A g⁻¹ current rate and retained 75.5% initial discharge capacity after 945 cycles. By operando techniques, the authors observed that there is proton insertion complemented by Zn²⁺ ion storage

caused by reversible deposition of Zn₄(OH)₆SO₄·5H₂O on to the surface of VO₂. They also proposed that the insertion of ions whether proton or Zn²⁺ ions into VO₂ cathode would be decided by the solvation energies of salt anion and the energetics of proton insertion. Between these two processes, proton insertion would cause minimal structural distortion and hence, displayed good cyclic stability. In this cell, the discharge/charge process involved both capacitive and ionic diffusion thus cathode displayed fast kinetics and high capacity. During discharge of cell, the first proton gets inserted and as discharge process goes on, Zn²⁺ ions diffusion process started due to the formation of Zn₄(OH)₆SO₄·5H₂O on VO₂, which prevented further insertion of protons. Chen et al. also studied aqueous Zn/VO₂ battery using VO₂ nanorods as cathode in 1M ZnSO₄ electrolyte which displayed 325.6 mAh g⁻¹ of specific capacity at 50 mA g⁻¹, good rate capability, and cyclic stability up to 5k cycles at 3 A g⁻¹.^[101b] The operando techniques suggested that expansion and shrinkage of VO₂ with Zn²⁺ insertion/extraction is reversible as authors did not observe any significant changes in the unit cells suggesting VO₂ can be a potential cathode material for ZIBs.

To avoid binders and improve conductivity and porosity, Dai et al. prepared free-standing graphene/VO₂ composite film which they used to demonstrate an excellent cathode for Zn ion battery.^[103] The cell displayed 276 mAh g⁻¹ of specific capacity at 0.1 A g⁻¹ of current rate which decreased to 120 mAh g⁻¹ at exceptionally high 35 A g⁻¹ current. The fabricated Zn/VO₂ battery showed outstanding cyclic stability (99% retention in 1000 cycles) and a maximum of 65 Wh kg⁻¹ of specific energy at 7.8 kW kg⁻¹ of specific power. The exceptional behavior was attributed to the synergistic effects from the robust structure of VO₂ and the highly porous nature of graphene which can sustain high volume changes during insertion/extraction of Zn²⁺ ion in the electrode. Authors have also demonstrated flexible soft-packaged Zn/VO₂ batteries. Not only VO₂ (B) was demonstrated for ZIBs, recently Zhang et al. demonstrated VO₂ (M) can be a suitable choice cathode for ZIB.^[104] A binder-free cathode was prepared using VO₂ (M) and CNTs which showed 248 mAh g⁻¹ of specific capacity at 2 A g⁻¹ of current, good rate capability, and superior cyclic stability up to 5000 cycles (84.5% retention in specific capacity at 20 A g⁻¹ of current). Authors also studied the energy storage mechanism which was as same as explained by Li et al.^[101c] However, herein authors showed that VO₂ (M) phase can also be a potential cathode for ZIBs. Li et al. investigated the impact of oxygen vacancy in VO₂ (B) crystal structure on the ZIB performance.^[105] DFT calculations suggested that oxygen vacancies in VO₂ (B) crystal can result in a narrow bandgap and reduce the Zn²⁺ ion diffusion barrier than pristine VO₂ (B). The oxygen vacancy rich VO₂ (B) delivered 375 mAh g⁻¹ of specific capacity at 100 mA g⁻¹ of current and 85% retention in specific capacity up to 2000 cycles which were better than VO₂ (B) nanobelts which was attributed to the oxygen vacancy that create big tunnel structure along *b* axis and hence improved the reaction kinetics and energy storage performance of ZIB.

Though rechargeable aqueous ZIBs have been demonstrated using VO₂ as cathode, but reported ZIBs have issues related to the formation of side product and cyclic stability which is mainly hampered by the deposition of side product on both

cathode as well as anode thus impeding the diffusion of ions. Yang et al. systematically studied the degradation mechanism of the Zn/VO₂ battery along with other cathodes.^[106] Zinc hydroxy sulfate (a basic zinc salt) was detected (by ex situ XRD) in most cases as a byproduct which was formed due to the chemisorption of zinc hydrated ions followed by its precipitation as a zinc hydroxy sulfate on the surface of electrodes. The side product formation is attributed to the dissociation of a water molecule ($\text{H}_2\text{O} \leftrightarrow \text{H}^+ + \text{OH}^-$) and formed OH⁻ ion reacted with electrolyte to form zinc hydroxy sulfate. Researchers found that the formation of this basic zinc salt strongly depends on applied current during electrochemical processes. Using a small current, the formation of basic zinc salt dominated the surface of the electrode which hinders the transport of ions thereby leading to rapid degradation in capacity. On the increase of current by hundred times, the growth of basic zinc salt was not dominant which helped to improve the cyclic stability. Also, the authors observed vanadium dissolution in addition to basic zinc formation which appeared to be a vital issue affecting the cycling behavior. In another study published by Pang et al. on aqueous Zn/VO₂ battery also involved the study of side product by in operando synchrotron diffraction methods and the effect of different anions on the performance.^[107] In 1M ZnSO₄ aqueous electrolyte, the electrode undergoes the reversible formation of solid-state reaction between VO₂ (B) and Zn_{0.44}VO₂ to form (Zn(OH)₂)₃ZnSO₄·5H₂O as a side product. The formation of side product is due to the hydration of Zn²⁺ ions which not only protect the corrosion of electrode materials, but also enable the dehydration process of zinc ions at the interface. This side product is also ionically conductive, thus, it made the mobility of Zn²⁺ ions facile at the interface. Authors also examined the formation of byproducts associated with Zn(CF₃SO₃)₂ and Zn(NO₃)₂ which suggested that byproducts with large ionic paths can be an essential choice for further improvement in electrochemical processes in ZIBs. Other morphologies such as tetragonal VO₂ hollow nanospheres^[108] and composites such as rGO/VO₂ nanobelts composite,^[109] PEDOT/VO₂,^[110] etc. have also been explored to demonstrate the performance of ZIBs using VO₂ as cathode material. Though there have been different studies that showed VO₂ can act as potential cathode material for ZIBs, yet its practical application is far from reality mainly due to the sluggish kinetics which affects the performance in terms of rate capability and cyclic stability. Also, most of the study involves fabrication of ZIB using aqueous electrolyte which suffers from voltage limitations due to the decomposition of water beyond 1.23 V. In the future, studies should be focused on the usage of water in a salt electrolyte that provides the freedom to extend the working potential window as suggested by Wang et al.^[111]

4.4. Other Battery Applications

VO₂ was not only utilized in LIBs and SIBs, but also it has been employed in many different battery applications such as Zn ion, Mg ion, Li-S, and hybrid Na-air. Khan et al. synthesized carambola-shaped VO₂ nanostructure by growing it on porous rGO coated carbon paper (VGC) and explored its activity as an air electrode for a hybrid Na-air battery.^[77] Prior to examining its

activity in hybrid Na-air cells, the authors carried out detailed electrocatalytic activity analysis to observe its activity for oxygen reduction (ORR) and oxygen evolution reaction (OER). VO₂ nanostructures showed activity for ORR and OER both in alkaline solution though it wasn't better than the benchmark catalyst such as Pt/C (for ORR) and RuO₂ (for OER), but it can be a possible alternative due to the lower cost. A hybrid Na-air cell was fabricated using VGC as air electrode which displayed 0.64 V of overall overpotential gap, 81% electrical energy efficiency, good cyclic stability up to 50 cycles, and 100 mW g⁻¹ of specific power. The performance was attributed to the improved electrical conductivity due to the absence of binder and the presence of rGO and efficient diffusion of air and electrolyte owing to the open structure of air electrode.

VO₂ was also employed in Li-S batteries by Song et al. to improve the Coulombic efficiency and cyclic stability.^[112] The cell with VO₂-VN host showed high specific capacity 1105 mAh g⁻¹ at 1C rate which decreased to 935 mAh g⁻¹ when the rate was increased twice. Authors investigated the cyclic stability of the Li-S cell at 2 C rate and observed that capacity decayed 0.06% per cycle after 800 cycles. Also, a fabricated cell can be operated at an elevated temperature of 50 °C. The superior performance of the VO₂-VN/graphene host can be attributed to the immobilization-diffusion-conversion of lithium polysulfides which inhibited the shuttling of polysulfides, boosting the redox kinetics, and hence improving the electrochemical performance of Li-S batteries. We have summarized the performance of VO₂ nanostructures used for EES applications in Table 2.

4.5. Supercapacitor Application

VO₂, a valuable functional material, crystallizes in different polymorphs. The main concern with metal oxide for its application is resistivity/conductivity. VO₂ shows better performance and cyclic stability than V₂O₅ because of higher electronic conductivity and better structural stability when cycling. Therefore, it was also employed as an electrode material in supercapacitor. Depending on the charge storage mechanism, supercapacitors are classified into two categories i) electrical double layer capacitors (EDLCs) and ii) pseudocapacitors. The reversible charge storage in EDLCs occurs physically by adsorption of electrolyte ions at the interface of electrode/electrolyte whereas, in pseudocapacitors, the charges were stored chemically by the redox reaction at the vicinity (within few nanometers) of the surface.^[121] VO₂ has been considered as pseudocapacitive material which means it stores charges near surface. Here, we have summarized the important findings on VO₂ as an electrode for supercapacitor applications.

Alike other transition metal oxides, VO₂ also suffered from higher resistivity. Pan et al. synthesized highly conductive VO₂ was synthesized by H₂ treatment and investigated its effect on charge storage properties of a supercapacitor.^[122] The commercial VO₂ powder was annealed at 500 °C in presence of continuous H₂ flow at 50 Torr. It was found that H₂ treatment lowered the crystal quality of the VO₂, which enhances the surface driven pseudocapacitance property. H₂ treated VO₂ showed threefold lesser resistivity as compared to nontreated

Table 2. Summary of VO₂ nanostructures utilized in numerous energy storage devices.

| Material | Morphology | Cell type | Capacity [mAh g ⁻¹] | Cycle | Capacity retention [%] or final capacity (mAh g ⁻¹) | Ref |
|--|-------------------------------|--------------------|---------------------------------|-------|---|-------|
| Paramontroseite VO ₂ | Walnut like nanoarchitectures | Li ion/2E | 61.9 | 50 | 74.3% | [23a] |
| VO ₂ (B) | Flowerlike | Li ion/2E | 74.9 | 50 | 41.5% | [21c] |
| VO ₂ (B) | Belt-like | Li ion/2E | 62.1 | 50 | 46% | [21c] |
| VO ₂ (B) | Carambola | Li ion/2E | 58.3 | 50 | 38% | [21c] |
| Post-treated VO ₂ (B) | flowerlike | Li ion/2E | 81.3 | 50 | 67% | [21c] |
| Paramontroseite VO ₂ | Hollow nanourchins | Li ion/2E | 72.1 | 50 | 39.1% | [23b] |
| Paramontroseite VO ₂ | Nanorods | Li ion/2E | 43.5 | 50 | 30.3% | [23b] |
| MWCNT/VO ₂ (B) | Bundles | Li ion | 177 | 100 | 92% | [65] |
| C/VO ₂ (B) | microspheres | LIBs | 160.8 | 50 | 51% | [69] |
| VO ₂ (B) | Nanobelts | LIBs | 201.3 | 50 | 54% | [62] |
| VO ₂ (B) | Fibrous | LIBs | 334 | 20 | 80% | [63] |
| VO ₂ (B)/graphene | Nanotubes | LIBs | 450 | 20 | 71% | [59] |
| VO ₂ (B) | Bundles of nanorods | LIBs | 171 | 47 | 63% | [113] |
| VO ₂ (B)@C | Nanobelts | LIBs | 161 | 50 | 80% | [61] |
| N-doped graphene VO ₂ (B) | Flower | LIBs | 418 | 50 | 60% | [92] |
| VO ₂ -graphene | Ribbons | LIBs | 204 | 1000 | 90% | [4c] |
| C-Vox | Nanobelts | LIBs | 232 | 50 | 84% | [114] |
| VO ₂ (R)-C | Microspheres | LIBs | 1091 | 100 | 637 mAh g ⁻¹ | [71] |
| VO ₂ on Sb:SnO ₂ | Nanobelts | LIBs | 350 | 80 | 86% | [72] |
| VO ₂ (B) on carbon cloth | Nanobelt | LIBs | 130 | 200 | 90% | [74] |
| GQDs coated VO ₂ nanoarrays on graphene foam | 3D | LIBs | 421 at 0.1 A g ⁻¹ | 1500 | 94% at 18 A g ⁻¹ | [4a] |
| GQDs coated VO ₂ nanoarrays on graphene foam | 3D | SIBs | 306 at 0.1 A g ⁻¹ | 1500 | 88% at 18 A g ⁻¹ | [4a] |
| VO ₂ (B)/rGO | 3D | LIBs | 253s | 50 | 195 mAh g ⁻¹ | [96] |
| VO ₂ (B)/rGO | 3D | SIBs | 195 | 50 | 112 mAh g ⁻¹ | [96] |
| VO ₂ /CNT | | LIBs | 537.6 at 0.05 A g ⁻¹ | 100 | 536.5 mAh g ⁻¹ at 0.1 A g ⁻¹ | [115] |
| Hydrogen molybdenum bronze/VO ₂ nanoflakes on graphene foam | Core/shell | LIBs | 219 | 500 | 209 mAh g ⁻¹ | [12] |
| VO ₂ (B) | Raft-like nanobelts | LIBs | 160.3 | 100 | 89.5 mAh g ⁻¹ | [116] |
| N-doped carbon coated VO ₂ | Arrays | LIBs | 295 | 500 | 281 mAh g ⁻¹ | [75] |
| rGO/VO ₂ (B) | Nanorods | LIBs | 692 | 400 | 400 mAh g ⁻¹ | [60] |
| VO ₂ | Hollow microspheres | LIBs | 163 | 1000 | 119 mAh g ⁻¹ | [94] |
| VO ₂ | Six-armed microspindles | LIBs | 142 | 1000 | 85 mAh g ⁻¹ | [94] |
| VO ₂ | Random nanowires | LIBs | 118 | 1000 | 53 mAh g ⁻¹ | [94] |
| rGO/VO ₂ (B) | Nanorods | SIBs | 220 | 100 | 154 mAh g ⁻¹ | [60] |
| VO ₂ | Nanosheets | SIBs | ≈250 at 20 mA g ⁻¹ | 50 | 179 mAh g ⁻¹ | [64] |
| rGO/VO ₂ | Microspheres | SIBs | 214 | 2000 | 156 mAh g ⁻¹ | [76] |
| VO ₂ (A)/graphene | Nanostructure | SIBs | 115 | 100 | 115 mAh g ⁻¹ | [117] |
| VO ₂ /Mxene | 3D flower | SIBs | 229.2 | 200 | 280.9 mAh g ⁻¹ | [78] |
| VO ₂ /MoS ₂ | Nanorods | LIBs | 979.4 | 100 | 694.5 mAh g ⁻¹ | [118] |
| VO ₂ | Nanoflakes | Hybrid (Li-Mg ion) | 206.8 | 100 | 154.9 mAh g ⁻¹ | [98] |
| VO ₂ (B) | Nanosheets | Hybrid (Li-Mg ion) | 145 | 500 | 94.3 mAh g ⁻¹ | [100] |
| VO ₂ (B) | Nanosheets | Mg ion | 333 | 60 | 15 mAh g ⁻¹ | [99] |
| VO ₂ (B) | Nanorods | Mg ion | 341 | 60 | 143 mAh g ⁻¹ | [99] |
| VO ₂ -VN | | Li-S | 935 | 800 | | [112] |
| SnO ₂ @C@VO ₂ | Hollow nanospheres | LIB | 1305.6 | 100 | 765.1 mAh g ⁻¹ | [119] |
| Tetragonal VO ₂ | Hollow nanospheres | Zn ion | 440 at 0.1 A g ⁻¹ | 860 | 143 mAh g ⁻¹ at 1 A g ⁻¹ | [108] |
| rGO/VO ₂ (B) | Nanobelts | Zn ion | 456 at 0.1 A g ⁻¹ | 1600 | 216 mAh g ⁻¹ at 5 A g ⁻¹ | [109] |
| PEDOT/VO ₂ | Nanobelts | Zn ion | 540 at 0.05 A g ⁻¹ | 1000 | 280.7 mAh g ⁻¹ at 5 A g ⁻¹ | [110] |
| rGO/VO ₂ (M) | Nanoparticles | LIB | 311 | 200 | 283 mAh g ⁻¹ at 60 mA g ⁻¹ | [120] |

sample as confirmed by temperature dependence resistance study. The plausible mechanism for superior performance was explained by hydrogen intercalation in VO_2 crystals which leads to the formation of a strong H–O bond without altering the V oxidation state. Due to the formation of H–O bond, O electronegativity was reduced, which weakens V–O bond strength, resulting in the tendency of electron occupation of V d-levels, or a metallic state. In addition, the hydrogen reduction can also cause O-vacancies or slightly adjust V valence states, which significantly increases the conductivity at high temperatures.^[123] The electrochemical study of H_2 treated VO_2 was performed in 1 M Na_2SO_4 aqueous electrolyte. The obtained voltammogram revealed that the observed current density of treated VO_2 was almost fourfold higher than pristine VO_2 . EIS study also suggested a threefold decrease in resistance than pristine VO_2 . Further, the specific capacitance and specific energy of H_2 treated VO_2 was calculated to be $\approx 300 \text{ F g}^{-1}$ and 17 W h kg^{-1} respectively, with cycling efficiency of 96% superior to pristine VO_2 . Authors concluded that the estimated fourfold enhancement in specific capacitance is due to the improvement in electronic conductivity and fast charge transfer. Though authors claimed that high capacitance was achieved by preparing conductive VO_2 yet, the initial loss in capacitance was problematic. Graphene and VO_2 based composites were also studied for supercapacitors applications in order to improve the electronic conductivity, mechanical stability, and also surface area. Wang et al. synthesized 3D graphene- VO_2 nanobelt composite (graphene/ VO_2) hydrogels by hydrothermal method.^[124] The weight percentage of VO_2 (B) in the hydrogel was 59 %. Authors build a symmetric device using prepared 3D graphene/ VO_2 composite which displayed 427 F g^{-1} of specific capacitance at 1 A g^{-1} in 1.2 V potential window in 0.5 M K_2SO_4 electrolyte. The composite exhibited 21.3 W h Kg^{-1} of maximum specific energy, 3000 kW kg^{-1} of maximum specific power, and outstanding cyclic stability (92% retention after 5000 cycles). Also, authors attributed the superior cyclic stability to the synergistic effect between VO_2 and graphene. The presence of graphene reduces the chemical dissolution of VO_2 and provides support to maintain the VO_2 structure. EIS studies were performed to understand the superior electrochemical performance than their individual components. The superior electrochemical activity and stability were attributed to the faster electrolyte ions diffusion and electron transport across the interface of an interconnected porous network of graphene/ VO_2 composite. Another advantage of this work is the utilization of cheap precursors and scalable synthesis methods, which is one of the requirements for practical application. However, the specific energy of VO_2 based devices can be further improved using asymmetric configuration which was not carried out in this work. In another work related to graphene, Lee et al. prepared graphene based VO_2 composite where authors studied the effect of graphene lateral size on the energy storage performance.^[125] Authors synthesized flexible electrodes and found that VO_2 :ultralarge graphene oxide (UGO) weight ratio of 7:3 as optimal concentration for preparing mechanically stable film without any defects. Authors choose two different lateral sizes of GO, ultralarge GO, UGO ($47 \pm 22 \mu\text{m}$) and small-scale GO (SGO) ($0.8 \pm 0.5 \mu\text{m}$) to fabricate a flexible hybrid supercapacitor. Two flexible electrodes had been synthesized using VO_2 in combination with UGO

and SGO which were termed as VURGO and VSRGO. The VURGO hybrid electrode exhibited 769 F g^{-1} of specific capacitance which was higher than the VSRGO electrode (385 F g^{-1}) and ultralarge GO (URGO) (286 F g^{-1}). The EIS and four-point probe technique suggested that VURGO has lesser sheet resistance as compared to VSRGO which strongly suggests that the electrical conductivity is affected by the synergistic effect of VO_2 nanobelts and URGGO combination. The long-term cyclic stability test for VURGO shows capacitance retention of 82% at a current density of 5 A g^{-1} up to 5000 cycles. This investigation clearly demonstrated the importance of the usage of large-size graphene sheets that can significantly improve the performance of electrode materials. Wang et al. fabricated a high potential supercapacitor using VO_2 nanoflowers on 3D graphene networks (VO_2 NF@3DG) as a flexible and binder-free electrode.^[126] The device showed the areal capacitance of 466 mF cm^{-2} and 283.2 mF cm^{-2} in the three- and the two-electrode configurations, respectively in 0.5 M K_2SO_4 aqueous electrolyte. The device also displayed 63.5% retention in capacitance after 3000 cycles, indicating stable cycling performance which could be due to the rapid electron and ion transport owing to the interconnected nature of the electrode. Further, the device showed 279.6 mWh m^{-2} maximum areal energy and $60\,000 \text{ mW m}^{-2}$ high-areal power.

The poor electrocatalytic activity of VO_2 was also utilized to fabricate an aqueous supercapacitor in order to achieve a high voltage device. The use of water-based electrolytes is considered as a green and sustainable electrolyte, but they suffer from a low working potential range. Thus, it is crucial to either use a wide potential window stable electrolyte or to modify the electrode to suppress the water electrolysis process associated with hydrogen evolution and OERs. One seminal study published by Sahoo et al. utilized two different metal oxides having poor activity for water electrolysis to enhance the working potential of the device in aqueous electrolytes.^[127] rGO@ VO_2 nanostructures were utilized as a negative electrode material to suppress the hydrogen evolution process due to its poor catalytic activity. For positive electrode, authors used rGO@ Mn_3O_4 which is a poor catalyst for oxygen evolution. Using these electrodes authors fabricated an aqueous electrolyte-based device which can be operated up to 2.2 V. The fundamental mechanism explained by authors is that oxidation of Mn^{4+} to Mn^{7+} at positive electrode and reduction of V^{3+} to V^{2+} occurs at a specific potential which suppresses the O_2 and H_2 evolution reactions, respectively. The high-voltage water-electrolyte based asymmetric supercapacitor device exhibited a high specific energy of 42.7 Wh kg^{-1} and a maximum power density of $11\,260 \text{ W kg}^{-1}$.

Binder-free electrode always offers an advantage over traditional electrodes prepared by slurry coating methods. Therefore, Hu et al. prepared a binder-free VO_2/TiO_2 nanosponges electrode by electrostatic spray deposition method which is structured as tangled spherical particles and bunches.^[128] The as-prepared nanosponges with varying V percentages were tested for supercapacitors. In general, the VO_2 electrochemical performance decreases owing to the large volumetric change (during the expansion/contraction process) at subsurface level by Faradaic pseudocapacitance. However, anatase TiO_2 (typical zero-strain material), restrains the volumetric change and keeps the framework stable during ion intercalation/deintercalation,

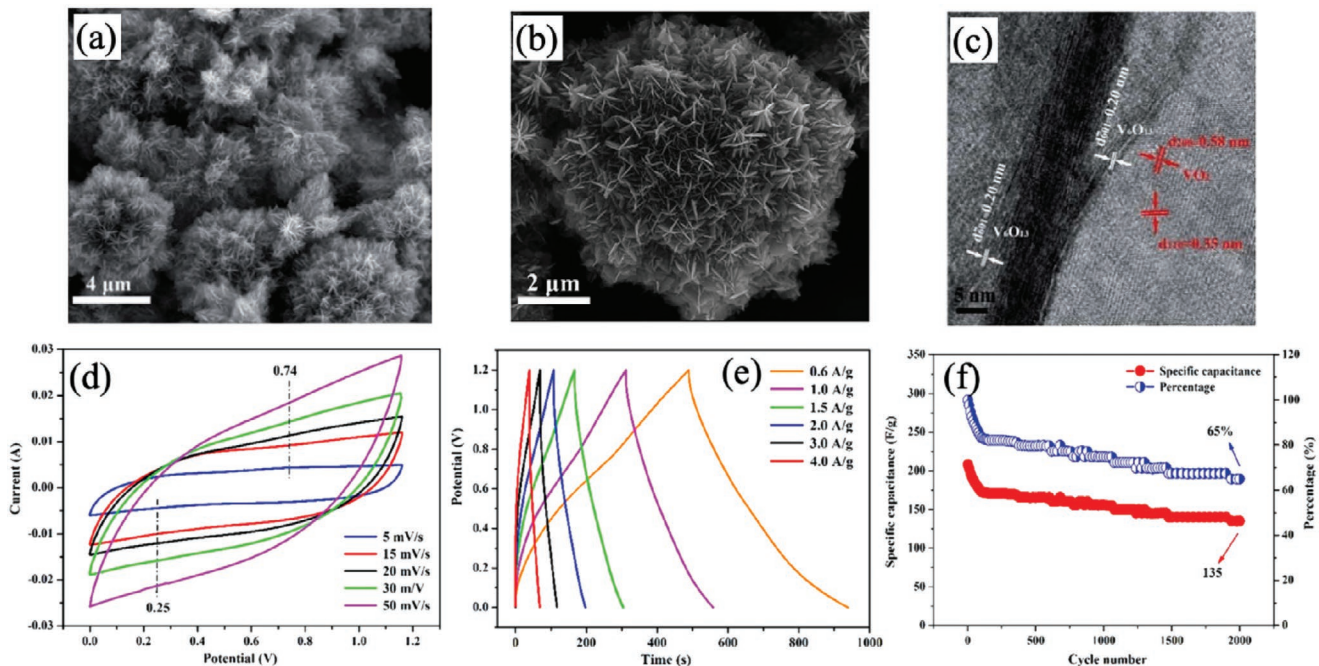


Figure 16. a,b) FE-SEM c) HR-TEM images of VO_2 hierarchical microspheres. Electrochemical performance of hierarchical VO_2 microspheres d) Voltammogram at different sweep rates, e) galvanostatic charge-discharge profiles at different current rates, and f) cycling stability analysis in terms of percentage at a current density of 4.0 A g^{-1} . Reproduced with permission.^[129] Copyright 2015, The Royal Society of Chemistry.

and thus an improvement in cyclic stability was observed. The half-cell performance was tested in an 8M LiCl aqueous solution over the potential range from -0.3 to -1.0 V (vs SCE). The VO_2/TiO_2 electrodes show an electrochemical capacity of $\approx 548 \text{ F g}^{-1}$ (at 10 mV s^{-1}) and 84.3% retention in specific capacitance up to 1000 cycles.

Highly open porous 3D structure is advantageous to bulk material as it offers better electrode-electrolyte contact due to the better accessibility of surface by electrolyte thus can improve the electrochemical kinetics. Li et al. reported the synthesis of 3D hierarchical VO_2 microspheres from hyperbranched nanoribbons for supercapacitor applications (Figure 16a,b).^[129] The synthesized VO_2 microspheres have two crystals forms V_6O_{13} and VO_2 with 86.2 and 13.8 mass% respectively. The growth mechanism was explained with a time-dependent experiment and the role of solvent polarity. The device performance was examined in 1M LiNO_3 aqueous electrolyte in button cell using 3D VO_2 microspheres. The hierarchical microspheres show specific capacitance of 456 F g^{-1} at 0.6 A g^{-1} up to 1.2 V (Figure 16c,d). The estimated maximum energy and power density were 22.8 Wh kg^{-1} and 1.2 kW kg^{-1} at 4 Ag^{-1} respectively. The hierarchical vanadium oxide microspheres show 65% of specific capacitance retention after 2000 cycles at 4 Ag^{-1} (Figure 16f).

Zhang et al. had also reported 3D VO_2 (B) hierarchical spheres for supercapacitor applications. 3D porous solid and hollow VO_2 (B) porous hierarchical spheres were synthesized as per the reported scheme.^[130] The electrochemical performance was analyzed in 1M Na_2SO_4 /carboxymethyl cellulose as an electrolyte. The areal and gravimetric capacitance of hollow VO_2 (B) spheres were found to be 1175 mF cm^{-2} and 336 F g^{-1} , respectively at 2 mA cm^{-2} of the applied current rate. However,

VO_2 (B) solid spheres showed 951 mF cm^{-2} areal and 272 F g^{-1} gravimetric capacitances. The superior performance of hollow VO_2 (B) spheres was explained by the EIS study. The solution resistance (R_s) and charge transfer resistance (R_{ct}) of hollow VO_2 (B) were estimated to be lower than solid spheres which were attributed to the porosity of material, which allowed effective diffusion of electrolyte as well as the faster ion diffusion and transport thereby resulting in the superior conductivity of hollow VO_2 (B) spheres. The symmetric supercapacitor (SSC) devices of 3D VO_2 (B) were examined in the potential window of 0 to 1.4 V. The CV curves displayed quasi-rectangular shapes at a high scan rate (100 mV s^{-1}) suggesting the excellent capacitive behavior of VO_2 (B) spheres. In the two-electrode configuration, the hollow spheres SSC device had shown an energy density of 669 mWh m^{-2} and the corresponding power density of 3.5 W m^{-2} which is higher than the solid spheres SSC device showing energy density of 333 mWh m^{-2} at 3.5 W m^{-2} power density. The observed capacitance retention of hollow and solid VO_2 (B) SSC device were 60 and 36%, respectively after 5000 cycles. A multicomponent electrode including VO_2 , graphene, and NiS_2 was prepared to improve specific energy and better cyclic stability by enhancing the conductivity. Chen et al. synthesized densely packed $\text{VO}_2/\text{graphene}@\text{NiS}_2$ hybrid aerogel having 3D nanostructure which was employed as electrode material in asymmetric supercapacitor device.^[131] The electrochemical study of the $\text{VO}_2/\text{graphene}@\text{NiS}_2$ has been performed with 6M KOH as an electrolyte. The galvanostatic charge-discharge measurements of $\text{VO}_2/\text{Graphene}@\text{NiS}_2$ exhibited specific capacitance up to 1280 F g^{-1} at 1 A g^{-1} current rate and good cyclic stability was also observed up to 5000 cycles (capacitance retention of 63.5%). The superior performance of the $\text{VO}_2/\text{graphene}@\text{NiS}_2$ is explained by EIS measurement which

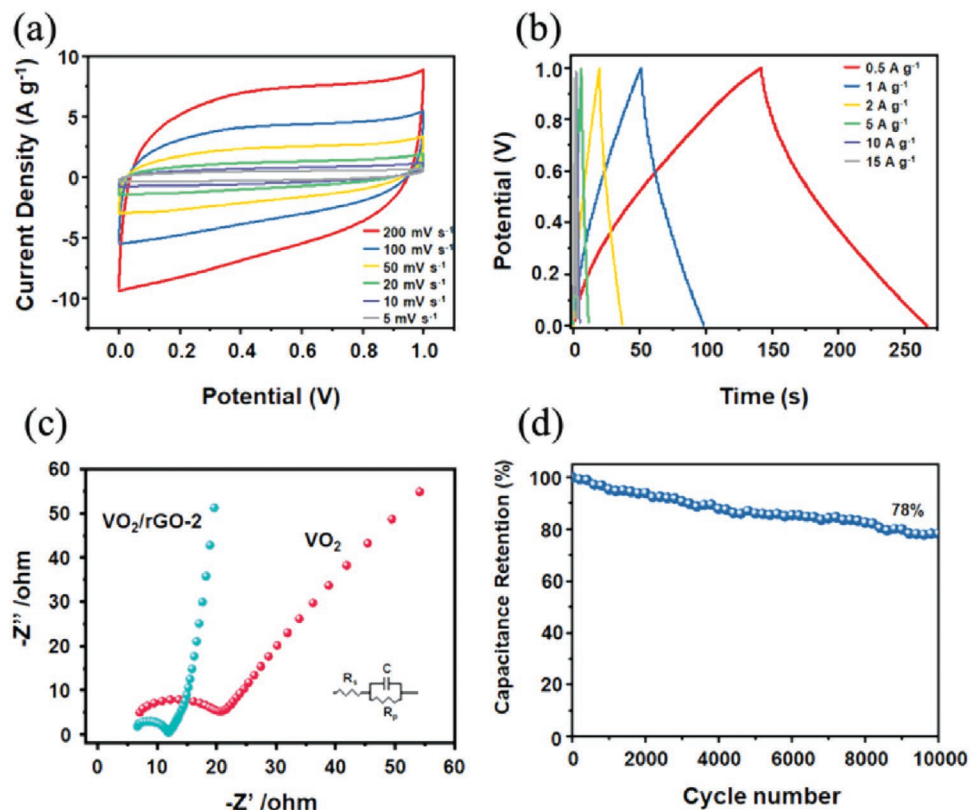


Figure 17. a) CV and b) charge-discharge profiles at different sweep and current rates, respectively. c) EIS spectra of $\text{VO}_2(\text{B})$ nanobelts and $\text{VO}_2/\text{rGO-2}$ and d) cyclic stability plot in terms of capacitance retention up to 10 000 cycles for $\text{VO}_2(\text{B})/\text{rGO-2}$ based all-solid-state supercapacitors. Reproduced with the permission.^[132] Copyright 2019, Nature Publishing Group.

suggested that this composite has a lower solution and charge transfer resistance that leads to faster ionic transport. The asymmetric supercapacitor device was fabricated using $\text{VO}_2/\text{graphene@NiS}_2$ and graphene aerogel as positive and negative electrodes, respectively. The device performance was analyzed in a 1.4 V potential window with KOH/PVA as gel electrolyte. The device showed 60.2 Wh kg^{-1} of energy density at 350 W kg^{-1} power density and retained 86.2% of initial capacitance up to 10 000 cycles. It would be worth mentioning that this solid-state supercapacitor device displayed good performance in terms of the working potential of the device and high specific energy. In another study, Lv et al. had reported free-standing $\text{VO}_2(\text{B})$ nanobelts/rGO composites for flexible all-solid-state supercapacitors.^[132] The rGO sheets and $\text{VO}_2(\text{B})$ nanobelts intertwined to give a porous framework to the synthesized material. The three-electrode electrochemical performance of $\text{VO}_2(\text{B})/\text{rGO}$ was performed with $0.5 \text{ M K}_2\text{SO}_4$ within the potential range of 0 to -1.0 V . The maximum capacitance calculated from the galvanostatic charge-discharge method was 353 F g^{-1} at 1 A g^{-1} $\text{VO}_2(\text{B})/\text{rGO}$ which was higher than the VO_2 and rGO. Further, all symmetric solid-state supercapacitor was fabricated using carbon paper as current collector with PVA/LiCl gel electrolyte. The shape of the CV curves at different scan rates is almost unaltered, demonstrating the excellent charge and discharge characteristics of the device. The device showed a specific capacitance of 29.6 F g^{-1} at 1 A g^{-1} and maximum power density of 7152 W kg^{-1} at the energy density of 3.13 Wh kg^{-1} . After

10 000 charge/discharge cycles, the device retained 78% of initial capacitance (Figure 17).

2D materials having monolayer or multilayer displayed distinctive electronic properties than their counter bulk materials. Therefore, Rakhi et al. has synthesized 2D VO_2 nanosheets by simultaneous solution-reduction and exfoliation of V_2O_5 powder using hydrothermal approach and studied its application for supercapacitor.^[133] A device with 2D VO_2 nanosheets as electrodes was built which exhibited maximum specific energy of 46 Wh kg^{-1} at a power density of 1.4 kW kg^{-1} in the organic electrolyte (1M LiClO_4 in propylene carbonate). Further, the authors also fabricated a solid-state SSC device that exhibited 145 F g^{-1} of specific capacitance at 1 A g^{-1} current rate in gel electrolyte. The cyclic stability was analyzed by charging-discharging device up to 6000 cycles and found that the device retained 95% of initial capacitance. Like 2D sheets, 1D fibers especially carbon fibers are also considered as potential material owing to their high aspect ratio which can provide fast transport of electron. In 2017, Huang et al. had reported the fabrication of different vanadium oxide embedded carbon fibers to investigate its impact on supercapacitor application.^[4g] Three different vanadium oxides (V_xO_y) embedded in carbon fiber (CF) namely $\text{V}_2\text{O}_3/\text{CFs}$, $\text{VO}_2\text{-V}_2\text{O}_5/\text{CFs}$, and $\text{V}_2\text{O}_5/\text{CFs}$ were synthesized using different reaction conditions. The electrochemical performance was studied using Ni foam as a current collector and 4M KOH as an electrolyte in -0.1 to 0.6 V potential window. The estimated specific capacitance values for $\text{V}_2\text{O}_3/\text{CFs}$, $\text{VO}_2\text{-V}_2\text{O}_5/\text{CFs}$,

and $\text{V}_2\text{O}_5/\text{CFs}$ were 557 F g^{-1} , 476 F g^{-1} , and 606 F g^{-1} , respectively at 0.5 A g^{-1} . The synthesized $\text{V}_2\text{O}_3/\text{CFs}$ and $\text{VO}_2\text{-}\text{V}_2\text{O}_5/\text{CFs}$ show a negligible loss after 3000 cycles whereas $\text{V}_2\text{O}_5/\text{CFs}$ material shows 99% retention in capacitance at 5000th cycle as compared to capacitance at 2000th cycle. Later, 1D VO_2 based nanostructure material was also tested in fiber shaped supercapacitors devices due to high demand for flexible and wearable electronics. Thus, Man et al. grew a hierarchical $\text{VO}_2@$ polypyrrole ($\text{VO}_2@\text{PPy}$) core-shell NW arrays (NWAs) on carbon nanotube fiber (CNTF) as an electrode material for a fiber electrode for wearable electronics application.^[134] Authors built a fiber based asymmetric supercapacitor using $\text{VO}_2@\text{PPy}/\text{CNTF}$ as positive electrode and N-doped C coated VN NWAs on (CNTF VN@NC/CNTF) as negative electrode. The fiber device exhibited volumetric capacitance of 60.6 F cm^{-3} corresponding energy density of 29.3 mWh cm^{-3} at 250 mA cm^{-3} current density in 1.8 V potential window. Since the fabricated device was fiber shaped, the authors also carried out a bending test to observe the change in specific capacitance. The device retained 88.9% of capacitance after 4000 bending cycles. The performance can be attributed to the synergistic effect between VO_2 core that provides high surface area and PPy which suppresses VO_2 dissolution and hence electrode pulverization. In other findings, Zheng et al. prepared 1D $\text{VO}_2(\text{A})@\text{C}$ core-shell nanorods composites using glucose and V_2O_5 as precursors by hydrothermal method.^[135] The specific capacitance was 209 F g^{-1} at 100 mA g^{-1} current density evaluated from the discharge curve, whereas the capacitance retention was 56.3% after 1000 cycles. Authors fabricated an asymmetric supercapacitor device with flexibility using activated carbon as negative and $\text{VO}_2(\text{A})@\text{C}$ as positive electrode. The working potential window was 1.5 V for the hybrid device which showed 500 mF cm^{-2} of areal capacitance at a sweep rate of 5 mV s^{-1} . Also, the device exhibited a maximum of 714 mWh m^{-2} of areal energy and 3.75 W m^{-2} of areal power. However, cyclic stability of the device (34.6%) was poor, which might be due to the chemical dissolution of soluble vanadate ions. Authors found that by changing aqueous electrolyte with gel electrolyte (LiCl/PVA), cyclic stability was improved significantly with only 15% deterioration after 1600 cycles were observed, which was attributed to the presence of PVA that reduces the water content and also provide an elastic coating for structural stability. VO_2 crystallizes in different polymorphs to get insights about their effect on electrochemical performance. Basu et al. have prepared different phases of nanoporous VO_2 on carbon fiber studied them for supercapacitor applications.^[136] The electrochemical performance was studied in a half-cell configuration with aqueous Na_2SO_4 electrolyte. The material crystallized in monoclinic phase exhibited the best performance (capacitance of 33 mF cm^{-2} and capacitance degradation of only 6.3% up to 5000 cycles) than other triclinic and mixed phases.

One of the seminal studies published by Sahoo et al. has reported that synthesis of anodic reduced GO- VO_2 sheet-on-sheet heterostructure as high rate and high energy battery-supercapacitor hybrid (BSH) device.^[137] It was found that 2D transition metal dichalcogenides and graphene heterostructure can improve the interfacial interaction by enhancing the absorption of metal ions such as Li^+ and Na^+ that enhances the diffusion process.^[138] The group had focused to develop a

material to balance the interfacial kinetics of the electrodes. The charge storage behavior of synthesized anode rGO/ VO_2 composite was examined in $0.01\text{--}3.0 \text{ V}$ (vs Li/Li⁺) potential range. The specific capacity was estimated to be 1214 mAh g^{-1} at 0.1 A g^{-1} current density. The synthesized heterostructure provides better diffusion of ions due to enhancement in metal ion adsorption owing to improved interfacial interaction in 2D layer based heterostructure.^[137,138] Also, this kind of interface increases the electronic conductivity of composite material. For real-time application, a BSH device was fabricated using AC@CC (AC: activated carbon, CC: carbon cloth) as positive electrode and rGO@ VO_2 as a negative electrode. The device was examined in a $1\text{--}4 \text{ V}$ potential window to avoid any parasitic reactions if working potential is increased further. The capacity retention was observed $\approx 80\%$ after 10 000 cycles at a specific current of 2 A g^{-1} (Figure 18). The as fabricated hybrid device exhibits maximum energy density of 15.2 Wh kg^{-1} at a power density of $\approx 10\,000 \text{ W kg}^{-1}$ and energy density of 126.7 Wh kg^{-1} at a power density of 70 W kg^{-1} . Authors also examined the self-discharge rate of device by leaving the device at open-circuit conditions. Device showed retention of $\approx 70\%$ initial capacity up to 100 h.

VO_2 (D) was a recently discovered metastable phase that wasn't synthesized and electrochemically tested. Therefore, Kamila et al. had developed the VO_2 (D) phase having plate-like morphology and then prepared its composite with rGO.^[139] The VO_2 (D) phase consists of two VO_6 octahedra chains connected via corner-sharing O atoms. Two devices with symmetric and asymmetric (rGO was employed as negative electrode) configurations were fabricated. Authors optimized the percentage of rGO for the better performance of the devices. The symmetric device showed the specific capacitance of 244 F g^{-1} at 1 A g^{-1} current rate and outstanding cyclic stability up to 5000 cycles without any significant loss in charge stored. In addition, for asymmetric coin-cell configured device the charge storage performance was measured up to 2 V which exhibited 17 F g^{-1} of specific capacity at 1 A g^{-1} current rate.

In addition, Ndiaye et al. reported the synthesis of VO_2 monoclinic sheets and carbonized iron-polyaniline nanograins.^[140] The asymmetric device using VO_2 as positive and carbonized iron-polyaniline as negative electrode exhibited a 47 mAh g^{-1} of specific capacity and 30 Wh kg^{-1} specific energy (713 W kg^{-1} of specific power) at a current density of 1 A g^{-1} in 1.6 V of the potential window. The device displayed 89% charge retention after 10k charge-discharge cycles. In another study, Nadiye et al. successfully synthesized an asymmetric supercapacitor device using $\text{VO}_2/\text{activated expanded graphite}$ (VO_2/AEG) composite as a positive electrode and carbon-vanadium oxy-nitride ($\text{C-V}_2\text{NO}$) as a negative electrode.^[141] The charge storage performance of device $\text{VO}_2/\text{AEG}/\text{C-V}_2\text{NO}$ was tested using 6 M KOH as an electrolyte in the working potential window of 1.8 V . The device exhibited specific energy of 41.6 Wh kg^{-1} with a corresponding specific power of 904 W kg^{-1} at 1 A g^{-1} current density. The device showed a loss of only 7% capacitance in 10 000 cycles. Dong et al. had reported $\text{V}_5\text{O}_{12}/\text{VO}_2$ heterojunction nanomaterial on a 3D graphite substrate.^[142] The $\text{V}_5\text{O}_{12}/\text{VO}_2$ electrode showed an areal capacitance of 5.03 F cm^{-2} (465 F g^{-1}) as compared to the V_5O_{12} and VO_2 counterparts in a 3 M LiCl electrolyte. As asymmetric supercapacitor device has been

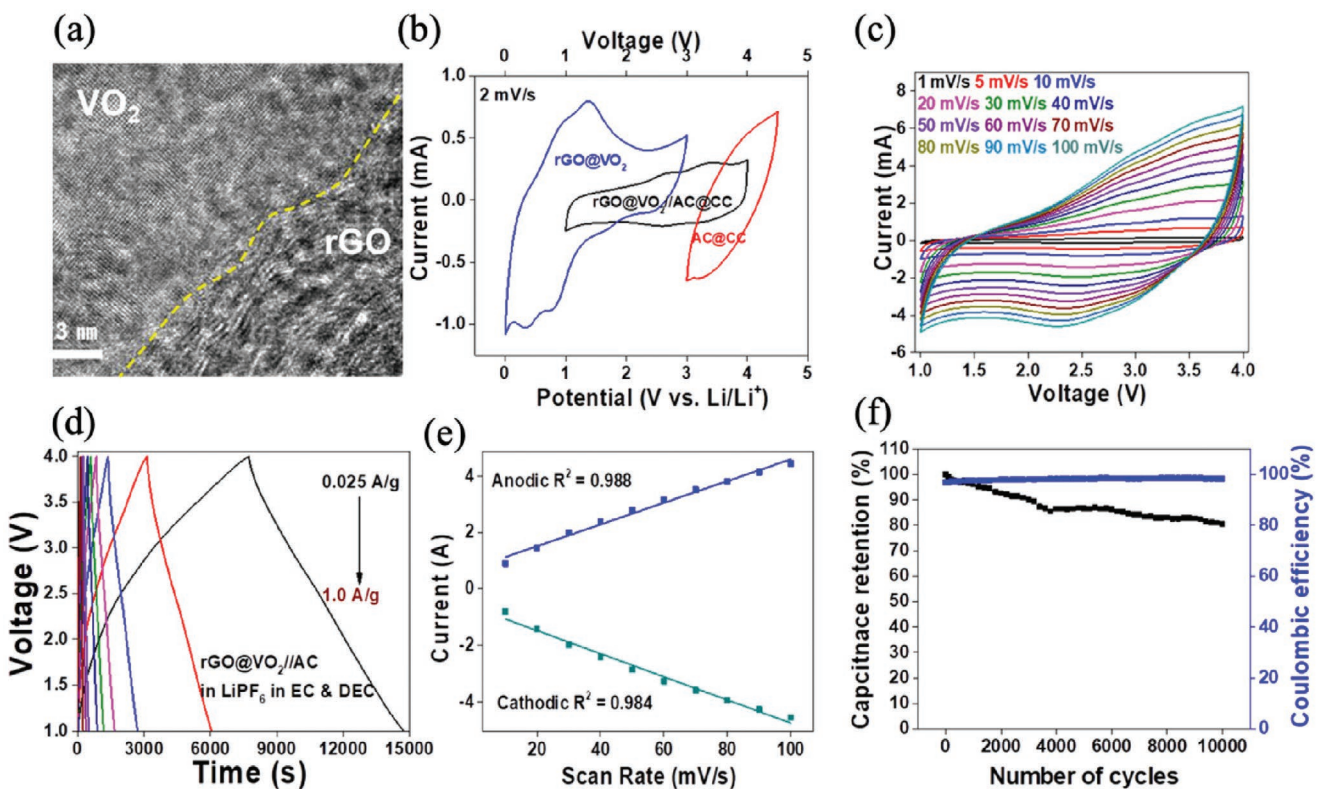


Figure 18. a) High-resolution TEM image of the rGO@VO₂ composite. b) CV of AC@CC, rGO@VO₂ in a half cell, and rGO@VO₂//AC@CC in a full cell. c) CV curves at different sweep rates and d) charge-discharge profiles at different current rates. e) Relationship between measured anodic (at 2.82 V) and cathodic (at 2.59 V) current with sweep rate. f) Cyclic stability and Coulombic efficiency curve of the hybrid device at 2 A g⁻¹ current rate. Reproduced with permission.^[137] Copyright 2019, American Chemical Society.

fabricated using V₅O₁₂/VO₂ and MnO₂ as negative and positive electrode respectively, exhibited areal/volumetric energy densities of 1.42 mWh cm⁻²/11.85 mWh cm⁻³ and deliver a cell voltage of 2 V with an energy density of \approx 18.6 Wh kg⁻¹ based on the active mass of the electrodes. Recently Du et al. reported Ni₃S₂@VO₂ nanorods as core-shell structure synthesized directly on the Ni foam.^[143] Ni foam provides a fast channel for electron transport. Ni₃S₂@VO₂ exhibited an areal capacitance of 1.09 C cm⁻² at 1 mA cm⁻². A SSC using Ni₃S₂@VO₂ shows the specific capacity of 0.864 C cm⁻² at a current of 1 mA cm⁻². Liu et al. prepared VO₂ based ternary composite namely, VO₂(B)/carbon nanotube/reduced GO [VO₂(B)/CNT/rGO] by hydrothermal approach.^[144] VO₂(B)/CNT/rGO showed specific capacitance of 649.1 F g⁻¹ at 0.5 A g⁻¹ and maximum energy density of 32.5 Wh kg⁻¹ with good cyclic stability up to 10 000 cycles (81.6% retention in capacitance). Overall, there has been significant interest among researchers to use VO₂ nanostructures and its composite for supercapacitor application. A number of different combinations have been attempted as explained above. Though many devices showed promising results in terms of cyclic stability and fast charging, specific energy in many devices is far from reality. It would be worth mentioning here that in most devices, the decay in specific capacitance is at initial cycles which may be due to the internal resistance and poor ionic conductivity of the electrode. It has been established that an increase in ionic conductivity of electrode can greatly

improve that specific capacitance of the electrode.^[145] However, there has not been any systematic study that correlates the effect of ionic and electronic conductivity on the performance of VO₂ based devices. Also, VO₂ is pseudocapacitive material which means that the charge storage process is at the near-surface and not at the bulk, therefore, increasing the surface area of electrode by nanoengineering or decrystallization methods can greatly enhance the charge storage capacity. Therefore, further research is needed to find a suitable composite or device combination for better performance.

5. Conclusion and Future Perspective

In this review, we provide a comprehensive and systematic overview of VO₂ nanostructures which include 0D, 1D, 2D, and 3D morphologies, and its detailed application in energy storage. The review contains discussions about different polymorphs of VO₂, their crystal structure, and detailed synthesis methods used to produce different morphologies and composite materials based on VO₂. A number of synthetic methods such as flame spray pyrolysis, chemical vapor condensation, thermal pyrolysis, etc. were employed to prepare VO₂ nano-materials. But in terms of controlling size and morphology, hydrothermal/solvothermal method was used largely. Though different polymorphs exist, among them, VO₂ (B) has been

studied extensively for energy storage application whereas, VO_2 (M) and VO_2 (R) has been extensively studied for electrochromic displays and memristors. Also, VO_2 (R) could be a suitable choice as electrode material for energy storage devices due to its intrinsic electronic conductivity, which is not studied extensively, nonetheless, it requires high temperature for synthesis. This review mainly focuses on the application of energy storage that includes Li-ion battery, Na-ion battery, Zn-ion battery, hybrid batteries, and supercapacitors using VO_2 as electrode material in aqueous and organic electrolytes. VO_2 (B) has an intrinsic advantage due to the tunneled structure which provides numerous sites for intercalation of metal ions and enough level of structural stability. However, bulk VO_2 (B) showed poor specific capacity, cyclic stability, and rate capability due to the low surface area and pulverization of electrodes originated from low electronic conductivity. To improve the performance of EES devices, electrodes made of VO_2 nanostructures were prepared which showed improved performance that includes better energy density and power density, however, the synthesis procedure requires additional cost and a complex development process which hampers the large-scale synthesis. In the future, more research should be focused on the synthesis of VO_2 nanostructure using wet chemical route to provide a cost-effective and large-scale synthesis method for enhanced charge storage performance.

Through using a variety of nanostructures, performance in terms of specific capacity and specific energy has been improved, but cyclic stability is still far from reality. Only a few reports exist which demonstrate that carbon-based composites improve electronic conductivity, cyclic stability, and structural stability. Nevertheless, the performance of electrode was further improved by making different nanostructures and composite which can provide a large surface to volume ratio, shorter diffusion path length, and more structural stability (due to volume changes originated by metal ion intercalation/deintercalation). Though 1D, 2D, and 3D VO_2 were prepared and its electrochemical performance was evaluated yet, there is no concrete study that can shed light on how morphology is related to electrochemical performance. But, based on the literature, it would be fair to say that 3D morphology of VO_2 including hollow spherical shape, microspheres, aerogel, etc. can improve the performance of materials by providing high surface area, better structural stability by sustaining volume changing. In electrochemical devices, both electronic and ionic conductivities are vital for a good performing electrode in terms of specific energy, specific power, and cyclic stability. VO_2 (B) displayed poor electronic conductivity ($\approx 1 \times 10^{-2} \text{ S cm}^{-1}$)^[146] which leads to the poor capacity and cyclic stability of electrodes in batteries. The electrical conductivity was improved using mainly graphene, but study related to ionic conductivity of VO_2 based electrode is still open. One effective strategy for an ionically conductive electrode could be the fabrication of a porous electrode.^[147] Therefore, in the future, research should be focused on the synthesis of porous electrodes which can improve the ionic conductivity of electrodes that can also help to improve the performance. In addition, MXenes and 2D layered materials can also be employed to make composite as an alternative material and investigate their performance of energy storage devices. It would be fascinating to study the change

in morphology, and electronic conductivity of composite with MXene and 2D layered materials and their application for metal ion storage in both organic and aqueous electrolytes. Due to the low cost and high availability, Ca and Mg ion-based batteries are currently attracting significant research attention. Future research directions for VO_2 should also be focused on its usage in multivalent ion batteries. These new alternative nanostructured materials with VO_2 and new metal ion-based batteries will certainly provide a new path for the fabrication of large scale and cost-effective energy storage devices.

Acknowledgements

S.R.M. thanks to Jain University for Junior Research Fellowship. M.S. thanks to SERB, New Delhi for research funding (EMR/2017/003368).

Conflict of Interest

The authors declare no conflict of interest.

Keywords

Li-ion batteries, Na ion batteries, supercapacitors, VO_2 nanostructures, Zn ion batteries

Received: October 25, 2020

Published online: December 28, 2020

- [1] a) Z. Khan, M. Vagin, X. Crispin, *Adv. Sci.* **2020**, *7*, 1902866; b) C. F. Armer, J. S. Yeoh, X. Li, A. Lowe, *J. Power Sources* **2018**, *395*, 414; c) P. Liu, K. Zhu, Y. Gao, H. Luo, L. Lu, *Adv. Energy Mater.* **2017**, *7*, 1700547.
- [2] a) L. F. Nazar, G. Goward, F. Leroux, M. Duncan, H. Huang, T. Kerr, J. Gaubicher, *Int. J. Inorg. Mater.* **2001**, *3*, 191; b) D. Bhardwaj, A. Goswami, A. Umarji, *J. Appl. Phys.* **2018**, *124*, 135301; c) Z. Khan, S. Park, S. M. Hwang, J. Yang, Y. Lee, H.-K. Song, Y. Kim, H. Ko, *NPG Asia Mater.* **2016**, *8*, e294; d) Z. Khan, B. Senthilkumar, S. Lim, R. Shanker, Y. Kim, H. Ko, *Adv. Mater. Interfaces* **2017**, *4*, 1700059; e) Z. Khan, S. Bhattu, S. Haram, D. Khushalani, *RSC Adv.* **2014**, *4*, 17378; f) B. Senthilkumar, Z. Khan, S. Park, K. Kim, H. Ko, Y. Kim, *J. Mater. Chem. A* **2015**, *3*, 21553; g) Z. Khan, N. Parveen, S. A. Ansari, S. T. Senthilkumar, S. Park, Y. Kim, M. H. Cho, H. Ko, *Electrochim. Acta* **2017**, *257*, 328; h) N. Parveen, Z. Khan, S. A. Ansari, S. Park, S. T. Senthilkumar, Y. Kim, H. Ko, M. H. Cho, *Chem. Eng. J.* **2019**, *360*, 415; i) S. Park, Z. Khan, T. J. Shin, Y. Kim, H. Ko, *J. Mater. Chem. A* **2019**, *7*, 1564; j) N. Parveen, S. A. Ansari, H. R. Alamri, M. O. Ansari, Z. Khan, M. H. Cho, *ACS Omega* **2018**, *3*, 1581; k) M. Shao, R. Zhang, Z. Li, M. Wei, D. G. Evans, X. Duan, *Chem. Comm.* **2015**, *51*, 15880; l) C. M. Julien, A. Mauger, *Nanomaterials* **2017**, *7*, 396; m) J. Shin, J. K. Seo, R. Yaylian, A. Huang, Y. S. Meng, *Int. Mater. Rev.* **2019**, *65*, 356.
- [3] a) T. Jayaraman, A. P. Murthy, V. Elakkiya, S. Chandrasekaran, P. Nithyadhaseni, Z. Khan, R. A. Senthil, R. Shanker, M. Raghavender, P. Kuppusami, M. Jagannathan, M. Ashokkumar, *J. Ind. Eng. Chem.* **2018**, *64*, 16; b) Z. Khan, S. O. Park, J. Yang, S. Park, R. Shanker, H.-K. Song, Y. Kim, S. K. Kwak, H. Ko, *J. Mater. Chem. A* **2018**, *6*, 24459; c) Q. Wu, L. Yang, X. Wang, Z. Hu, *Adv. Mater.* **2020**, *32*, 1904177; d) B. Senthilkumar, C. Murugesan,

- L. Sharma, S. Lochab, P. Barpanda, *Small Methods* **2019**, *3*, 1800253; e) S. A. Ansari, Z. Khan, M. O. Ansari, M. H. Cho, *RSC Adv.* **2016**, *6*, 44616.
- [4] a) D. Chao, C. Zhu, X. Xia, J. Liu, X. Zhang, J. Wang, P. Liang, J. Lin, H. Zhang, Z. X. Shen, H. J. Fan, *Nano Lett.* **2015**, *15*, 565; b) D. Chao, X. Xia, J. Liu, Z. Fan, C. F. Ng, J. Lin, H. Zhang, Z. X. Shen, H. J. Fan, *Adv. Mater.* **2014**, *26*, 5794; c) S. Yang, Y. Gong, Z. Liu, L. Zhan, D. P. Hashim, L. Ma, R. Vajtai, P. M. Ajayan, *Nano Lett.* **2013**, *13*, 1596; d) M. Yan, F. Wang, C. Han, X. Ma, X. Xu, Q. An, L. Xu, C. Niu, Y. Zhao, X. Tian, P. Hu, H. Wu, L. Mai, *J. Am. Chem. Soc.* **2013**, *135*, 18176; e) J. Liu, H. Xia, D. Xue, L. Lu, *J. Am. Chem. Soc.* **2009**, *131*, 12086; f) X. Liu, R. Liu, L. Zeng, X. Huang, X. Chen, C. Zheng, Y. Xu, Q. Qian, M. Wei, Q. Chen, *New J. Chem.* **2017**, *41*, 5380; g) G. Huang, C. Li, X. Sun, J. Bai, *New J. Chem.* **2017**, *41*, 8977; h) A. Pan, H. B. Wu, L. Yu, T. Zhu, X. W. Lou, *ACS Appl. Mater. Interfaces* **2012**, *4*, 3874; i) D. McNulty, D. N. Buckley, C. O'Dwyer, *J. Power Sources* **2014**, *267*, 831; j) N. Bahlawane, D. Lenoble, *Chem. Vap. Deposition* **2014**, *20*, 299.
- [5] a) P. G. Bruce, B. Scrosati, J.-M. Tarascon, *Angew. Chem., Int. Ed.* **2008**, *47*, 2930; b) A. Mauger, C. M. Julien, *AIMS Mater. Sci.* **2018**, *5*, 349.
- [6] A. Pan, J.-G. Zhang, Z. Nie, G. Cao, B. W. Arey, G. Li, S.-q. Liang, J. Liu, *J. Mater. Chem.* **2010**, *20*, 9193.
- [7] Y. Ji, S. Li, G. Zhong, Z. Zhang, Y. Li, M. J. McDonald, Y. Yang, *J. Electrochem. Soc.* **2015**, *162*, A7015.
- [8] X.-L. Wu, L.-Y. Jiang, F.-F. Cao, Y.-G. Guo, L.-J. Wan, *Adv. Mater.* **2009**, *21*, 2710.
- [9] a) J. Shin, H. Jung, Y. Kim, J. Kim, *J. Alloys Compd.* **2014**, *589*, 322; b) Y. Wang, K. Takahashi, K. H. Lee, G. Z. Cao, *Adv. Funct. Mater.* **2006**, *16*, 1133.
- [10] S. Li, J.-B. Liu, Q. Wan, J. Xu, B.-X. Liu, *Chem. Mater.* **2017**, *29*, 10075.
- [11] a) C. Tsang, A. Manthiram, *J. Electrochem. Soc.* **1997**, *144*, 520; b) L. Zhang, K. Zhao, W. Xu, J. Meng, L. He, Q. An, X. Xu, Y. Luo, T. Zhao, L. Mai, *RSC Adv.* **2014**, *4*, 33332; c) L. Mai, Q. Wei, Q. An, X. Tian, Y. Zhao, X. Xu, L. Xu, L. Chang, Q. Zhang, *Adv. Mater.* **2013**, *25*, 2969.
- [12] X. Xia, D. Chao, C. F. Ng, J. Lin, Z. Fan, H. Zhang, Z. X. Shen, H. J. Fan, *Mater. Horiz.* **2015**, *2*, 237.
- [13] V. Yadav, S. Roy, P. Singh, Z. Khan, A. Jaiswal, *Small* **2019**, *15*, 1803706.
- [14] a) M. Liu, B. Su, Y. Tang, X. Jiang, A. Yu, *Adv. Energy Mater.* **2017**, *7*, 1700885; b) H. T. Tan, X. Rui, W. Sun, Q. Yan, T. M. Lim, *Nanoscale* **2015**, *7*, 14595; c) Y. Cheng, Y. Xia, Y. Chen, Q. Liu, T. Ge, L. Xu, L. Mai, Y. Ke, Y. Zhou, P. Hu, S. Magdassi, Y. Long, *Appl. Energy* **2018**, *211*, 200.
- [15] a) Z. Shao, X. Cao, H. Luo, P. Jin, *NPG Asia Mater.* **2018**, *10*, 581; b) C. Drosos, D. Vernardou, *Materials* **2018**, *11*, 384; c) R. Heckingbottom, J. W. Linnett, *Nature* **1962**, *194*, 678; d) A. Srivastava, H. Rotella, S. Saha, B. Pal, G. Kalon, S. Mathew, M. Motapothula, M. Dykas, P. Yang, E. Okunishi, D. D. Sarma, T. Venkatesan, *APL Mater.* **2015**, *3*, 026101.
- [16] a) A. Joushaghani, J. Jeong, S. Paradis, D. Alain, J. Stewart Aitchison, J. K. S. Poon, *Opt. Express* **2015**, *23*, 3657; b) T. Driscoll, H.-T. Kim, B.-G. Chae, M. D. Ventra, D. N. Basov, *Appl. Phys. Lett.* **2009**, *95*, 043503.
- [17] M. E. A. Warwick, R. Binions, *J. Mater. Chem. A* **2014**, *2*, 3275.
- [18] J. B. Goodenough, *J. Solid State Chem.* **1971**, *3*, 490.
- [19] V. Eyert, *Ann. Phys.* **2002**, *11*, 650.
- [20] D. W. Murphy, P. A. Christian, F. J. DiSalvo, J. N. Carides, J. V. Waszczak, *J. Electrochem. Soc.* **1981**, *128*, 2053.
- [21] a) C. Leroux, G. Nihoul, G. Van Tendeloo, *Phys. Rev. B* **1998**, *57*, 5111; b) N. A. Chernova, M. Roppolo, A. C. Dillon, M. S. Whittingham, *J. Mater. Chem.* **2009**, *19*, 2526; c) S. Zhang, Y. Li, C. Wu, F. Zheng, Y. Xie, *J. Phys. Chem. C* **2009**, *113*, 15058; d) J.-Y. Luo, W.-J. Cui, P. He, Y.-Y. Xia, *Nat. Chem.* **2010**, *2*, 760.
- [22] F. Théobald, R. Cabala, J. Bernard, *J. Solid State Chem.* **1976**, *17*, 431.
- [23] a) C. Wu, Z. Hu, W. Wang, M. Zhang, J. Yang, Y. Xie, *Chem. Comm.* **2008**, 3891; b) Y. Xu, L. Zheng, Y. Xie, *Dalton Trans.* **2010**, *39*, 10729.
- [24] P. A. Christian, F. J. DiSalvo, D. W. Murphy, US Patent 4228226, 1980.
- [25] a) R. Nesper, H.-J. Muhr, *CHIMIA Int. J. Chem.* **1998**, *52*, 571; b) M. E. Spahr, P. Bitterli, R. Nesper, M. Müller, F. Krumeich, H. U. Nissen, *Angew. Chem., Int. Ed.* **1998**, *37*, 1263.
- [26] W. Zeng, N. Chen, W. Xie, *CrystEngComm* **2020**, *22*, 851.
- [27] a) T. Chirayil, P. Y. Zavalij, M. S. Whittingham, *Chem. Mater.* **1998**, *10*, 2629; b) J. Livage, *Materials* **2010**, *3*, 4175.
- [28] J. Zou, L. Xiao, L. Zhu, X. Chen, *J. Sol-Gel Sci. Tech.* **2019**, *91*, 302.
- [29] C. Cao, Y. Gao, H. Luo, *J. Phys. Chem. C* **2008**, *112*, 18810.
- [30] J.-H. Son, J. Wei, D. Cobden, G. Cao, Y. Xia, *Chem. Mater.* **2010**, *22*, 3043.
- [31] a) M. Li, D. B. Li, J. Pan, J. C. Lin, G. H. Li, *Eur. J. Inorg. Chem.* **2013**, *2013*, 1207; b) D. Alie, L. Gedvilas, Z. Wang, R. Tenant, C. Engrakul, Y. Yan, S. E. Shaheen, A. C. Dillon, C. Ban, *J. Solid State Chem.* **2014**, *212*, 237; c) S. Ji, Y. Zhao, F. Zhang, P. Jin, J. Cryst. Growth **2010**, *312*, 282; d) R. Chen, L. Miao, C. Liu, J. Zhou, H. Cheng, T. Asaka, Y. Iwamoto, S. Tanemura, *Sci. Rep.* **2015**, *5*, 14087.
- [32] a) D. Malarde, I. D. Johnson, I. J. Godfrey, M. J. Powell, G. Cibin, R. Quesada-Cabrera, J. A. Darr, C. J. Carmalt, G. Sankar, I. P. Parkin, *J. Mater. Chem. C* **2018**, *6*, 11731; b) J. Zhu, A. Huang, H. Ma, Y. Ma, K. Tong, S. Ji, S. Bao, X. Cao, P. Jin, *ACS Appl. Mater. Interfaces* **2016**, *8*, 29742.
- [33] Z. Peng, W. Jiang, H. Liu, *J. Phys. Chem. C* **2007**, *111*, 11119.
- [34] S. Guan, A. Rougier, O. Viraphong, D. Denux, N. Penin, M. Gaudon, *Inorg. Chem.* **2018**, *57*, 8857.
- [35] H. Zhang, X. Xiao, X. Lu, G. Chai, Y. Sun, Y. Zhan, G. Xu, *J. Alloys Compd.* **2015**, *636*, 106.
- [36] W. Zeng, H. Lai, T. Chen, Y. Lu, Z. Liang, T. Shi, K. Chen, P. Liu, F. Xie, J. Chen, *CrystEngComm* **2019**, *21*, 5749.
- [37] E. Fuls, D. Hensler, A. Ross, *Appl. Phys. Lett.* **1967**, *10*, 199.
- [38] S. Chen, H. Ma, J. Dai, X. Yi, *Appl. Phys. Lett.* **2007**, *90*, 101117.
- [39] H. Zhang, Z. Wu, X. Wu, W. Yang, Y. Jiang, *Vacuum* **2014**, *104*, 47.
- [40] Y. Zhang, R. Wang, Z. Qiu, X. Wu, Y. Li, *Mater. Lett.* **2014**, *131*, 42.
- [41] K. Nishikawa, Y. Kishida, K. Ito, S.-i. Tamura, Y. Takeda, *Appl. Phys. Lett.* **2017**, *111*, 193102.
- [42] B. Fang, Y. Li, G. Tong, X. Wang, M. Yan, Q. Liang, F. Wang, Y. Qin, J. Ding, S. Chen, *Opt. Mater.* **2015**, *47*, 225.
- [43] M. Borek, F. Qian, V. Nagabushnam, R. Singh, *Appl. Phys. Lett.* **1993**, *63*, 3288.
- [44] R. Teghil, L. D'Alessio, A. De Bonis, A. Galasso, N. Ibris, A. M. Salvi, A. Santagata, P. Villani, *J. Phys. Chem. A* **2009**, *113*, 14969.
- [45] S. Majid, D. Shukla, F. Rahman, K. Gautam, V. Sathe, R. Choudhary, D. Phase, *J. Phys.: Conf. Ser.* **2016**, *755*, 012027.
- [46] a) G. J. Fang, Z. Liu, Y. Wang, Y. Liu, K. Yao, *J. Vac. Sci. Technol., A* **2001**, *19*, 887; b) K. Shibuya, A. Sawa, *AIP Adv.* **2015**, *5*, 107118; c) B. Masina, S. Lafane, L. Wu, S. Abdelli-Messaci, T. Kerdja, A. Forbes, in *Quantum Dots Nanostruct.: Synth., Charact., Model.* XI (Eds: D. L. Huffaker, F. Szmulowicz, H. Eisele), International Society for Optics and Photonics, San Francisco **2014**.
- [47] P. S. Patil, *Mater. Chem. Phys.* **1999**, *59*, 185.
- [48] V. B. Kamble, A. M. Umarji, *J. Mater. Chem. C* **2013**, *1*, 8167.
- [49] I. J. Tadeo, E. P. Mukhokosi, S. B. Krupanidhi, A. M. Umarji, *RSC Adv.* **2019**, *9*, 9983.
- [50] R. Bharathi, R. Naorem, A. Umarji, *J. Phys. D: Appl. Phys.* **2015**, *48*, 305103.
- [51] C. Wu, J. Dai, X. Zhang, J. Yang, F. Qi, C. Gao, Y. Xie, *Angew. Chem., Int. Ed.* **2010**, *49*, 134.

- [52] a) D. Li, Y. Xia, *Adv. Mater.* **2004**, *16*, 1151; b) R. Berenguer, M. O. Guerrero-Pérez, I. Guzmán, J. Rodríguez-Mirasol, T. s. Cordero, *ACS Omega* **2017**, *2*, 7739.
- [53] O. Y. Berezina, N. Markova, E. Kolobova, A. Pergament, D. Yakovleva, V. Zlomanov, N. Krivoshchapov, *Micro Nanosyst.* **2020**, *12*, 68.
- [54] R. Lopez, L. C. Feldman, R. F. Haglund Jr, *Phys. Rev. Lett.* **2004**, *93*, 177403.
- [55] K. Appavoo, D. Y. Lei, Y. Sonnenfraud, B. Wang, S. T. Pantelides, S. A. Maier, R. F. Haglund Jr, *Nano Lett.* **2012**, *12*, 780.
- [56] S. Ding, Z. Liu, D. Li, W. Zhao, Y. Wang, D. Wan, F. Huang, *ACS Appl. Mater. Interfaces* **2013**, *5*, 1630.
- [57] S.-D. Lan, C.-C. Cheng, C.-H. Huang, J.-K. Chen, *Appl. Surf. Sci.* **2015**, *357*, 2069.
- [58] G. Armstrong, J. Canales, A. R. Armstrong, P. G. Bruce, *J. Power Sources* **2008**, *178*, 723.
- [59] C. Nethravathi, B. Viswanath, J. Michael, M. Rajamath, *Carbon* **2012**, *50*, 4839.
- [60] G. He, L. Li, A. Manthiram, *J. Mater. Chem. A* **2015**, *3*, 14750.
- [61] X. Rui, D. Sim, C. Xu, W. Liu, H. Tan, K. Wong, H. H. Hng, T. M. Lim, Q. Yan, *RSC Adv.* **2012**, *2*, 1174.
- [62] X. Wang, J. Huang, J. Liu, X. Sun, L. Wang, X. He, *Int. J. Electrochem. Sci.* **2011**, *6*, 1709.
- [63] H. Li, P. He, Y. Wang, E. Hosono, H. Zhou, *J. Mater. Chem.* **2011**, *21*, 10999.
- [64] W. Wang, B. Jiang, L. Hu, Z. Lin, J. Hou, S. Jiao, *J. Power Sources* **2014**, *250*, 181.
- [65] M. M. Rahman, J.-Z. Wang, N. H. Idris, Z. Chen, H. Liu, *Electrochim. Acta* **2010**, *56*, 693.
- [66] G. Ren, M. N. F. Hoque, X. Pan, J. Warzywoda, Z. Fan, *J. Mater. Chem. A* **2015**, *3*, 10787.
- [67] G. Ren, X. Pan, S. Bayne, Z. Fan, *Carbon* **2014**, *71*, 94.
- [68] H. Liu, Y. Wang, K. Wang, E. Hosono, H. Zhou, *J. Mater. Chem.* **2009**, *19*, 2835.
- [69] F. Wang, Y. Liu, C.-y. Liu, *Electrochim. Acta* **2010**, *55*, 2662.
- [70] J. Ni, W. Jiang, K. Yu, Y. Gao, Z. Zhu, *Electrochim. Acta* **2011**, *56*, 2122.
- [71] J. M. Won, Y. N. Ko, J.-K. Lee, Y. C. Kang, *Electrochim. Acta* **2015**, *156*, 179.
- [72] S. Park, C. W. Lee, J.-C. Kim, H. J. Song, H.-W. Shim, S. Lee, D.-W. Kim, *ACS Energy Lett.* **2016**, *1*, 216.
- [73] a) J. Stangl, V. Holý, G. Bauer, *Rev. Mod. Phys.* **2004**, *76*, 725; b) C. Teichert, *Phys. Rep.* **2002**, *365*, 335.
- [74] S. Li, G. Liu, J. Liu, Y. Lu, Q. Yang, L.-Y. Yang, H.-R. Yang, S. Liu, M. Lei, M. Han, *J. Mater. Chem. A* **2016**, *4*, 6426.
- [75] M. Chen, X. Liang, F. Wang, D. Xie, G. Pan, X. Xia, *J. Mater. Chem. A* **2019**, *7*, 6644.
- [76] B. Yan, X. Li, Z. Bai, L. Lin, G. Chen, X. Song, D. Xiong, D. Li, X. Sun, *J. Mater. Chem. A* **2017**, *5*, 4850.
- [77] Z. Khan, B. Senthilkumar, S. O. Park, S. Park, J. Yang, J. H. Lee, H.-K. Song, Y. Kim, S. K. Kwak, H. Ko, *J. Mater. Chem. A* **2017**, *5*, 2037.
- [78] F. Wu, Y. Jiang, Z. Ye, Y. Huang, Z. Wang, S. Li, Y. Mei, M. Xie, L. Li, R. Chen, *J. Mater. Chem. A* **2019**, *7*, 1315.
- [79] Y. Gao, C. Cao, L. Dai, H. Luo, M. Kanehira, Y. Ding, Z. L. Wang, *Energy Environ. Sci.* **2012**, *5*, 8708.
- [80] W. Li, S. Ji, Y. Li, A. Huang, H. Luo, P. Jin, *RSC Adv.* **2014**, *4*, 13026.
- [81] S. P. Rao, M. Miclau, A. Artemenko, C. Labrugere, A. Villesuzanne, M. Pollet, *Inorg. Chem.* **2013**, *52*, 4780.
- [82] Y. L. Zhong, Y. F. Zhang, X. Liu, X. H. Liu, C. Huang, H. B. Li, *Adv. Mater. Res.* **2011**, *295–297*, 368.
- [83] Z. Song, L. Zhang, F. Xia, N. A. Webster, J. Song, B. Liu, H. Luo, Y. Gao, *Inorg. Chem. Front.* **2016**, *3*, 1035.
- [84] C. Zheng, J. Zhang, G. Luo, J. Ye, M. Wu, *J. Mater. Sci.* **2000**, *35*, 3425.
- [85] Y. Wang, N. Song, X. Song, T. Zhang, Q. Zhang, M. Li, *RSC Adv.* **2018**, *8*, 10848.
- [86] W. Li, J. R. Dahn, D. S. Wainwright, *Science* **1994**, *264*, 1115.
- [87] M. S. Whittingham, *J. Electrochem. Soc.* **1976**, *123*, 315.
- [88] T. V. Buurn, U. V. Sacken, J. R. Dahn, US Patent 4965150, **1990**.
- [89] A. M. Kannan, A. Manthiram, *Solid State Ionics* **2003**, *159*, 265.
- [90] C. Wen, P. Junfeng, M. Liqiang, Y. Hua, Q. Yanyuan, *Chem. Lett.* **2004**, *33*, 894.
- [91] E. Baudrin, G. Sudant, D. Larcher, B. Dunn, J.-M. Tarascon, *Chem. Mater.* **2006**, *18*, 4369.
- [92] C. Nethravathi, C. R. Rajamathi, M. Rajamathi, U. K. Gautam, X. Wang, D. Golberg, Y. Bando, *ACS Appl. Mater. Interfaces* **2013**, *5*, 2708.
- [93] B. Zachau-Christiansen, K. West, T. Jacobsen, *Mater. Res. Bull.* **1985**, *20*, 485.
- [94] C. Niu, J. Meng, C. Han, K. Zhao, M. Yan, L. Mai, *Nano Lett.* **2014**, *14*, 2873.
- [95] a) R. E. Warburton, H. Iddir, L. A. Curtiss, J. Greeley, *ACS Appl. Mater. Interfaces* **2016**, *8*, 11108; b) J. C. Hunter, *J. Solid State Chem.* **1981**, *39*, 142.
- [96] N. B. Mahadi, J.-S. Park, J.-H. Park, K. Y. Chung, S. Y. Yi, Y.-K. Sun, S.-T. Myung, *J. Power Sources* **2016**, *326*, 522.
- [97] J. Xie, Q. Zhang, *Small* **2019**, *15*, 1805061.
- [98] C. Pei, F. Xiong, J. Sheng, Y. Yin, S. Tan, D. Wang, C. Han, Q. An, L. Mai, *ACS Appl. Mater. Interfaces* **2017**, *9*, 17060.
- [99] T. Luo, Y. Liu, H. Su, R. Xiao, L. Huang, Q. Xiang, Y. Zhou, C. Chen, *Electrochim. Acta* **2018**, *260*, 805.
- [100] Y. Cen, S. Li, Y. Zhou, X. Cai, X. Wang, Q. Xiang, B. Hu, D. Yu, Y. Liu, C. Chen, *J. Electrochem. Soc.* **2019**, *166*, A1660.
- [101] a) J. Ding, Z. Du, L. Gu, B. Li, L. Wang, S. Wang, Y. Gong, S. Yang, *Adv. Mater.* **2018**, *30*, 1800762; b) L. Chen, Y. Ruan, G. Zhang, Q. Wei, Y. Jiang, T. Xiong, P. He, W. Yang, M. Yan, Q. An, L. Mai, *Chem. Mater.* **2019**, *31*, 699; c) Z. Li, S. Ganapathy, Y. Xu, Z. Zhou, M. Sarilar, M. Wagemaker, *Adv. Energy Mater.* **2019**, *9*, 1900237.
- [102] T. Wei, Q. Li, G. Yang, C. Wang, *J. Mater. Chem. A* **2018**, *6*, 8006.
- [103] X. Dai, F. Wan, L. Zhang, H. Cao, Z. Niu, *Energy Storage Mater.* **2019**, *17*, 143.
- [104] L. Zhang, L. Miao, B. Zhang, J. Wang, J. Liu, Q. Tan, H. Wan, J. Jiang, *J. Mater. Chem. A* **2020**, *8*, 1731.
- [105] Z. Li, Y. Ren, L. Mo, C. Liu, K. Hsu, Y. Ding, X. Zhang, X. Li, L. Hu, D. Ji, G. Cao, *ACS Nano* **2020**, *14*, 5581.
- [106] G. Yang, Q. Li, K. Ma, C. Hong, C. Wang, *J. Mater. Chem. A* **2020**, *8*, 8084.
- [107] Q. Pang, H. Zhao, R. Lian, Q. Fu, Y. Wei, A. Sarapulova, J. Sun, C. Wang, G. Chen, H. Ehrenberg, *J. Mater. Chem. A* **2020**, *8*, 9567.
- [108] Y. Liu, P. Hu, H. Liu, X. Wu, C. Zhi, *Mater. Today Energy* **2020**, *17*, 100431.
- [109] F. Cui, J. Zhao, D. Zhang, Y. Fang, F. Hu, K. Zhu, *Chem. Eng. J.* **2020**, *390*, 124118.
- [110] X. Liu, G. Xu, Q. Zhang, S. Huang, L. Li, X. Wei, J. Cao, L. Yang, P. K. Chu, *J. Power Sources* **2020**, *463*, 228223.
- [111] F. Wang, O. Borodin, T. Gao, X. Fan, W. Sun, F. Han, A. Faraone, J. A. Dura, K. Xu, C. Wang, *Nat. Mater.* **2018**, *17*, 543.
- [112] Y. Song, W. Zhao, L. Kong, L. Zhang, X. Zhu, Y. Shao, F. Ding, Q. Zhang, J. Sun, Z. Liu, *Energy Environ. Sci.* **2018**, *11*, 2620.
- [113] N. Gangangappa, A. Siddaramanna, *Mater. Characterization* **2012**, *68*, 58.
- [114] X. Zhou, G. Wu, J. Wu, H. Yang, J. Wang, G. Gao, *Phys. Chem. Chem. Phys.* **2014**, *16*, 3973.
- [115] B. Xiao, B. Zhang, J.-c. Zheng, L.-b. Tang, C.-s. An, Z.-j. He, H. Tong, W.-j. Yu, *Ceram. Int.* **2018**, *44*, 13113.
- [116] L. Liu, Q. Liu, W. Zhao, G. Li, L. Wang, W. Shi, L. Chen, *Nanotechnology* **2017**, *28*, 065404.
- [117] X. Hu, Z. Zhao, L. Wang, J. Li, C. Wang, Y. Zhao, H. Jin, *Electrochim. Acta* **2019**, *293*, 97.

- [118] S. Zeng, C. Wang, H. Li, J. Wang, X. Xu, B. Wu, B. He, *Chem. Lett.* **2019**, *48*, 367.
- [119] W. Guo, Y. Wang, Q. Li, D. Wang, F. Zhang, Y. Yang, Y. Yu, *ACS Appl. Mater. Interfaces* **2018**, *10*, 14993.
- [120] H. J. Song, M. Choi, J.-C. Kim, S. Park, C. W. Lee, S.-H. Hong, B.-K. Kim, D.-W. Kim, *Sci. Rep.* **2016**, *6*, 30202.
- [121] Y. Zhang, J. Zheng, T. Hu, F. Tian, C. Meng, *Appl. Surf. Sci.* **2016**, *371*, 189.
- [122] X. Pan, Y. Zhao, G. Ren, Z. Fan, *Chem. Comm.* **2013**, *49*, 3943.
- [123] G. Wang, Y. Ling, Y. Li, *Nanoscale* **2012**, *4*, 6682.
- [124] H. Wang, H. Yi, X. Chen, X. Wang, *J. Mater. Chem. A* **2014**, *2*, 1165.
- [125] M. Lee, B.-H. Wee, J.-D. Hong, *Adv. Energy Mater.* **2015**, *5*, 1401890.
- [126] J. Wang, X. Zhang, Y. Zhang, A. Abas, X. Zhao, Z. Yang, Q. Su, W. Lan, E. Xie, *RSC Adv.* **2017**, *7*, 35558.
- [127] R. Sahoo, D. T. Pham, T. H. Lee, T. H. T. Luu, J. Seok, Y. H. Lee, *ACS Nano* **2018**, *12*, 8494.
- [128] C. Hu, H. Xu, X. Liu, F. Zou, L. Qie, Y. Huang, X. Hu, *Sci. Rep.* **2015**, *5*, 16012.
- [129] H.-Y. Li, C. Wei, L. Wang, Q.-S. Zuo, X. Li, B. Xie, *J. Mater. Chem. A* **2015**, *3*, 22892.
- [130] Y. Zhang, X. Jing, Y. Cheng, T. Hu, M. Changgong, *Inorg. Chem. Front.* **2018**, *5*, 2798.
- [131] H.-C. Chen, Y.-C. Lin, Y.-L. Chen, C.-J. Chen, *ACS Appl. Energy Mater.* **2019**, *2*, 459.
- [132] W. Lv, C. Yang, G. Meng, R. Zhao, A. Han, R. Wang, J. Liu, *Sci. Rep.* **2019**, *9*, 10831.
- [133] R. B. Rakhi, D. H. Nagaraju, P. Beaujuge, H. N. Alshareef, *Electrochim. Acta* **2016**, *220*, 601.
- [134] P. Man, Q. Zhang, J. Sun, J. Guo, X. Wang, Z. Zhou, B. He, Q. Li, L. Xie, J. Zhao, C. Li, Q. Li, Y. Yao, *Carbon* **2018**, *139*, 21.
- [135] J. Zheng, Y. Zhang, Q. Wang, H. Jiang, Y. Liu, T. Lv, C. Meng, *Dalton Trans.* **2018**, *47*, 452.
- [136] R. Basu, S. Ghosh, S. Bera, A. Das, S. Dhara, *Sci. Rep.* **2019**, *9*, 4621.
- [137] R. Sahoo, T. H. Lee, D. T. Pham, T. H. T. Luu, Y. H. Lee, *ACS Nano* **2019**, *13*, 10776.
- [138] a) K. Roy, M. Padmanabhan, S. Goswami, T. P. Sai, G. Ramalingam, S. Raghavan, A. Ghosh, *Nat. Nanotechnol.* **2013**, *8*, 826; b) D. Su, S. Dou, G. Wang, *Chem. Comm.* **2014**, *50*, 4192.
- [139] S. Kamila, B. Chakraborty, S. Basu, B. K. Jena, *J. Phys. Chem. C* **2019**, *123*, 24280.
- [140] N. M. Ndiaye, M. J. Madito, B. D. Ngom, T. M. Masikhwa, A. A. Mirghni, N. Manyala, *AIP Adv.* **2019**, *9*, 055309.
- [141] N. M. Ndiaye, N. F. Sylla, B. D. Ngom, F. Barzegar, D. Momodu, N. Manyala, *Electrochim. Acta* **2019**, *316*, 19.
- [142] R. Dong, Y. Song, D. Yang, H.-Y. Shi, Z. Qin, M. Zhang, D. Guo, X. Sun, X.-X. Liu, *J. Mater. Chem. A* **2020**, *8*, 1176.
- [143] H. Du, F. Ding, J. Zhao, X. Zhang, Y. Li, Y. Zhang, J. Li, X. Yang, K. Li, Y. Yang, *Appl. Surf. Sci.* **2020**, *508*, 144876.
- [144] Y. Liu, Y. Zhang, T. Hu, Y. Mu, J. Sun, J. Zheng, H. Jiang, X. Dong, C. Meng, *Colloids Surf. A* **2020**, *586*, 124222.
- [145] G. Wee, O. Larsson, M. Srinivasan, M. Berggren, X. Crispin, S. Mhaisalkar, *Adv. Funct. Mater.* **2010**, *20*, 4344.
- [146] S. A. Corr, M. Grossman, Y. Shi, K. R. Heier, G. D. Stucky, R. Seshadri, *J. Mater. Chem.* **2009**, *19*, 4362.
- [147] a) A. D. Dysart, J. C. Burgos, A. Mistry, C.-F. Chen, Z. Liu, C. N. Hong, P. B. Balbuena, P. P. Mukherjee, V. G. Pol, *J. Electrochem. Soc.* **2016**, *163*, A730; b) G. Inoue, M. Kawase, *J. Power Sources* **2017**, *342*, 476.



Ziyauddin Khan is presently working with Prof. Xavier Crispin as a Principal Research Engineer in the Laboratory of Organic Electronics at Linköping University, Sweden. He received his Ph.D. in Chemistry from the Indian Institute of Technology Guwahati, India, in 2013. Thereafter, he worked at the Tata Institute of Fundamental Research, Mumbai, as a postdoctoral visiting scientist. In early 2014, he joined as a postdoctoral research associate at Ulsan National Institute of Science & Technology (UNIST), Republic of Korea. His research interest is focused on the design of nanostructured inorganic materials and conducting polymers for applications in batteries, supercapacitors, and electrocatalysis.



Prem Singh received his B. Pharmacy in 2012 from the Indo-Soviet Friendship College of Pharmacy Moga, Punjab, India and later M. Pharmacy in Pharmaceutics in 2014 from Swift School of Pharmacy under Punjab Technical University, India. He worked as a Team Leader in the quality control department (analytical method validation) at Cipla Pharmaceutical Ltd. and Panacea Biotec. He is currently pursuing his Ph.D. in the field of nanobiotechnology from the Indian Institute of Technology, Mandi, India under the supervision of Dr. Amit Jaiswal. His primary research interest includes the synthesis of plasmonic nanostructures for SERS sensing, photo-thermal therapy, and catalysis.



Amit Jaiswal is presently an Assistant Professor in the School of Basic Sciences at Indian Institute of Technology Mandi, India. He is also an associate of the Indian Academy of Sciences Bangalore, India. Dr. Jaiswal completed his Ph.D. in Nanotechnology from the Indian Institute of Technology Guwahati, India and post-doctoral research from Washington University in St. Louis, USA and Technion – Israel Institute of Technology, Haifa, Israel. His research interest is in the synthesis of nanomaterials for sensing, catalysis, therapeutic and diagnostic applications.



Manav Saxena received his Ph.D. (Chemistry) from the Indian Institute of Technology Kanpur, Uttar Pradesh, India in 2012. He worked as UGC-Dr. D S Kothari postdoctoral fellow in IEST Shibpur, West Bengal, India. In 2014, he joined Prof. Rodney S. Ruoff's research group at Center for Multidimensional Carbon Materials-IBS, UNIST, Ulsan, South Korea as a postdoctoral fellow. He joined the Centre for Nano and Material Sciences, JAIN University, Karnataka, India as an Assistant Professor in 2017. His research interest is the synthesis and development of controlled heterostructures as active energy electrode materials.